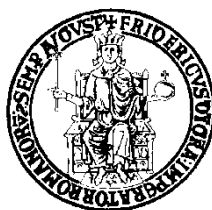


UNIVERSITÀ DEGLI STUDI DI NAPOLI FEDERICO II



Sustainable agricultural and forestry systems and food security

XXXV CYCLE

*Impacts of climatic seasonality and land use on the ecosystem
functions in a Mediterranean agro-forest environment.*

PhD Program Coordinator

Chiar.^{mo} Prof. Albino Maggio

Supervisor

Chiar.^{mo} Prof. Ing. Nunzio Romano

Co-supervisor

Chiar.^{mo} Dr. Paolo Nasta

PhD candidate

Dott.ssa Carolina Allocca

ACKNOWLEDGEMENTS

I want to express my sincere gratitude to all the individuals who have contributed to the completion of this thesis. This work represents the culmination of years of dedication and would not have been possible without the support and input of many people.

First and foremost, I wish to thank my supervisor, Prof. Nunzio Romano, and my co-supervisor for their invaluable guidance and unwavering support throughout the research journey. Their expertise and enthusiasm have inspired and steered my work.

I want to express my gratitude to all the people in my thesis for their invaluable contribution: Fabio Marzaioli, Luisa Stellato, Caterina Mazzitelli, Isabella Passariello, Ugo Lazzaro, Benedetto Sica, Paola Di Fiore, Mario Palladino, Mauro Rubino for their valuable insights and advice that have enhanced the quality of this thesis.

Special thanks go to my family for their constant emotional and motivational support. Words cannot express my gratitude for their encouragement at every stage of this academic journey.

To my friends and colleagues, I thank you for the stimulating conversations, mutual support, and shared laughter that have made this academic experience more meaningful.

Lastly, I want to thank everyone who participated in my research and contributed their time and invaluable collaboration.

Thank you to everyone who has made this thesis possible.

ABSTRACT

Mediterranean agroecosystems are experiencing rapid environmental changes due to natural and anthropogenic perturbations. According to the IPCC, the regions of the Mediterranean area are particularly vulnerable to global warming, and their vulnerability might increase to extreme events, i.e., more floods in winter and more droughts, fires, and water shortages in the future. The concepts of ecosystem vulnerability and resilience indicators have been recently used in environmental studies to describe an ecosystem's ability, in general, not only to cope with natural extreme events or anthropogenic disturbances but also to recover its functions at a greater or lesser rate.

In this study, we identified two ecosystem vulnerability and resilience indicators at the regional scale. In this regard, we used an advanced geostatistical tool to map soil physical and hydraulic properties.

Seven primary soil properties were estimated over 75-m ×75-m blocks by jointly analyzing more than 3,000 point-based soil measurements with gridded terrain attributes using multi-located block cokriging. Two compound soil indicators were then assessed from the maps of these soil properties: 1) the soil organic carbon stock (SOCS) in the entire region of Campania, which represents a resilience indicator, and 2) the groundwater recharge transit time in the Sele alluvial plain where information about the mean annual depth to groundwater is available. The recharge transit time represents an ecosystem vulnerability indicator.

In the second part of this doctoral thesis, we carried out an intensive field campaign with a transdisciplinary approach to better describe and understand the dynamics of hydrological processes across different spatial scales in two experimental plots (MFC2 and GOR1) located in the Upper Alento River catchment (southern Italy). Sporadic (fortnightly to monthly frequency) measurements of stable isotopes ($\delta^2\text{H}$ and $\delta^{18}\text{O}$) were sampled in water from the shallow aquifer (at MFC2 only), streamflow, and bulk precipitation. Water samples were extracted from soils and plant twigs using the CIRCE laboratory's cost-effective cryogenic vacuum distillation equipment (University of Caserta). The stable isotopes were used in Hydrus-1D to simulate isotope transport in the soil-plant-atmosphere continuum. In this regard, we exploited stable isotope measurements taken from a potted olive tree in a glasshouse and validated model simulations. We estimated the root water uptake transit time, which will be used at the plot scale in a follow-up study.

TABLE OF CONTENTS

SUMMARY

1	Introduction.....	1
1.1	Research questions and objectives	7
1.2	Structure of the thesis	9
2	Effective estimation of soil physical properties and their uncertainties using advanced geostatistical tool	10
2.1	Introduction	10
2.1.1	Framework and goal of the study – Relevance of the research.....	12
2.2	Case study and methods	15
2.2.1	Sampling and laboratory measurements	15
2.2.2	Geostatistical modeling.....	18
2.2.3	Composite indicators of soil behavior	23
2.3	Results and discussions	25
2.3.1	Splitting Campania into representative land units (RLUs)	25
2.3.2	Mapping primary soil properties and associated uncertainties	26
2.3.3	Mapping compound indicators of soil behavior	37
2.4	Concluding remarks.....	40
3	Using a transdisciplinary approach to better describe dominant agro-hydrological processes in two basin agro-forest ecosystems.....	42
3.1	Introduction	42
3.2	Materials and Methods	45
3.2.1	Site description and field campaign	45
3.2.2	Hydroclimatic monitoring.....	49
3.2.3	Stable water isotopic monitoring	50
3.2.4	Extraction of water from the soil and the plant.....	52
3.2.5	Sample $\delta^{18}\text{O}$ and $\delta^2\text{H}$ measurements.....	53
3.2.6	Soil moisture monitoring	55
3.2.7	Isotope Data Analysis	56

3.3	Results	58
3.3.1	Dynamics in hydroclimate and soil moisture.....	58
3.3.2	Dynamics of stable isotopes.....	60
3.4	Discussion	70
4	Coupling isotope tracing and eco-hydrological modeling to quantify root water uptake transit time	72
4.1	Introduction	72
4.2	Materials and Methods	73
4.2.1	Experimental setup, monitoring, and sampling approach.....	73
4.2.2	Simulation of isotope transport in the potted olive tree experiment	75
4.2.3	Determination of root water uptake source and transit time with the virtual tracer experiment.....	76
4.3	Results	77
4.3.1	Simulation of isotope transport in the potted olive tree experiment	77
4.3.2	Determination of root water uptake source and transit time through the virtual tracer experiment.....	78
4.4	Discussion	82
4.4.1	Quantifying irrigation uptake dynamics.....	82
4.4.2	Model limitations	83
4.5	Concluding remarks.....	84
5	Conclusion	93
6	References.....	94

LIST OF TABLES

TABLE 2-1 COUNT, MINIMUM (MIN), MAXIMUM (MAX), MEAN, MEDIAN, STANDARD DEVIATION (SD), SKEWNESS, KURTOSIS OF CLAY, SAND, ORGANIC MATTER (OM), ROCK FRAGMENT (RF), CALCIUM CARBONATE (CaCO ₃), SOIL BULK DENSITY (BD), pH, ELEVATION (Z), SLOPE, FLOW ACCUMULATION (FA), PLAN CURVATURE (PLANc) AND PROFILE CURVATURE (PROFc) FOR SOIL SAMPLES COLLECTED IN THE ENTIRE REGION OF CAMPANIA.	27
TABLE 2-2 CORRELATION MATRIX BETWEEN CLAY, SAND, ORGANIC MATTER (OM), ROCK FRAGMENT (RF), CALCIUM CARBONATE (CaCO ₃), BULK DENSITY (BD), pH, ELEVATION (Z), SLOPE, FLOW ACCUMULATION (FA), PLAN CURVATURE (PLANc) AND PROFILE CURVATURE (PROFc) FOR SOIL SAMPLES COLLECTED IN THE ENTIRE REGION OF CAMPANIA.	28
TABLE 2-3. MODEL PERFORMANCE IN TERMS OF MEAN ERROR (ME) AND MEAN STANDARDIZED SQUARE ERROR (MSSE) FOR THE GAUSSIAN DATA OF CLAY (G CLAY), SAND (G SAND), SOM (G SOM), BD (G BD), RF (G RF), CaCO ₃ (G CaCO ₃), pH (G pH).....	29
TABLE 2-4. RESULTS OF BLOCK SUPPORT CORRECTION FOR THE SELECTED SOIL VARIABLES: CLAY, SAND, ORGANIC MATTER (OM), ROCK FRAGMENT (RF), CALCIUM CARBONATE (CaCO ₃), BULK DENSITY (BD), pH.	32
TABLE 3-1 THE AVERAGE PRECIPITATION (P), TEMPERATURE (T), POTENTIAL EVAPOTRANSPIRATION POTENTIAL (ET ₀), AND RELATIVE HUMIDITY (RH) FOR TWO EXPERIMENTAL SITES (AT MFC2 AND GOR1) OVER THE PERIOD OF 2016-2022.	58
TABLE 3-2 MINIMUM, MAXIMUM, MEAN, MEDIAN, AND STANDARD DEVIATION VALUES OF ISOTOPIC SIGNATURES IN THE RAIN, GROUNDWATER, STREAMFLOW, PLANTS, AND SOIL SAMPLING IN EACH DEPTH SEGMENT IN MFC2	64
TABLE 3-3: MINIMUM, MAXIMUM, MEAN, MEDIAN, AND STANDARD DEVIATION VALUES OF ISOTOPIC SIGNATURES IN THE RAIN, GROUNDWATER, STREAMFLOW, PLANTS, AND SOIL SAMPLING IN EACH DEPTH SEGMENT IN GOR1	65
TABLE 4-1 MEAN, STANDARD DEVIATION, COEFFICIENT OF VARIATION, MINIMUM AND MAXIMUM AMOUNTS OF IRRIGATION (IRR), TRANSIT TIME (τ), AND IRRIGATION CONTRIBUTION TO ACTUAL TRANSPIRATION (T_A/IRR) FOR THE FIRST 21 IRRIGATION EVENTS USED IN THIS STUDY. THE LAST FIVE EVENTS WERE IGNORED BECAUSE THEIR ARRIVAL TIME EXCEEDED THE TIME OF THE MODEL SIMULATION.	80

LIST OF SUPPLEMENTARY TABLES

SUPPLEMENTARY MATERIAL TABLE S 4-1. OPTIMISED VALUES OF THE SOIL HYDRAULIC PARAMETERS α , N , AND K_s WITH THEIR 95% CONFIDENCE LIMITS AND CORRELATION MATRIX.	90
--	----

LIST OF FIGURES

FIGURE 2-1. DIGITAL ELEVATION MODEL (DEM) OF CAMPANIA (75-M GRID SIZE) FROM WHICH THE SLOPE, PLAN CURVATURE, PROFILE CURVATURE, AND FLOW ACCUMULATION WERE DERIVED. SYMBOL Z DEPICTS ELEVATION IN UNITS OF M ABOVE SEA LEVEL.	16
FIGURE 2-2 MAP OF THE FOUR REPRESENTATIVE LAND UNITS (RLUs) IDENTIFIED IN CAMPANIA (LEFT); 3,316 SAMPLING POSITIONS DISTRIBUTED WITHIN THE FOUR RLUs (RIGHT).	25
FIGURE 2-3. AUTO- AND CROSS-VARIOGRAMS OF THE BLOCK LINEAR MODEL OF CO-REGIONALIZATION FOR THE GAUSSIAN DATA OF CaCO_3 (G CaCO_3), CLAY (G CLAY), Z (GZ), SOM (G SOM), SAND (G SAND), BD (G BD), FA (G FA), RF (G RF), PH (G PH), PLANC (G PLANC), PROF C (G PROF C), AND SLOPE (G SLOPE). THE GREEN POINTS ARE THE EXPERIMENTAL VALUES WHEREAS THE RED DOTTED LINES ARE THE MODEL OF CO-REGIONALIZATION. THE VERTICAL LINES ARE THE HULL OF PERFECT CORRELATION, WHEREAS THE HORIZONTAL DASHED LINES ARE THE EXPERIMENTAL VARIANCES.	30
FIGURE 2-4. HISTOGRAMS OF A) CLAY, C) SAND, E) SOM, G) RF, I) CaCO_3 , K) BD, M) PH; ANAMORPHOSIS OF B) CLAY, D) SAND, F) OM, H) RF, J) CaCO_3 , L) BD, N) PH. POINT AND BLOCK MODELS ARE DENOTED BY BLUE AND RED COLORS, RESPECTIVELY.	33
FIGURE 2-5 75-M-GRID-SIZE MAPS OF EXPECTED VALUES OF A) CaCO_3 , C) CLAY, E) SOM, G) SAND, I) BD, K) RF, M) PH; AND CORRESPONDING UNCERTAINTY OF B) CaCO_3 , D) CLAY, F) SOM, H) SAND, J) BD, L) RF, N) PH.	35
FIGURE 2-6. A) 75-M-GRID-SIZE MAP OF NEAR SOIL SURFACE SOIL ORGANIC CARBON STOCK (SOCS), B) LAND USE MAP REFERRED TO 2018 (DOWNLOADED FROM THE COPERNICUS LAND MONITORING SERVICE WEBSITE).	36
FIGURE 2-7. A) GEOGRAPHICAL POSITION OF THE SELE RIVER PLAIN (RED POLYGON) IN CAMPANIA (HILLSHADE), B) 75-M-GRID-SIZE MAP OF MEAN RECHARGE TRANSIT TIME, T_{RM}	38
FIGURE 3-1 GEOGRAPHIC LOCATION OF THE UPPER (UARC, GREEN POLYGON) AND LOWER (LARC, RED POLYGON) ALENTO RIVER CATCHMENT IN SOUTHERN ITALY.	45
FIGURE 3-2 GEOGRAPHICAL LOCATION AND 5-M DIGITAL ELEVATION MODEL (DEM) OF THE UPPER ALENTO RIVER CATCHMENT (UARC) IN CAMPANIA (SOUTHERN ITALY). ALSO SHOWN ARE THE TWO EXPERIMENTAL SITES (MFC2 AND GOR1) WITH THE RELEVANT WEATHER STATIONS. THE ARTIFICIAL WATER RESERVOIR IS DELIMITED BY THE PIANO DELLA ROCCA EARTHEN DAM. THE SATELLITE IMAGES DISPLAY THE POSITIONS OF THE TWENTY END-DEVICES OF THE SOILNET WIRELESS NETWORK AND COSMIC-RAY NEUTRON PROBE AT MFC2 AND GOR1 THE TRIANGLE DEPICTS THE POSITION OF THE SOIL PROFILE SUBJECT TO ISOTOPIC MEASUREMENTS.	47
FIGURE 3-3 SCHEMATIC OF THE CVD REALIZED AND TESTED FOR SOIL WATER EXTRACTION	53
FIGURE 3-4 LOCAL METEORIC WATER LINE (LMWL) FOR TWO SITES VERSUS THE GLOBAL METEORIC WATER LINE (GMWL). THE RED DOTS (MFC2) AND GREEN DOTS (GOR1) INDICATE THE ISOTOPIC COMPOSITION OF THE RAINFALL COLLECTED FROM OCTOBER 2020 TO OCTOBER 2022.	56

FIGURE 3-5 DAILY VALUES OF A) RAINFALL AND $\Delta^{18}\text{O}$ IN RAINFALL WATER AT MFC2 (A), B) RAINFALL AND $\Delta^{18}\text{O}$ IN RAINFALL WATER AT GOR1 (C), DAILY AIR TEMPERATURE AT MFC2 (RED LINE) AND GOR1 (BLUE LINE) (D) DAILY VOLUMETRIC WATER CONTENT MEASURED BY USING THE GS3 SENSOR AT THE DEPTHS OF 15 CM AND 30 CM AT MFC2 AND GOR1, (E) REFERENCE POTENTIAL EVAPOTRANSPIRATION(ET_0) AT MFC2 AND GOR1 (INTERVAL 15 MIN) AND $\Delta^{18}\text{O}$	60
FIGURE 3-6 DUAL-ISOTOPE PLOT FOR WATER SAMPLES OF RAIN, STREAMFLOW, GROUNDWATER (GW) SOIL AND PLANT IN TWO EXPERIMENTAL SITES, MFC2(A) AND GOR1(B)	61
FIGURE 3-7: BOXPLOTS OF SOIL WATER AND XYLEM WATER D-EXCESS. BOXES REPRESENT THE LC-EXCESS, WHILE WHISKERS INDICATE THE MINIMUM AND MAXIMUM VALUES, EXCLUDING THE OUTLIERS. THE HORIZONTAL SOLID LINE WITHIN BOXES REPRESENTS THE MEDIAN.	62
FIGURE 3-8 SEASONAL SAMPLE OF THE ISOTOPIC RATIO FOR WATER SAMPLES OF RAIN, STREAMFLOW, GROUNDWATER (GW) SOIL AND PLANT IN TWO EXPERIMENTAL SITES, MFC2(A) AND GOR1(B)	66
FIGURE 3-9 SEASONAL SAMPLE OF THE ISOTOPIC RATIO FOR WATER SAMPLES SOIL AND PLANT IN MFC2 (OLIVE MONITORING POINT)	67
FIGURE 3-10: THE DAILY SOIL WATER CONTENT VERSUS THE MEASUREMENT OF $\Delta^{18}\text{O}$ IN SOIL WATER. THE BLUE TRIANGLES REPRESENT THE RELATIONSHIP BETWEEN WATER CONTENT AND $\Delta^{18}\text{O}$ ON SAMPLING DAYS FROM OCTOBER TO MARCH, WHILE THE RED ONES REPRESENT THE RELATIONSHIP BETWEEN WATER CONTENT AND $\Delta^{18}\text{O}$ ON SAMPLING DAYS FROM APRIL TO SEPTEMBER. THE PLOT (A) RELATES TO THE SAMPLES COLLECTED AT 15 CM DEPTH, WHILE PLOT (B) RELATES TO THOSE COLLECTED AT 30 CM DEPTH. THE DATA IS RELATED TO THE MFC2 SITE.	68
FIGURE 3-11: THE DAILY SOIL WATER CONTENT VERSUS THE MEASUREMENT OF $\Delta^{18}\text{O}$ IN SOIL WATER. THE BLUE TRIANGLES REPRESENT THE RELATIONSHIP BETWEEN WATER CONTENT AND $\Delta^{18}\text{O}$ ON SAMPLING DAYS FROM OCTOBER TO MARCH, WHILE THE RED ONES REPRESENT THE RELATIONSHIP BETWEEN WATER CONTENT AND $\Delta^{18}\text{O}$ ON SAMPLING DAYS FROM APRIL TO SEPTEMBER. THE PLOT (A) RELATES TO THE SAMPLES COLLECTED AT 15 CM DEPTH, WHILE PLOT (B) RELATES TO THOSE COLLECTED AT 30 CM DEPTH. THE DATA IS RELATED TO THE GOR1 SITE.	69
FIGURE 4-1 A) SAP FLOW SENSORS WERE INSTALLED IN THE TRUNK OF THE OLIVE TREE (OLEA EUROPAEA) AND PLACED IN A 70 L POT COVERED BY A PLASTIC FILM; B) CROSS-SECTION OF THE SOIL PROFILE IN THE POT WITH THE POSITIONS OF THE THETA PROBE SHOWN ON THE SOIL SURFACE AND THE THREE SOIL SAMPLING DEPTHS (0-5 CM, 5-15 CM, AND 15-25 CM) FOR ISOTOPE MEASUREMENTS.	73
FIGURE 4-2 HOURLY DATA OF A) WATER IRRIGATION (IRR) EVENTS (BLUE BARS), ACTUAL TRANSPIRATION, T_a (RED LINE), AND B) SOIL WATER CONTENT, θ (FROM RED TO BLUE INDICATED IN THE COLOUR BAR INDICATING DRY TO WET CONDITIONS) ACROSS THE SOIL PROFILE SIMULATED IN HYDRUS-1D.	77

FIGURE 4-3 HOURLY DATA OF A) TAP (BLUE BARS WITH $\delta^{18}\text{O} = -7.97 \text{ ‰}$) AND LABELLED (YELLOW BARS WITH $\delta^{18}\text{O} = -12.75 \text{ ‰}$) B) $\delta^{18}\text{O}$ (FROM RED TO BLUE INDICATED IN THE COLORBAR) ACROSS THE SOIL PROFILE SIMULATED IN HYDRUS-1D. 78

FIGURE 4-4 HOURLY DATA OF A-B) TAP (1ST EVENT) AND LABELLED (14TH EVENT) WATER IRRIGATION (IRR) EVENT (BLACK BAR) WITH KNOWN $\delta^{18}\text{O}$ SIGNATURE, ISOTOPE-FREE IRRIGATION EVENTS (CYAN BARS), ACTUAL TRANSPIRATION, T_A (RED LINE), C-D) $\delta^{18}\text{O}$ (FROM WHITE TO BLACK INDICATED IN THE COLORBAR) ACROSS THE SOIL PROFILE, E-F) CUMULATIVE ROOT $\delta^{18}\text{O}$ UPTAKE (GREEN LINE). VERTICAL DASHED LINES INDICATE ENTRY (T_{IN}) AND ARRIVAL (T_{OUT}) TIMES... 79

FIGURE 4-5 A) CUMULATIVE ROOT WATER UPTAKE (RWU) TILL ARRIVAL TIME FOR EACH IRRIGATION EVENT, B) CUMULATIVE ROOT ISOTOPE UPTAKE TILL ARRIVAL TIME FOR EACH IRRIGATION EVENT, C) RELATIONSHIP BETWEEN RWU AND ROOT ISOTOPE UPTAKE SUMS WITH DASHED LINE INDICATING THE FITTING LINEAR REGRESSION EQUATION WITH CORRESPONDING COEFFICIENT OF DETERMINATION (R^2); THE CIRCLES ARE COLOUR-CODED ACCORDING TO THE CORRESPONDING RWU TRANSIT TIME (τ). 81

LIST OF SUPPLEMENTARY FIGURES

SUPPLEMENTARY FIGURE S 4-1. HOURLY DATA OF A) OBSERVED (WHITE CIRCLES) AND SIMULATED (BLUE LINE) SOIL WATER CONTENT VALUES AT $Z = -3 \text{ CM}$ AND B) OBSERVED (COLOURED CIRCLES) AND SIMULATED (COLOURED LINES) $\delta^{18}\text{O}$ (‰) AT $Z = -3, Z = -10, \text{ AND } Z = -20 \text{ CM}$ 91

SUPPLEMENTARY FIGURE S 4-2. HOURLY DATA OF A) OBSERVED SAP FLOW (YELLOW CIRCLES) AND SIMULATED ACTUAL TRANSPIRATION, T_A (RED LINE) Z-SCORES, AND B) OBSERVED (GREY CIRCLES) AND SIMULATED (GREEN LINE) $\delta^{18}\text{O}$ (‰) IN THE TWIG TISSUES..... 92

1 Introduction

Terrestrial (forestry and agricultural) systems provide natural capital and ecosystem services and functions to the human economy and society (Dong et al., 2010).

The exploitation of natural capital has allowed human beings to adapt to the environment and develop increasingly complex infrastructures for human well-being. Our planet's natural resources are not only limited, but they can rapidly degrade. Since the 1970s, there has been particular attention to the problem of the exhaustion of natural resources. In 1972, "The Club of Rome", founded by the Italian economist Aurelio Peccei, published the first report entitled "Limits to Growth", which analyzed the contemporary world problems driven by demographic increase and limitless economic development within limited environmental conditions. The Club of Rome report was revised in 1992 by researchers from the Massachusetts Institute of Technology, who updated the analysis by confirming the thesis written twenty years earlier. The scope was a reduction of energy consumption and resources to prevent a sudden collapse of the system. The researchers claimed, *"To slow down this process, man must push the accelerator on efficiency and simultaneously slow down consumption and population growth"*. In other words, the principle of sustainable development was born. The term "sustainability" was used before 1992. Another crucial moment of sustainable development was represented by the United Nations Conference in Rio de Janeiro in 1992. The Conference approved "Agenda 21," which states *"the right to development must be realized in such a way as to reasonably meet the needs relating to the environment and the story of the present and future generations"*. Finally, "the Agenda 2030 for sustainable development" was signed on 25 September 2015 by 193 United Nations countries, including Italy, to share the commitment to guarantee a better present and future for our planet and the people who live there. The Global Agenda defines 17 Sustainable Development Goals to be achieved by 2030, divided into 169 Targets, by paving the way to a shared roadmap for placing Italy and the world on a sustainable path. The process of changing the development model is monitored through Goals, Targets, and over 240 indicators: concerning these parameters, each country is periodically assessed by the United Nations (UN) and by national and international public opinion. The

Agenda 2030 expresses the sustainability of the current development model, not only on the environmental level but also on the economic and social one, overcoming the idea that sustainability is only an environmental issue but also an integrated vision of the different dimensions of development. One of the key aspects of international debates, which emerges above all from the strategies for sustainable development and adaptation to climate change, is that of ecosystem services, the benefits that nature offers and contributes to environmental stability and the well-being of the socioeconomic system. What is underlined is that the vital role of ecosystem services has been ignored for a long time, which has contributed to the unsustainable exploitation of natural resources.

CBD (Convention on Biological Diversity, 1992) defines an ecosystem as "*a dynamic complex of plant, animal and microorganism communities and their non-living environment interacting as a functional unit*". The diversity of functional groups is relevant to the ecosystem functioning. Ecosystem functions are based on and define the biological, geochemical, and physical processes within an ecosystem. They refer to the structural components of an ecosystem (e.g., water, soil, atmosphere, and biota) and their interactions within and across ecosystems (Zedda et al., 2015). The most relevant exchanges within ecosystems, for example, concern energy and nutrients (i.e., carbon and nitrogen), as well as the production and decomposition of biomass (Jax, 2010). The set of ecosystem functions offers humans and the surrounding environment a series of goods and services called ecosystem services. We report two other commonly referenced and representative definitions:

1. *Ecosystem services are the conditions and processes through which natural ecosystems and the species that make them up sustain and fulfill human life. They maintain biodiversity and the production of ecosystem goods, such as forage timber, biomass fuels, natural fiber, pharmaceuticals, industrial products, and their precursors (Daily, 1997b).*
2. *Ecosystem goods (such as food) and services (such as waste assimilation) represent the benefits human populations derive, directly or indirectly, from ecosystem functions (Costanza et al., 1997).*

According to the new version of the Common International Classification of Ecosystem Services (Haines-Young & Potschin, 2018), Ecosystem Services are divided into three main categories:

- Provisioning services: material services related to the goods provided by ecosystems.
- Regulating services: intangible services with a regulative function (e.g., erosion control, water purification, climate control).
- Cultural services: nonmaterial benefits obtained from ecosystems.

Any biome produces ecosystem services that might influence human well-being. Human interventions can increase some benefits, though often at the expense of others. An ecosystem typically comprises many different regions, such as forests, agriculture, and urban areas, each producing a different bundle of services. For example, forest ecosystems provide various ecosystem functions and services essential to ensure the stability of ecological and anthropogenic systems. The forests have a vital role in preserving global biological diversity, such as tropical forests alone account for approximately 50% of the 5-20 million plant and animal species on Earth. Moreover, they are also a regulatory mechanism of the climate system (Prävälje, 2018). A recent paper by Van Meerveld et al. (2021) demonstrated that forest regeneration could positively contribute to local hydrological ecosystem services. The results depend on the trade-off between the improved soil infiltration capacity (reducing overland flow and increasing soil and groundwater recharge) and greater evapotranspiration (diminishing local water availability). Moreover, the hydrological effects of forest restoration could be on a large scale, with variations in the local climate (exposure to rainfall and solar radiation or fog) also significant. Forest restoration could positively impact precipitation on a large scale, at least in theory (Ellison et al., 2017). Above canopy intercepts rain and snow by improving soil structure and reducing surface runoff. These phenomena represent a vital ecosystem service in watersheds where erosion, floods, or avalanches imply high costs, high risks of damaging infrastructure or productive croplands, residential property, the environment, and humans (Wunder & Thorsen, 2014).

Several global scientific reports, in the last 18 months alone, issued by the Intergovernmental Panel on Climate Change (IPCC), Intergovernmental Science-Policy Platform report on Biodiversity and Ecosystem Services (IPBES), International Resource Panel (IRP) and UN Environment, show how the current exploitation of natural resources appears unsustainable (SOER, 2020). European Union (EU) must solve persistent problems such as biodiversity loss, resource use, impacts of climate on ecosystem services, and environmental risks to health and well-being. Human activities and climate change have caused widespread reductions in animal and plant populations and the extent and integrity of ecosystems. Over the last 50 years, the impact of climate change and human activities on ecosystem functions and services has been observed worldwide (IPBES, 2019; UN Environment, 2019; IPCC, 2022).

In the era of the Anthropocene, in which humans have heavily altered the Earth system (Ellis, 2011), the consequences of environmental change, the need to improve the well-being of people around the world, and the need to conserve the biodiversity together on a planetary scale require attention on how to manage ecosystems in a sustainable way and the provision of ecosystem services for the well-being of society. Several research approaches have been proposed for a better understanding of the ecosystem service concept. These are studies based mainly on the principles of sustainable development with objectives to improve the functions of an ecosystem and consequently the services it offers (Bennett, 2015). Sustainability is defined as the ability of an agroecosystem to maintain productivity when subject to a major disturbing force. The actual or potential disturbance may be caused by intensive stress, where stress is defined as a frequent, sometimes continuous, relatively small, and predictable disturbing force that has a large cumulative effect (Conway, 1987).

About 40% of the global land surface has been converted into agroecosystems, systems modified to produce food, fiber, fuel, and other products for human consumption and processing.

The soil is a key component of an agroecosystem. In fact, soil has been designated as a natural capital or stock yielding a sustainable flow of valuable goods and services (Dominati et al., 2010). The soils are essential for the functioning of

terrestrial ecosystems in many different ways including climate control, water quantity and quality, nutrient cycle and the habitat of a biodiversity (Vogel, 2019). Many environmental problems affecting other environmental matrices derive from the alteration of the processes that occur in the soil. Such alterations are essential and cause changes in the functioning of ecosystems.

Hewitt et al. (2015) assert that soil is a neglected component in ecosystem services studies and policy making. Daily et al. (1997) suggested that soils are one of the essential components of a nation's economic status and including soils in a country's ecosystem services frameworks, policies, and decision-making processes is extremely important. McBratney et al. (2014) and Robinson et al. (2012) emphasize the need to evaluate soil ecosystem services and promote soil-ecosystem linkage in land resource policy and management development. There are many studies on soil and ecosystem services, but not all have explored the direct relationship with soil properties (Adhikari & Hartemink, 2016). Adhikar and Hartemink (2016) have developed a conceptual diagram that links the key soil properties to ecosystem services through its functions for human well-being. However, to grow awareness that soil plays a critical role in several environmental services.

Therefore, the main concerns for soils are mainly two: food security and the functioning of terrestrial systems. Both are endangered by land use and climate change, with a direct impact on the contribution of soil functions to ecosystem services. Considering this more significant attention to the soil, there is a need to evaluate the offer of the ground's functions.

Zwetsloot et al. (2020) explored the current state of soil multifunctionality in Europe and the interactions between soil functions in five climate zones and two types of land use (arable land and forests). This study's author concluded that using correlation and co-occurrence analyses, the synergies, and trade-offs between soil functions vary among climatic zones and land-use types.

Rabot et al. (2022), have studied potential soil multifunctionality using the concepts of soil-based ecosystem services and soil functions. They have considered the provision of physical and chemical habitat for plant growth, the retention and transfer of water and pollutants, and the carbon storage function. The results of this

study have taken exciting conclusions regarding the use of soil functions for evaluating environmental issues related to agriculture.

Agroecosystems support many ecosystem services and consequently, their management is increasingly necessary to achieve sustainability objectives (Allen, 2022).

The World Commission for Environment and Development (WCED) definition of sustainability includes a concept that is still widely used: "*meeting the needs of the present generation without compromising the ability of future generations to meet their own needs*" (WCED, 1987).

In the general context of ecosystem services offered by an environment, the concept of "resilience" cannot perhaps be separated from that of "sustainability". In fact, one of the five ESR Framework's core principles (Attwood et al. 2014; Quintero et al., 2015) is based on building resilience: "*Building resilience is about enhancing the capacity of communities to develop in an uncertain world sustainably*". In general, the resilience of an ecosystem can be synthetically expressed as its greater or lesser capacity to restore the pre-existing state upon the occurrence of a certain perturbation, be it natural (such as an earthquake or a volcanic eruption) or anthropogenic (such as contamination) (Kumar et al., 2010). On the other hand, with a slightly more quantitative vision and more linked to an assessment of environmental risk, the resilience of an ecosystem would be associated with the "return period" so that the perturbed ecosystem resumes the state of equilibrium that existed before the disturbance or a new one follows (Tardio et al., 2017).

Kaptijn (2018) found that an insight into how ancient practices have managed to achieve positive results, but also negative effects, in achieving socio-ecological resilience through water management, can help our modern communities to cope with problems similar. The fact that an irrigation practice was sustainable in the past does not necessarily mean that the same is true today. Another example is the fact that, contrary to the often expressed assertion that the agronomic technique of "slash and burn" is deleterious and responsible for the loss of a large part of tropical forests, it seems instead that in the long term it is a practice to be considered sustainable.

Very often the decrease of resilience in an assigned ecosystem determines a decay of regulatory services and, consequently, also the performance of procurement services can decline markedly. Some agronomic or water resource management practices for irrigation purposes are clear examples (Parris, 2010). Precisely in areas more prone to suffer the negative effects of drought, such as some areas of the Mediterranean, greater resilience can certainly be achieved by improving the efficiency of water use, by intervening in one or more of the following factors:

- Reduction of losses in water conveyance and delivery systems.
- Increasing rainwater collection systems.
- Make greater use of use of marginal water (e.g. purified wastewater).
- Improvement of soil moisture monitoring techniques.
- Recharging of groundwater during periods of lower seasonal water demand.
- Careful use of mechanical soil processing practices, and this last factor is to be placed directly in relation to soil erosion.

In issues of over-exploitation of water resources and soil degradation, the resilience of a certain ecosystem can be increased by involving more land management bodies and stakeholders, while precisely for marginal rural areas their resilience can be increased by combining practices traditional with the most modern sustainable production systems.

1.1 Research questions and objectives

Research questions

In this thesis, the overarching theme connecting the presented work is the critical importance of studying ecosystem functions related to the sustainable management of water resources in Mediterranean climate regions. Furthermore, it emphasizes the importance of employing advanced observation and analysis techniques to address these challenges. We conducted our research at two different spatial scales: the Campania region and two small basins within the Campania region. While the studies all tackled similar research questions and addressed the same problem, they were approached with distinct methodologies. We aim to highlight the use of advanced techniques employed in this study and underscore the importance of developing a method that could be beneficial for other research endeavors.

On this latter point, during the doctoral period two novel points have been developed: *i*) a cost-effective cryogenic vacuum distillation equipment, *ii*) an advanced geostatistical tool to map soil physical and hydraulic properties.

The overarching research questions that link the different parts of this doctoral thesis are as follows: How does an ecosystem respond to potential changes in land use and climatic conditions? How does a particular ecosystem adapt to these changes to ensure the provision of water-related ecosystem functions?

At the regional scale, we focused on assessing the physical resilience of soil to changes in climatic conditions, particularly in regions subject to Mediterranean-type climate seasonality and frequent shifts in agro-ecosystems. In this context, the concept of "water transit time" (τ) was introduced to analyze the transport of water and solutes at a specific spatial scale. This parameter represents a functional indicator for understanding and managing water resources in these regions. A tangible example is the use of the water transit time indicator developed by Batsukh et al. (2022) to highlight relevant aspects of soil characteristics influencing the recharge of shallow groundwater.

At the scale of the experimental sites within the small basins, we conducted integrated monitoring using water isotopes in soil and plant matrices. This monitoring allowed for a detailed assessment of ecohydrological flows, i.e., how water is distributed and utilized in two different land use units. Specific points within these basins were studied as representatives of ecosystem functions across the entire basin. This approach provides a comprehensive understanding of how ecosystems respond to variations in climate change and land use, thereby contributing to the development of sustainable water resource management strategies.

Furthermore, it is important to emphasize that the advanced methods and techniques used in this thesis have not only yielded relevant research findings but also have the potential to be applied in other similar study contexts. This underscores the importance of creating methodologies that can be beneficial to the broader scientific community, thereby advancing knowledge in the fields of ecology and water resource management.

In conclusion, this thesis successfully addresses the crucial question of how ecosystems respond to climate change and land use in Mediterranean regions, utilizing a combination of advanced methodological approaches and detailed monitoring. This study makes significant contributions to understanding hydrology in these regions and offers methodologies that can be adopted in the future to address similar challenges.

1.2 Structure of the thesis

This thesis comprises three main sections (Chapters 2 to 4) reporting the main activities during the PhD.

Chapter 2 refers to the regional-scale assessment of soil functions and resilience indicators, Accounting for change of support to estimate primary soil properties and their uncertainty.

Chapter 3 highlights the importance of carrying out a transdisciplinary approach to describe dominant hydrological processes in two agro-ecosystems.

Chapter 4 proposes a practical approach combining isotope tracing and Hydrus-1D to estimate root water uptake transit time in a soil-plant-atmosphere system.

2 Effective estimation of soil physical properties and their uncertainties using advanced geostatistical tool¹

2.1 Introduction

Soil quality is viewed in slightly different ways, mainly depending on a researcher's background and the ultimate goal of an investigation. According to the SSSA Glossary (2008), soil quality is defined as the capacity of soil to function within ecosystem boundaries to sustain biological productivity, maintain environmental quality, and promote plant and animal health. Among the various factors that contribute to shaping this capacity, soil organic carbon (SOC) in topsoil can greatly affect soil quality. A decrease in SOC, which is a situation of particular concern in Mediterranean regions, strongly impacts the characteristics of agricultural ecosystems, especially their vulnerability and resilience to disturbances that alter the physical environment (Doran and Parkin, 1994, Lal, 2015).

Recently, resilience has been increasingly used in environmental studies to describe the ability of an ecosystem in general, or soil in particular, not only to cope with natural extreme events or anthropogenic disturbances but also to recover its functions at a greater or lesser rate (Zampieri, 2021). Particular attention has been recently paid to assessing the physical resilience of soil to changes in climatic conditions, especially in regions under Mediterranean-type weather seasonality and subject to frequent changes in agricultural land use. With regard to this aspect, the concept of transit time (τ) was introduced to elucidate water and solute transport phenomena occurring at a certain spatial scale (Hrachowitz et al., 2016, Remondi et al., 2019) and can be viewed as a useful indicator of resilience for water resources management. One example is the transit time indicator (τ_R) used by Batsukh et al. (2022) to highlight some aspects of soil characteristics relevant to shallow groundwater recharge.

¹ This chapter refers to the following paper: Allocca, C., A. Castrignanò, P. Nasta, N. Romano. 2023. Regional-scale assessment of soil functions and resilience indicators: Accounting for change of support to estimate primary soil properties and their uncertainty. *Geoderma* 431: 116339 <https://doi.org/10.1016/j.geoderma.2023.116339>

Maps of vulnerability and resilience indicators support the implementation of sustainable adaptation and mitigation strategies for global changes to ensure the provision of ecosystem functions/services (Costanza et al., 1997, Vereecken et al., 2016). In the search for these strategies, a key step is the design of a sampling scheme to obtain reliable detailed maps from sparse measurements, a task which necessarily brings the concepts of *observation scale* and *model scale* into play (Bierkens et al., 2000). Even though in the past the term *scale* was used quite loosely, especially by scientists from different disciplines, Blöschl and Sivapalan (1995) developed an effective framework to deal with this issue. They defined scale as a spatial or temporal dimension consisting of three components: support, spacing, and extent. The term spatial support refers to the physical dimension (i.e. the size of an area or volume) over which a variable or parameter is measured, spacing is the average distance between two locations of sampling or monitoring, and extent is the spatial size of the study area. This framework is employed today, albeit with a few small nuances, in almost all environmental disciplines when designing a sampling scheme to map a certain variable or running a computer model to portray simulated scenarios of water futures (McBratney, 1998; Hopmans et al., 2002; Romano, 2014).

In several environmental applications on a regional scale, observations are point-based (commonly, having spatial support of a few decimeters) at the nodes of a spatial grid with a mesh size of hundreds of meters or kilometers. Therefore, there is a typical scale mismatch between the dimensions of the spatial spacing and support of the observations and the blocks composing the gridded map of the target variable. The scale transfer from point to block support is defined as support change (Teuling et al., 2006; Gentine et al., 2012; Nimmo et al., 2021).

It is also worth emphasizing that any map of environmental variables and parameters is affected by epistemic uncertainties deriving from a variety of sources related to the sampling approach and support change techniques (Burrough & McDonnell, 1988). Therefore, to quantify the estimation errors when drawing a map is important to correctly frame its suitability for a particular use. Ignoring such errors may lead to undesired and perhaps unforeseen consequences, especially in decision-making for local land management. For these reasons, the *GlobalSoilMap*

community (e.g. Heuvelink, 2014) advocates the requirement to quantify uncertainty also in environmental mapping, where such quantification is often neglected or is limited to only a summary assessment of the map's accuracy.

As mentioned above, the change of support between observed and estimated variables, either upscaling or downscaling, is a critical problem since uncertainties may be highly dependent on the area, or volume, over which the observations are made and the estimates are averaged (Bierkens et al., 2000, Gelfand et al., 2001, Malone et al., 2013, Buttafuoco et al., 2021). To support precision farming and carbon sequestration assessment, for example, agroforestry management requires detailed maps of oven-dry soil bulk density, which is commonly measured on an intact soil core collected with a steel cylinder whose inner volume depends mainly on soil texture and ranges approximately from 100cm^3 to 400cm^3 . Another example is the capacitance probe, embedded at a certain soil depth, which measures the average soil permittivity over a soil volume of approximately 850cm^3 . The cosmic-ray neutron sensor averages soil moisture over horizontal spatial supports with diameters ranging approximately from 300m to 600m (i.e. a spatial resolution of tens of hectares), whereas the investigated soil depths range approximately from 0.20m to 0.50m. Similarly, the use of MODIS products, with a pixel of $250\text{m}\times 250\text{m}$, involves averaging over a horizontal area of $62,500\text{m}^2$ (horizontal spatial resolution) and a soil depth of about 0.05m.

2.1.1 Framework and goal of the study – Relevance of the research

Structural and non-structural measures are usually envisaged to avoid or at least reduce the impacts of hazards. However, the achievement of good policies to implement such measures for restoring degraded zones or re-establishing ecosystem functions, cannot be separated from the need to ensure an efficient allocation of public money. Public managers and stakeholders look at such issues on relatively large spatial scales and thus should obtain information about the status of the environment at these scales as accurately as possible. An example of this type of task is the “Transparency in Campania” blueprint funded by the regional council of Campania to tackle food security and sustainable agriculture problems (additional information can be found at the webpage <https://www.campaniatrasparente.it>). One

of the main aims of this blueprint was to achieve a comprehensive and integrated region-wide picture of the environmental situation through the collection of a large number of samples from groundwater, surface water, soil, vegetation, air, livestock, and human biological fluids (e.g. blood plasma, male seminal liquid).

Regarding the soil component of this blueprint, extensive fieldwork was carried out in the farmlands of Campania (hence excluding the urbanized areas) to collect more than three thousand disturbed samples and intact cores from topsoil, at the nodes of regular grids with mesh ranging from 1,0km to 4,0km, and measure basic soil physical and chemical properties, such as particle-size distribution, oven-dry bulk density, rock fragment, soil organic matter content, calcium carbonate, and pH. The purpose was to map the soil attributes accurately and make efficient evaluations of the impacts of disturbance processes on the ecosystem functions and services of agricultural lands and forest areas in Campania at a spatial scale of some tens of meters. Crossman et al. (2013) stated that this can be a non-trivial question because it involves the use of proper techniques of spatial prediction at a regional scale and the assessment of its uncertainty. One way to fulfill this task is to resort to multivariate geostatistics while exploiting the knowledge of proxy terrain covariates derived from a 75-m Digital Elevation Model (DEM) of Campania to reduce the uncertainty of prediction at unvisited sites.

That said, the primary purpose of our investigation was to address the issues of change of support that come into play when mapping the estimates of point-based, primary soil characteristics in Campania averaged over a 75-m×75-m block support. Using the linear model of co-regionalization (LCM), these maps were obtained by combining laboratory-measured soil properties observed at point (or, pedon) support, with terrain attributes (secondary information) computed using the DEM with a grid cell of 75-m×75-m size (or 75m/pixel). As pointed out by Gotway Crawford and Young (2005), scale and change of support are intertwined questions and should be carefully addressed when dealing with spatial modeling since they can significantly impact prediction reliability. Therefore, the additional objectives of this study were to quantify the epistemic uncertainty associated with the mapping of the primary soil properties and evaluate the impact that change-of-support exerts on the predictions. Several approaches can be followed to address uncertainty. The

one adopted in this paper estimates uncertainty in soil maps through multivariate geostatistical modeling. As an exemplary outcome of our study, we used the maps of individual soil characteristics to identify two compound indicators for soil quality and physical resilience, namely the stocks of soil organic carbon and recharge transit time, that help identify the zones of a landscape that are likely to be more vulnerable than others concerning climatic and anthropogenic disturbances. Although the computation of uncertainty associated with the estimated input soil properties is performed over the selected block support, the uncertainty of the soil quality indicators is not computed. This topic will be discussed in a subsequent article.

The relevance of our investigation is also framed within the pedometrics challenges as reviewed by Wadoux et al. (2021). Specifically, the results discussed in the present paper aim to yield insight into how to provide more precise estimates at scales appropriate for decision-making (challenge #5) and draw representative maps of soil functionality (challenge #7). In the paper by Wadoux et al. (2021), challenge #5 is as follows: *«Can we develop workable techniques to derive predictions of soil characteristics at scales appropriate for modelling and decision making, by up- and downscaling observations in 3D space and time? These techniques should account for complex non-linearities and interactions, and quantify the associated prediction uncertainty»*, whereas challenge #7 is as follows: *«How to recognize, quantify and map soil functionality?»*.

2.2 Case study and methods

2.2.1 Sampling and laboratory measurements

The study area for this investigation (approximately 13,671km²) is the administrative region of Campania (southern Italy; see Figure 2-1), in which 34.6% of the region is classified as montane (southern Apennines), 50.8% as hilly, and 14.6% lowland. Campania is a region with very diverse morphological features. It is characterized by the Apennines ridge and hilly inland areas as well as lowlands mainly along the lower reaches of the two main rivers, the Volturno and Sele. A specific feature is the presence of several volcanic complexes: Roccamonfina (on the Lazio-Campania border), the famous Vesuvius-Mt. Somma, the Campi Flegrei, the volcanoes in the islands of Ischia, Procida, and Vivara, and the marine volcanoes located in the marine sector of the Campi Flegrei caldera. The climate reflects the typical Mediterranean seasonality with cool wet winters and warm dry summers. Mean annual rainfall along the coast ranges between 900mm^{yr}⁻¹ and 1,200mm^{yr}⁻¹. Mean annual rainfall in upland areas is influenced by the orographic setting, reaching as high as 1,500–2,000mm^{yr}⁻¹ in western areas and less than 700–1,000mm^{yr}⁻¹ in eastern zones. Land use has dramatically changed over the last five decades mainly due to socio-economic factors that have caused a massive migration from the rural interior to the urban lowlands (especially toward the cities of Naples and Salerno in the late 1950s and 1960s), which has resulted in an increase in urban sprawl since the Second World War (Nasta et al., 2017). Hilly and montane areas are characterized by the prevalence of forests, while the cultivation of grapevine, olives, tomatoes, and many kinds of cereals and typical vegetable crops of the Mediterranean belt takes place in the region's lowlands and coastal plains.

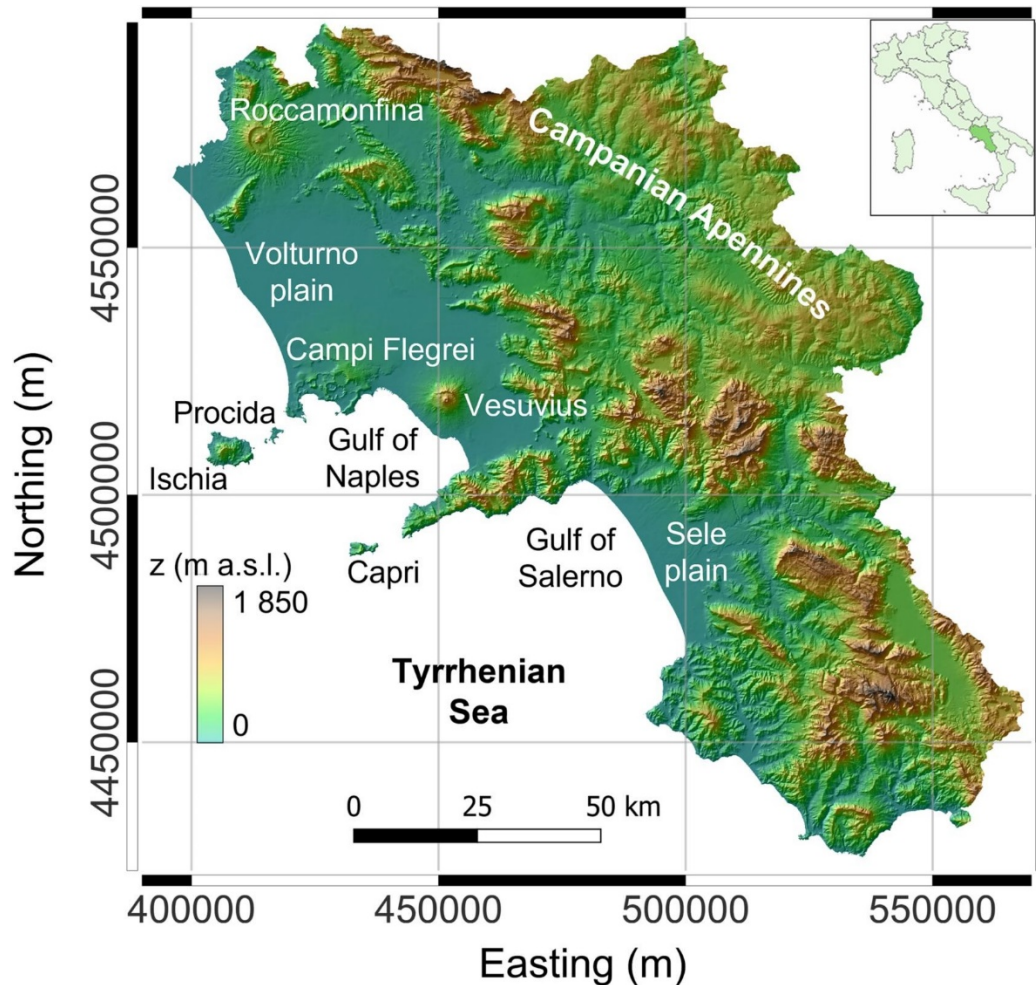


Figure 2-1. Digital Elevation Model (DEM) of Campania (75-m grid size) from which the slope, plan curvature, profile curvature, and flow accumulation were derived. Symbol *z* depicts elevation in units of m above sea level.

The present study refers to a survey carried out in 2017 of a total of 3,316 locations where both disturbed samples and intact cores were collected in the topsoil, at soil depth of about 5cm. The sampling strategy was based on previous data and organized with a variety of regular grid cells as follows: 1-km square cells in coastal plains or highly degraded agricultural areas (e.g. the so-called Land of Fires in the surroundings of the municipalities of Naples and Caserta) and close to urban areas; 2-km square cells in agricultural areas, and 4-km square cells in the hill and mountain areas and those zones under low potential hazards. Soil samples were located randomly within a cell. Since this investigation was part of the “Transparency in Campania” blueprint, which also dealt with agricultural site contamination assessment and management, we did not adopt a composite sampling

strategy to determine soil physical and chemical properties, but the disturbed soil samples were collected in the same pit from where the intact cores were extracted. Each disturbed soil sample was split into four sub-samples, and each was subjected to standard laboratory measurements, carried out at the Laboratory of Soil Hydrology of the University of Naples Federico II, to determine the following soil attributes:

- Soil particle-size distribution was determined using the sieving technique for the sand-sized particles (effective diameter from 2.0mm to 0.50mm) and the hydrometer method for the clay-sized particles (effective diameter less than 0.002mm) (Gee and Or, 2002). The textural class of each soil sample was determined according to the United States Department of Agriculture (USDA) classification from the percentages of sand and clay contents;
- Rock fragment (RF) is considered a coarse mineral fragment greater than 2.0mm. Rock fragment by mass (RF_m ; in g/g) was measured by weighing the particles >2.0 mm and expressed as a percentage of the total mass of the soil sample; RF (%) was expressed here on a by-volume basis and determined by the gravimetric RF_m , the oven-dry soil bulk density (see below for its measurement), and the density of the rock fragments (assumed to be 2.70 g cm^{-3});
- Soil organic carbon (SOC) content was measured from the sieved soil sample (fine fraction less than 2.0mm) using the wet combustion method suggested by Mebius (1960) (potassium dichromate method). SOC was expressed as % by mass and, by convention, we set the soil organic matter (SOM) content equal to $SOM=1.724 \times SOC$ (Russel and Engle, 1928);
- Soil pH was measured using a pH-meter after performing electrode calibration; temperature compensation was not carried out as the measurements were performed in an ambient-controlled room of our laboratory;
- Soil calcium carbonate (CaCO_3) content (%) was determined using the volumetric calcimeter method (FAO, 2020).

Each intact soil core was taken by vertically inserting a steel cylinder, with a volume of approximately 309 cm^3 (0.070m in height, 0.075m in inner diameter). Each soil

core was placed in a ventilated oven, at the standard temperature of 105°C for at least 48h, to measure the oven-dry soil bulk density, BD (g cm^{-3}) (Palladino et al., 2022).

Elevation (z , expressed in m a.s.l.) was taken from a 75-m Digital Elevation Model (DEM) (see Figure 2-1 together with the physiographic features presented at the beginning of this section) that was also used to obtain other input terrain attributes, namely slope (degrees), plan curvature (PlanC), profile curvature (ProfC), and flow accumulation (FA). FA was calculated as the accumulated weight of all cells flowing into each downslope cell in the output raster. The slope is the first derivative of the mathematically continuous surface that constitutes a raster DEM while the second-order derivatives, the rates of change of slope in the downslope direction (ProfC) and perpendicular to the downslope direction (PlanC) are investigated because of their importance in geomorphological and hydrological analyses (Romano & Palladino, 2002).

2.2.2 Geostatistical modeling

Geostatistical analysis was carried out in this study to obtain 75-m grid size (block scale) maps of the seven primary soil variables by using their point-scale measurements. This study treats the change of support from point to block scale as made up of the following main steps:

- Application of block cokriging using irregularly shaped blocks. The expected values are computed by taking into account the spatial correlations while not limiting ourselves to a simple mean value of the observations falling within each polygon;
- Simple cokriging with spatially-varying means;
- Back transformation of the Gaussian variable estimates; we did not use point Gaussian anamorphosis, but rather applied block anamorphosis after proper correction.

It is worth mentioning that the last procedure (i.e., block anamorphosis correction), although known in applications of geostatistics to mining engineering and petroleum industry (e.g. Chilès and Delfiner, 2012) has not yet, to our knowledge, been applied in environmental studies.

2.2.2.1 Exploratory analysis and Gaussian anamorphosis

Conventional basic statistics, including maximum, minimum, mean, median, standard deviation (SD), skewness, and kurtosis were calculated to characterize the data distributions of the study variables. To facilitate the variogram modeling with skewed data distributions, before performing the geostatistical analyses, all variables were transformed into standardized Gaussian variables to obtain the mean of 0 and the standard deviation of 1. For this purpose, Gaussian anamorphosis (i.e. nonlinear change of variables to carry out the analyses in a Gaussian space) was performed. This technique consists in determining a continuous mathematical function (Φ) that transforms a random variable (Y), having a standardized Gaussian distribution, into a random variable (Z) with any distribution $Z=\Phi(Y)$. This was done by fitting a polynomial expansion of orthonormal Hermite polynomials truncated to a finite order (n) (Chilès & Delfiner, 2012):

$$Z = \sum_{i=0}^n \Psi_i \cdot H_i(Y)$$

Eq. (2-1)

where Ψ_i and H_i are Hermite coefficients and polynomials of order i , respectively. Function Φ is to be inverted to determine Y , i.e. $Y= \Phi^{-1}(Z)$.

2.2.2.2 Spatial interpolation

As a preliminary step to any multivariate spatial analysis, a co-regionalization dataset was generated while assuming that all variables were known at the sample locations. For this purpose, the raster (auxiliary) variable value of the nearest pixel was assigned to the sample location. Given the extension and complex morphology of the study region, it is expected that the assumption of spatial stationarity would not hold over the whole area. Therefore, the interpolation was carried out through the following three steps:

- i)* In the first step, the entire study area of Campania was classified into four macro-geographical units as will be described in Section 2.3.1;
- ii)* A variant of block cokriging on irregularly shaped geographical units, called “polygon cokriging”, was employed to determine the expected value and standard deviation of the Gaussian transformed variables for each unit.

Polygon cokriging is a mere extension of ordinary block cokriging when the block is of any shape (Goovaerts, 2008, Diacono et al., 2014, Castrignanò and Buttafuoco, 2020).

iii) The expected values were then used as local means in simple block cokriging with varying local means (Goovaerts, 1997), to provide continuous interpolation of the study variables over the whole study area.

Block cokriging is the standard geostatistical technique used to predict block averages from point-scale observations (Goovaerts, 1997). It is based on the calculation of the regularized (mean) block variogram, which requires discretizing the block in several regular cells on the centers of which the point variogram is computed. In the process of averaging the variogram over the block, the individual cell is assigned a weight that is proportional to the fraction of the cell that falls within the block (Goovaerts, 2008).

It is worth noting that simple block (co)kriging with varying local means (Goovaerts, 1997; Goovaerts, 2008, Castrignanò et al., 2009) differs from simple block (co)kriging, which requires a strong assumption of second-order stationarity for which the overall mean is constant and known. Under non-stationary conditions, the mean value was replaced for each variable by the expected value (local mean) estimated at each block as described in Section 2.2.2.2, point *iii*. This made it possible to take into account the lack of stationarity as represented by the partitioning of the study area into assumed homogeneous macro-geographical units. The estimate of each variable can then be written as the sum of the local mean and the estimate of the residual value from the local mean, the latter obtained by solving the simple block cokriging system where the covariance matrix is that of the residuals, not of the variables. The system can be expressed in terms of variograms instead of co-variances. To solve such a system, a linear model of co-regionalization (LMC) is fitted to the matrix of direct and cross variograms of residuals from local means (Journel and Huijbregts, 1978). LMC regards all the study variables as a realization of the same independent physical processes acting over different spatial scales. Accordingly, direct and cross-block variograms of the residuals are modeled as a linear combination of the same set of standardized variograms of unit sill, each corresponding to a specific scale (Goovaerts, 1997,

Castrignanò and Buttafuoco, 2020, Wackernagel, 2003). In particular, the variant multi-located block cokriging was used in this study to fuse the sparse soil variables with the gridded auxiliary variables. Multi-located block cokriging (Rivoirard, 2001, Castrignanò et al., 2009) is a simplified version of full cokriging, which employs the more densely sampled auxiliary variables only at the target point and at all locations where the soil variables are available.

The prediction quality of the LMC approach was assessed using cross-validation (Isaaks and Srivastava, 1989) consisting in removing one observation from the entire dataset and then providing the estimation at the same position using the remaining observations. The estimated value and the observed value are compared and the residual error at that position is computed. The cross-validation procedure was repeated for each position where an observation was made and N validity tests were thus generated. An assessment of the overall bias of estimation was obtained by computing the mean error (ME) statistic. Overall estimation precision was assessed by computing the mean-square standardized error (MSSE) statistic. The analytical expressions for the ME and MSSE metrics are reported below (Cressie, 1993, Carroll and Cressie, 1996):

$$\text{ME} = \frac{1}{N} \sum_{i=1}^N \{z(\xi_i) - z^*(\xi_i)\}$$

Eq. (2-2)

$$\text{MSSE} = \frac{1}{N} \sum_{i=1}^N \left\{ \frac{z(\xi_i) - z^*(\xi_i)}{\sigma(\xi_i)} \right\}^2$$

Eq. (2-3)

where N is the number of observations, σ is the block cokriging standard deviation, whereas z and z^* are the observation and estimate at the vector position ξ_i , respectively. If the estimate is unbiased, the former statistic [i.e. ME Eq. (2-2)] should be as close to zero as possible. Instead, for the estimate to be precise (a measure of the degree of dispersion), the latter statistic [i.e. MSSE Eq. (2-3)] should be within the heuristic tolerance interval $\left(= 1 \pm 3\sqrt{2/N} \right)$ (Chilès and Delfiner, 2012).

2.2.2.3 Support correction and uncertainty assessment

As mentioned above, all estimates were obtained for Gaussian transformed variables. To back-transform the variables into the original units, the inverse transformation of Gaussian anamorphosis was applied while accounting for the change of support. One of the advantages of using Hermite polynomial expansion for anamorphosis modeling is that it is possible to modify this function for change of support scaling the anamorphosis function by one global support coefficient, r , that shall be determined in such a way that the block variance matches that estimated (Harding and Deutsch, 2019):

$$Z_v(\xi) = \sum_{i=0}^n \{\Psi_i \cdot r \cdot H_i[Y(\xi)]\}$$

Eq. (2-4)

where Z_v refers to the variable on the block v . The global correction coefficient (r) was computed using the following equation (Chilès and Delfiner, 2012):

$$var [Z_v(\xi)] = \sum_{i=0}^{\infty} \Psi_i^2 \cdot r^2$$

Eq. (2-5)

for the estimated block variance. This was calculated as the difference between the point variance, obtained from the sill of the direct variogram model of the raw variable, and the average variogram within the block, obtained through the regularization process previously described (Journel and Huijbregts, 1978).

Finally, the estimation uncertainty was assessed by computing the 95% confidence interval (i.e. CI95%) of the Gaussian transformed variable. This interval contains the true mean of the estimated Gaussian variable (EV) with a probability level of 0.95. More specifically, at each node of the interpolation grid, CI95% was calculated as the difference between the upper limit (UL95%=EV+1.96×SD) and the lower limit (LL95%=EV−1.96×SD), where SD is the estimation standard deviation. To obtain CI95% of the raw variable, the lower and upper limits of the Gaussian variable were back-transformed using the previously calculated block Gaussian anamorphosis model (Eq. (2-4)). For strongly skewed variables it is expected that CI95% may be strongly asymmetric. A relative estimate of uncertainty (in percentage terms) was computed using the following ratio:

$$Uncertainty = \frac{(UL95\% - LL95\%)}{EV} \times 100$$

Eq. (2-6)

where all symbols refer to the raw variable.

All geostatistical analyses were performed using ISATIS software (Geovariances, 2018).

2.2.3 Composite indicators of soil behavior

Soil quality and resilience in the study region were assessed by computing the following two composite indicators that combine the regional estimates of the seven primary soil variables (sand and clay contents, oven-dry bulk density, rock fragment content, soil organic matter content, calcium carbonate content, and pH): 1) Soil organic carbon stock (SOCS), and 2) Recharge transit time (τ_R).

2.2.3.1 Soil organic carbon stock (SOCS) as a composite indicator of soil quality
According to Popleau et al. (2017), SOCS was computed using the following relation:

$$SOCS = BD \times SOC \times D \times \left(1 - \frac{RF}{100}\right)$$

Eq. (2-7)

where D (cm) is soil depth, assumed in this study as a constant and equal to 20 cm.

2.2.3.2 Recharge transit time (τ_R) as a composite indicator of soil resilience

Assessing the transit time for the travel of infiltrated water moving through a soil profile to reach the water table can be conveniently viewed as an indicator of the physical resilience of soil (Boumaiza et al., 2021). A map of the mean annual depth to the groundwater table, D_{GW} , (all lengths are expressed in cm to ensure consistency) is available for the Sele River plain, which is the second largest river in Campania and where the groundwater is known to be quite vulnerable to nitrates (Tufano et al., 2020, Nasta et al., 2021a). Therefore, for illustrative purposes only, we restricted our analysis to this zone to compute the recharge transit time, τ_R (d), along a hypothetical uniform soil column. According to Batsukh et al. (2022), τ_R is defined as follows:

$$\tau_R = D_{GW}/c$$

Eq. (2-8)

where c (cm d⁻¹) is the soil moisture vertical velocity defined as follows:

$$c = \frac{K_s(1 - S_f^m)^2}{2(\theta_s - \theta_r)S_e^{1/2}} \cdot \left[1 + \frac{4S_e^{1/m}S_f^{m-1}}{(1 - S_f^m)} \right]$$

Eq. (2-9)

and with S_e and S_f computed as follows:

$$S_e = \frac{(\theta - \theta_r)}{(\theta_s - \theta_r)} ; S_f = 1 - S_e^{1/m}$$

Eq. (2-10)

where θ (cm³ cm⁻³) is the volumetric soil water content across the soil profile (assumed uniform), and θ_r (cm³ cm⁻³), θ_s (cm³ cm⁻³), α (cm⁻¹), n (-), m (-), K_s (cm d⁻¹) are the parameters of the soil water retention and hydraulic conductivity functions described by the van Genuchten (VG) relations (van Genuchten, 1980). The VG hydraulic parameters can be estimated using well-established pedotransfer functions (PTFs) from the knowledge of easily-retrievable soil properties, namely the oven-dry bulk density, and the sand, clay, and soil organic carbon contents. Recently, Nasta et al. (2021b) found that the PTF proposed by Weynants et al. (2009), based on the previously mentioned soil properties, outperformed other available PTFs by using three large data sets in Europe. Since the soil water content, θ , is unknown across the uniform soil profile, we calculated the block-specific mean recharge transit time, τ_{RM} , as the geometric mean (with τ_R expressed in years) obtained at preselected θ steps (in the range between θ_r and θ_s).

2.3 Results and discussions

2.3.1 Splitting Campania into representative land units (RLUs)

Before conducting geostatistical modeling, we carried out the preliminary task of splitting the entire territory of Campania into a limited number of geographical units (referred to as representative land units, RLUs), reflecting similar characteristics in pedology, hydrogeology, and geomorphology within them, but with an evident level of diversity between them. There was also the need to ensure that each unit was large enough to contain a similar number of the available sampled locations. To meet such requirements, we used a hierarchical sequence of physical information that enabled us to delineate the four RLUs depicted in Figure 2-2 (left).

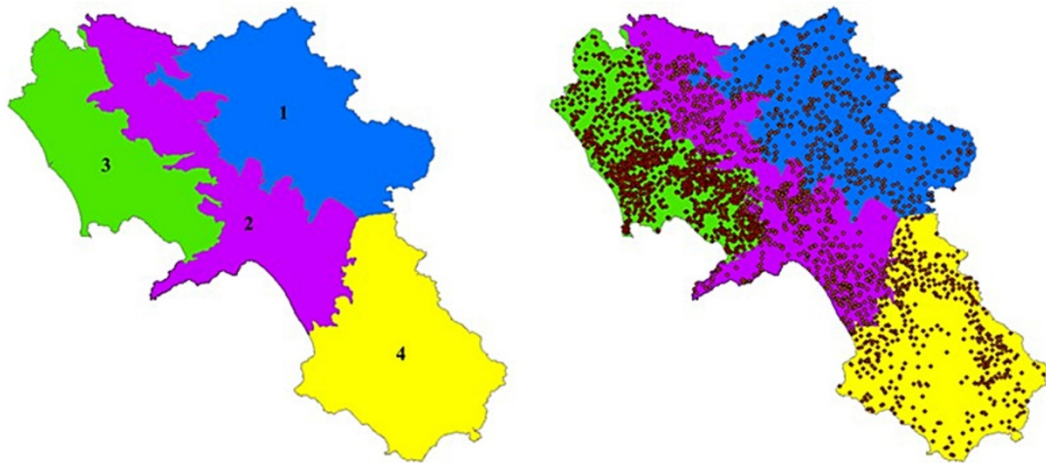


Figure 2-2 Map of the four representative land units (RLUs) identified in Campania (left); 3,316 sampling positions distributed within the four RLUs (right).

The first step in this task was performed by using general information and relevant maps regarding the geolithological (Guarino et al., 2022) and hydrogeological (De Vita et al., 2018, Cusano et al., 2022) features of Campania. These maps allow identification of the larger rock groups in the study region yielding the following main landscapes: coastal alluvial plains (mainly those of the Volturno and Sele rivers, also evident in Figure 2-1 and located in RLUs #3 and #2–4 of Figure 2-2), volcanic units (RLU-3 of Figure 2-2), carbonate Apennines (mainly RLU-2 of Figure 2-2), and siliciclastic rocks and flysch materials (mainly RLU-1 and some southern zones of RLU-4). General pedological features were then superimposed by using the study by Costantini and Dazzi (2013) that identified the following major areas in Campania: 1) Cambisol-Andosol region with Regosols of central

Italy (Lazio, Mt. Vesuvio), 2) Cambisol-Leptosol region with Luvisols of the southern Apennines, and 3) Cambisol-Regosol region with Luvisols of eastern Italy (east and south-east part of the Apennines). Volcanic soils represent a very specific feature of Campania and reference was made to the study by Terribile et al. (2007) that enabled us to delineate the major volcanic complexes (Campi Flegrei, Somma-Vesuvius, Roccamonfina) and relevant andic soils covering large parts of RLU-3. A subsequent step in the use of a hierarchical sequence of information was carried out with the regional map of agricultural land uses (Regione Campania, 2009). Di Gennaro et al. (2002) identified in Campania 30 soil-landscape units differing in pedological, ecological, and landscape characteristics, and mapped the land systems for the entire region (scale 1:250.000).

All the above-mentioned levels of information are mainly linked to general topographical, geological, and soil-landscape features of the study region. In light of the purpose of the present study, an additional layer of information was retrieved from the paper by Palladino et al. (2022) who analyzed a large dataset of oven-dry soil bulk density values collected over the entire region of Campania. Exploiting the specific hierarchical analyses carried out by Palladino et al. (2022) we were able to further refine the outcome of the previous general grouping steps and finally identify the four RLUs depicted in Figure 2-2a.

The locations of the sampling sites in each of these RLUs are shown in Figure 2-2b. Using the values of clay content (%Clay) and oven-dry soil bulk density (BD) measured in each unit, we performed the statistical analysis of variance (ANOVA), assuming independence of sample data, to test in a fairly simplistic way whether the differences among the means of %Clay and BD of the four land units were significant at 0.05 probability level. In all the cases considered (results not shown for brevity), we rejected the null hypothesis that at least the means of percent clay and BD did not differ among the four RLUs.

2.3.2 Mapping primary soil properties and associated uncertainties

The basic statistics of the seven soil physical and chemical variables (sand, clay, BD, SOM, RF, CaCO₃, and pH) and five terrain attributes (*z*, slope, PlanC, ProfC, FA) comprising the co-regionalization dataset are reported in Table 2-1. It is worth

pointing out that the statistics for the auxiliary variables (i.e. the terrain attributes, originally in raster format), refer only to the pixels closest to the soil samples. Visual inspection of this table shows that most of the terrain attributes are characterized by a relatively large variability, especially those linked more to the topography and morphological features of the study region. In addition, almost all the data distributions were non-centered and with the shape parameters of skewness and kurtosis that deviated significantly from those of a Gaussian distribution, which could be partly attributed to the presence of outliers. The above comments justify the normalizing and standardizing transformations performed on the twelve variables before running the geostatistical analysis.

Table 2-1 Count, minimum (Min), maximum (Max), mean, median, standard deviation (SD), skewness, kurtosis of clay, sand, organic matter (OM), rock fragment (RF), calcium carbonate (CaCO₃), soil bulk density (BD), pH, elevation (z), slope, flow accumulation (FA), plan curvature (PlanC) and profile curvature (ProfC) for soil samples collected in the entire region of Campania.

Variable	Unit	Count	Min	Max	Mean	Median	SD	Skewness	Kurtosis
Clay	%	2,855	0.29	70.85	24.14	21.99	14.94	0.6	2.61
Sand	%	2,855	0.85	97.48	38.21	36.87	18.48	0.34	2.51
SOM	%	2,802	0.070	24.27	3.73	3.11	2.45	1.94	9.05
RF	%	2,791	0.00	48.51	6.09	3.18	7.49	2.16	8.58
CaCO ₃	%	2,791	0.15	61.22	8.44	7.0	5.68	3.15	18.43
BD	g cm ⁻³	2,847	0.54	2.65	1.24	1.25	0.20	-0.1	3.63
pH	-	2,791	5.90	11.82	6.86	6.6	0.88	3.78	18.73
Z	m	2,791	1.00	1,633	240.14	138	251.73	1.2	4.16
Slope	degrees	2,855	0.00	40.45	4.97	2.62	6.01	1.81	7.03
FA	-	2,741	0.00	491	18.09	3	49.32	5.36	36.75
PlanC	-	2,855	-0.59	1.15	0.00	0.00	0.07	2.64	54.03
ProfC	-	2,855	-1.00	1.04	0.01	0	0.07	0.98	44.14

Careful examination of Pearson's correlation matrix reported in Table 2-2 reveals the generally low correlations among the primary soil variables. Low correlations also occur among these primary variables with the auxiliary terrain attributes, except for the significant negative correlation between clay and sand contents. However, this situation should not discourage undertaking multivariate analysis inasmuch as what Pearson's coefficient measures is only the linear component of the correlation between the variables while assuming the independence of the samples. Given the complexity of the region under study, as also highlighted by the presence of outliers, nonlinearity and local variability in the relationships between

the variables should be expected. Therefore, the variables were preliminarily Gaussian-transformed without removing outliers once the reliability of all the measured data was verified.

Table 2-2 Correlation matrix between clay, sand, organic matter (OM), rock fragment (RF), calcium carbonate (CaCO₃), bulk density (BD), pH, elevation (z), slope, flow accumulation (FA), plan curvature (PlanC) and profile curvature (ProfC) for soil samples collected in the entire region of Campania.

	Clay	Sand	SOM	RF	CaCO ₃	BD	pH	z	Slope	FA	PlanC	ProfC
Clay	1											
Sand	-0.83	1										
SOM	-0.07	0.06	1									
RF	-0.07	0.21	0.27	1								
CaCO ₃	0.17	-0.15	0.15	0.06	1							
BD	0.17	-0.1	-0.35	-0.16	0.17	1						
pH	0.11	-0.07	0.25	0.04	0.3	0.01	1					
Z	0.23	-0.12	0.24	0.16	0.02	-0.08	-0.04	1				
Slope	0.02	0.05	0.25	0.27	0.03	-0.17	-0.05	0.59	1			
FA	-0.04	0.00	0.00	-0.02	0.00	0.00	0.03	-0.06	-0.12	1		
PlanC	0.03	0.00	-0.01	0.00	-0.03	0.02	0.00	0.05	0.03	-0.14	1	
ProfC	-0.03	0.03	0.05	0.05	0.02	-0.06	0.00	0.00	0.13	0.05	-0.42	1

Gaussian anamorphosis was applied with a series of Hermite polynomials truncated to the first 100 terms (i.e. $n=100$ in Eq. (2-4)), obtaining for all variables symmetric distributions with mean zero and variation range between -3.44 and $+3.44$. As there were no significant differences between the directional variograms, an isotropic point LMC was first adapted to the set of experimental direct- and cross-variograms of the Gaussian-transformed variables. The model consisted of three spatial structures: the nugget effect, a spherical model with a 30,000-m range, and a spherical model with a 70,000-m range. Each spatial component explained a proportion of the spatial variance of 50%, 18%, and 32%, respectively. The unstructured component (nugget effect) accounted for half of the total variability, a situation which, despite the large sample size, may be due to the too-coarse sampling scale in relation to the heterogeneity of the study area. The remaining spatially correlated variation was split into two components at different scales with an evident prevalence of the longer-range component.

The prediction quality was verified for the seven primary soil variables using the point LMC since the support of the observations of soil attributes was punctual.

Cross-validation was performed on 2,600 samples, using simple cokriging with spatially variable means obtained by applying block cokriging. The cross-validation results shown in Table 2-3 are referred to as the only robust data, i.e. those estimates whose standardized errors lie in the range $[-3.5; +3.5]$, thus excluding the most extreme outliers, which were always in the order of tens. Examination of Table 2-3 shows that ME was always very close to zero and MSSE fell within the tolerance interval, $[0.915; 1.10]$, except for the Gaussian-transformed variable of BD and RF, whose values were slightly higher than the upper limit. Given the differences in spatial support between the primary variables (centimeter scale) and the auxiliary variables (75-m scale), it was first necessary to regularize the point variograms and then fit an LMC on 75-m \times 75-m blocks (the size of the DEM cell). The fitted block LMC included the following spatial structures: nugget effect, a spherical model with a range of 29,996.03m, and a spherical model with a range of 70,011.36m, explaining 9%, 34%, and 57% of the total variance, respectively. Therefore, the change in spatial support produced the following effects:

- A drastic reduction in the total variance from 12.94 to 6.64 (so about half the initial value);
- A reduction in the unstructured component due to the averaging operation, with a considerable increase in the proportion of the multi-scale structured component (about 91% of the total block variance).

Table 2-3. Model performance in terms of mean error (ME) and mean standardized square error (MSSE) for the Gaussian data of Clay (g Clay), Sand (g Sand), SOM (g SOM), BD (g BD), RF (g RF), CaCO₃ (g CaCO₃), pH (g pH).

variable	ME	MSSE
g Clay	0.019	1.06
g Sand	0.004	1.01
g SOM	0.016	1.02
g BD	0.009	1.16
g RF	0.009	1.15
g CaCO ₃	0.0002	1.02
g pH	0.052	0.959

The mathematical models standardized to the unit sill for the two spatial scales remained practically unchanged, with the short-range component proportionally a little more than half that of the long-range component.

The block LMC after performing the regularization process is shown in Figure 2-3, with a very good fit mainly due to the averaging process of the point variograms. The strength of the spatial relationship between pairs of variables can be assessed by the distance of the model (bold line) from the dashed line representing the intrinsic (maximum) correlation (Wackernagel, 2003). It is worth noting that the spatial relations derived from the block LMC refer to Gaussian transforms. However, it is assumed that Gaussian anamorphosis does not alter the geometric distribution of spatial dependence structures. Therefore, these relations can also be extended to raw variables. A generally weak spatial correlation between the primary and auxiliary variables is quite evident, probably due to the original difference between the two supports.

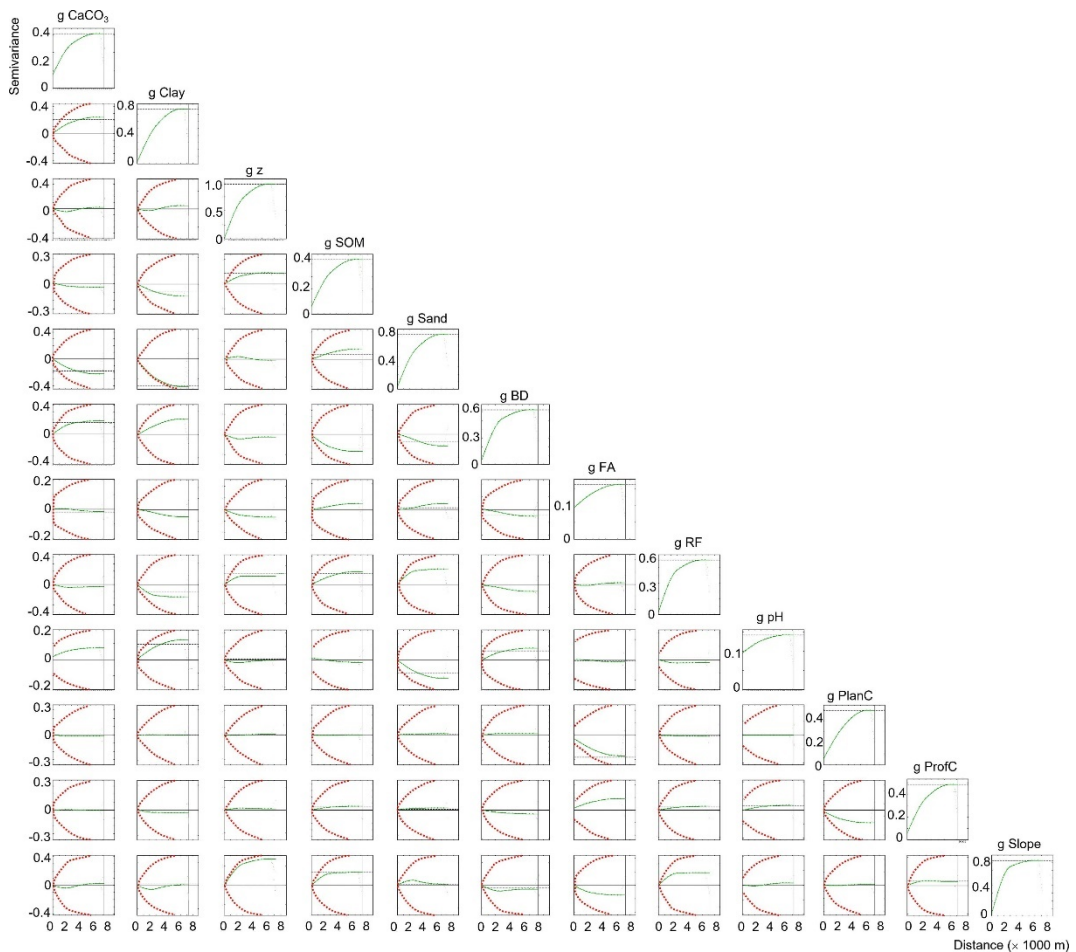


Figure 2-3. Auto- and cross-variograms of the block linear model of co-regionalization for the Gaussian data of CaCO₃ (g CaCO₃), Clay (g Clay), z (gz), SOM (g SOM), Sand (g Sand), BD (g BD), FA (g FA), RF (g RF), pH (g pH), PlanC (g PlanC), ProfC (g ProfC), and Slope (g Slope). The green points are the experimental values whereas the red dotted lines are the model of co-regionalization. The vertical lines are the hull of perfect correlation, whereas the horizontal dashed lines are the experimental variances.

A positive correlation was found between volumetric rock fragment (RF) and elevation and slope, whereby zones at higher altitudes are usually characterized by a larger amount of coarse material. Clay content was positively correlated with BD, CaCO₃, and soil pH, but negatively correlated with RF, SOM, and sand content. For the other variables, it may be of interest to highlight the negative relationships of BD with SOM and RF, the positive relationship with pH, as well as the positive relationship between RF and SOM. Many of these relationships might be explained as a function of position in the landscape and might also vary locally.

All of the above comments make it clear that the regularization process resulting from the change of support had a considerable effect on statistics. Therefore, this justifies the calculations done to change point anamorphosis into block anamorphosis to convert block co-kriging estimates of Gaussian-transformed variables into raw variables.

As noted above, and from a perusal of Table 2-4, the block variance was low compared to the point variance, the latter calculated from the sill of the direct variogram of the raw variable, especially for CaCO₃, SOM, and pH; the difference between the two variances is represented by the within-block mean variogram [$\gamma(v,v)$] (Figure 2-3). In the case of soil pH, the greatest total variance was within-block variance due to the relatively large stochastic component, more than 67% of the sill of the direct variogram. This is also reflected in the correction coefficient r , which was close to 1.0 for the clay, sand, and rock fragment contents (which were better spatially-structured variables), but much smaller for CaCO₃, SOM, and especially for soil pH.

Table 2-4. Results of Block Support correction for the selected soil variables: clay, sand, organic matter (OM), rock fragment (RF), calcium carbonate (CaCO₃), bulk density (BD), pH.

	CaCO ₃ %	Clay %	SOM %	Sand %	BD g cm ⁻³	RF %	pH -
Point Variance	32.27	223.32	5.99	341.37	0.04	56.05	0.76
Variogram Sill	32.4	254.55	6.36	438.85	0.04	56.36	0.75
$\gamma(v,v)$	25.57	56.72	3.72	95.63	0.02	22.85	0.72
Block Variance	6.7	166.6	2.27	245.74	0.02	33.2	0.04
Block Support Correction (<i>r</i>)	0.5139	0.8697	0.6463	0.8512	0.7552	0.8078	0.3062
Block Zmin	0.8	0.29	0.11	0.85	0.54	0	6.19
Block Zmax	47.71	70.85	22.38	97.48	2.62	48.5	9.37
Block_Mean	8.36	28.8	3.54	32.72	1.27	5.12	6.85
Point Zmin	3.95	1.87	0.65	2.51	0.71	0	6.42
Point Zmax	27.02	70.74	11.75	83.65	1.68	33.75	7.04
Point Mean	7.64	29.55	3.31	31.59	1.28	4.63	6.68

As might be expected, the change of support affected not only the total variance of estimates but also the shape of their histogram. The differences detected in the estimated histograms (see the left panel in Figure 2-4) were due to diversities in the two models of point or block anamorphosis (right panel in Figure 2-4). Whereas for the clay and sand contents such differences were not considerable, for SOM, CaCO₃, and RF they became significant, especially for values above approximately the average: for the same Gaussian estimate, the raw value obtained with the point model was significantly higher than that with the block model, the reverse for below-average values. Soil oven-dry bulk density and pH deserve a separate discussion, as the differences between the two models became very large only for extremely high values, the reliability of which should, however, be verified.

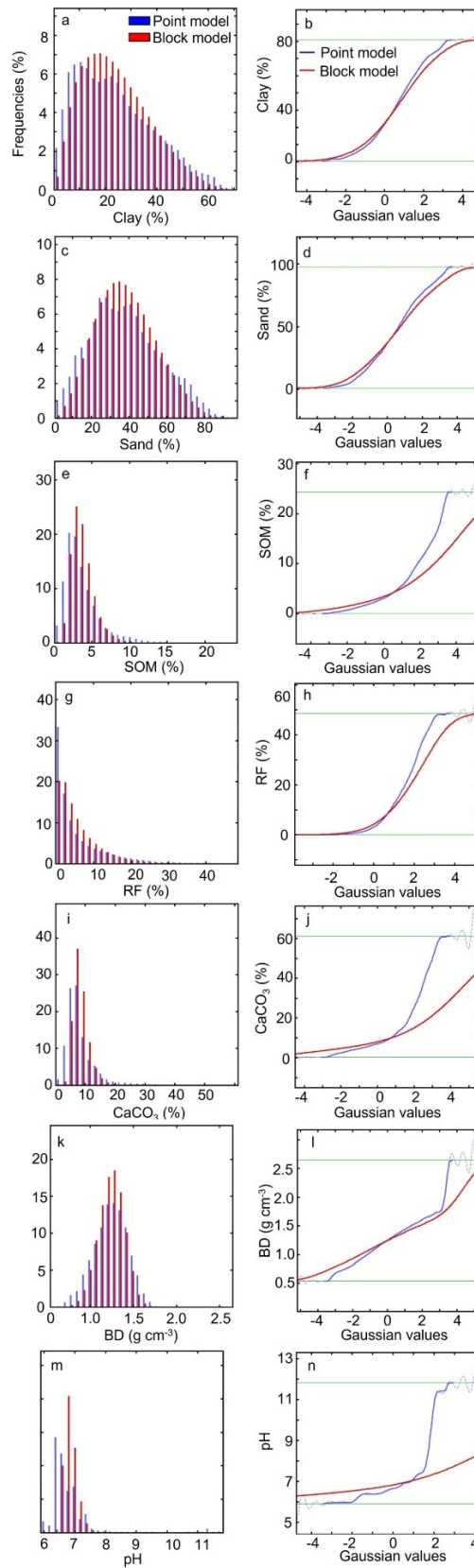


Figure 2-4. Histograms of a) Clay, c) Sand, e) SOM, g) RF, i) CaCO₃, k) BD, m) pH; Anamorphosis of b) Clay, d) Sand, f) OM, h) RF, j) CaCO₃, l) BD, n) pH. Point and block models are denoted by blue and red colors, respectively.

To summarise, whereas the estimate of the overall mean value is virtually not distorted by using data with different supports, the dispersion from the sample mean is instead underestimated in a way that may depend on the sample volume considered. Therefore, this affects the total variance of the data in a statistically predictable way. However, the critical aspect that comes into play is that the change of support also affects the extreme values of the statistical distributions and the probabilities of exceeding preselected threshold values (Lajaunie and Wackernagel, 2000). In agriculture, as an example, the probability that the local soil–water contents and/or nitrate concentrations take on values below critical thresholds can be a criterion on which a decision is based whether or not irrigation or fertigation is applied. This probability is highly dependent on the shape of the histogram. This is a reason why it is of crucial importance to account for the change-of-support problem when dealing with issues of site-specific management occurring in precision agriculture.

Figure 2-5 shows the maps of the estimates (EVs, expected values) of the seven primary soil variables (CaCO_3 , Clay, SOM, Sand, BD, RF, pH) with the associated maps of uncertainty expressed in percentages Eq. (2-6). In general, the EV values were strongly influenced by the topography of the study region and by the selected four RLUs reflecting fairly similar landscape features within each of them. Concerning CaCO_3 , the following units can clearly be distinguished: one in the northwest and the other in the south characterized by the lowest values, whereas the central and northeastern areas had the highest values. With respect to the uncertainty, there was a positive relationship with the estimate in the northern portion that became negative in the southern portion. The map for clay content shows a great similarity with that of CaCO_3 in the northern part of the region, but the opposite occurs in the southern portion. The uncertainty map appears rather fragmented and shows a reciprocal function with that of the estimates. In general, the highest SOM values occurred in the more elevated areas, except for a zone in the northeast where the lowest values were recorded. Overall, the regional distribution of SOM tends to take on lower values in the main lowlands of Campania, i.e. the Volturno and Sele river plains (see the land-use map of Figure 2-6b), which could be attributed to the presence of intense agricultural practices that

can enhance the decomposition of organic matter, perhaps exacerbated by non-optimal on-farm tillage practices. With regard to the uncertainty of SOM, a generally positive relationship occurs with the estimate except for the northeast portion of the region where a reciprocal function was detected.

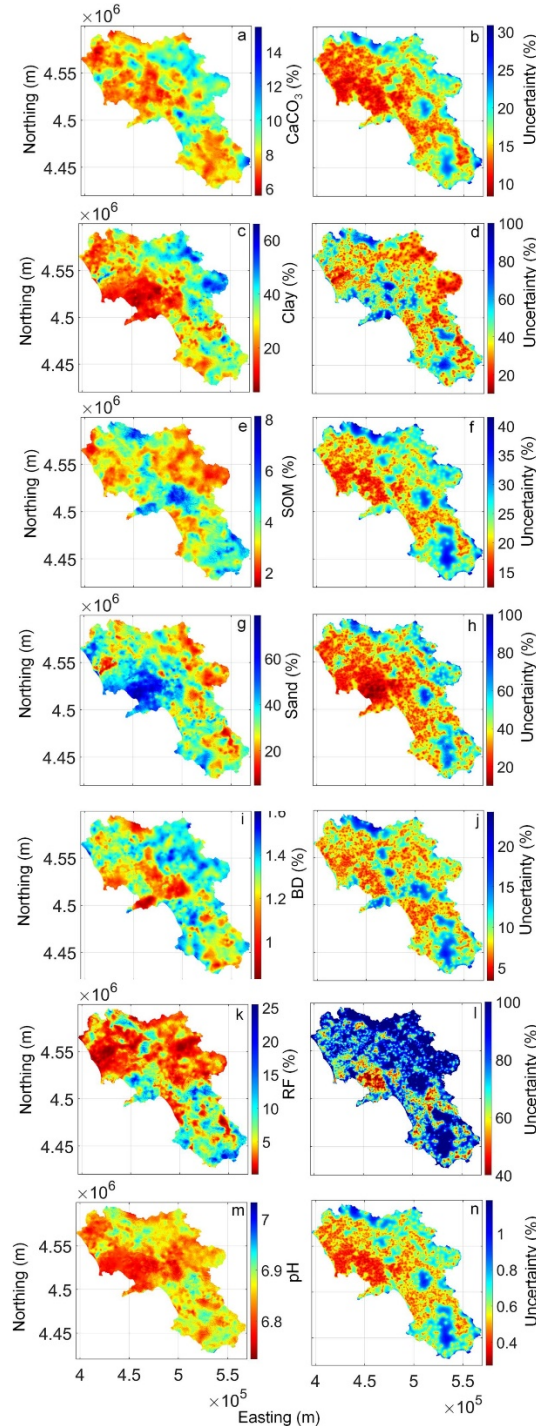


Figure 2-5 75-m-grid-size maps of expected values of a) CaCO₃, c) Clay, e) SOM, g) Sand, i) BD, k) RF, m) pH; and corresponding uncertainty of b) CaCO₃, d) Clay, f) SOM, h) Sand, j) BD, l) RF, n) pH.

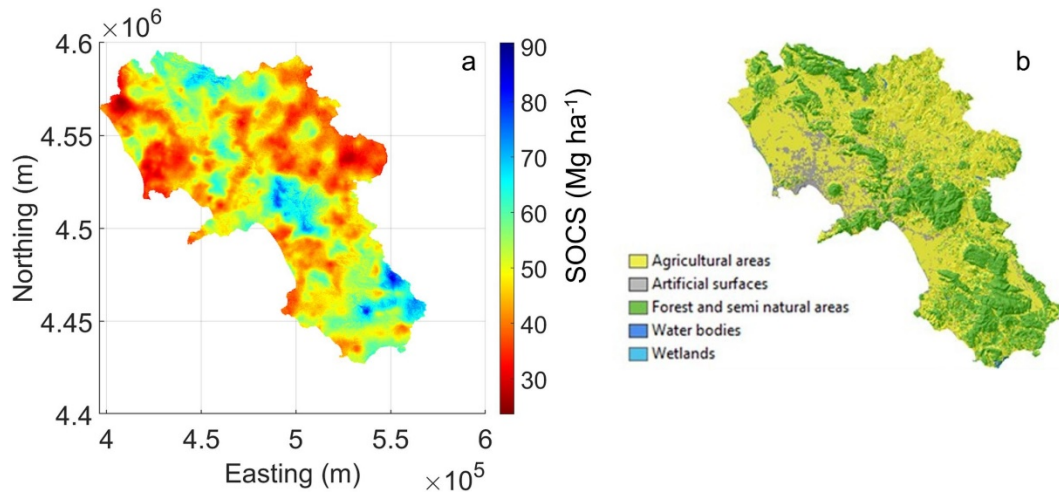


Figure 2-6. a) 75-m-grid-size map of near soil surface soil organic carbon stock (SOCS), b) land use map referred to 2018 (downloaded from the Copernicus Land Monitoring Service website).

The map for sand content reveals a reciprocal function with the clay map, with a wide area characterized by the highest values located around the Gulf of Naples, whereas the lowest values occurred at the highest altitudes. The uncertainty map of sand content can be roughly divided into two distinct parts according to the median longitudinal line marked by the chain of the southern Apennines: the western part of the region with the lowest uncertainty values and the eastern part with the highest uncertainty values.

The map of oven-dry soil bulk density (BD) appears rather patchy, which makes it rather difficult to distinguish the beneficial impact of the preliminary grouping of the region into the four representative land units to account in some ways for the deterministic component of variability causing nonstationarity. In general, the densest soils occurred at the highest altitudes, but this property was sometimes locally reversed. The same fragmentation observed in the estimation map is reflected in the related uncertainty map. However, as a trend, for less dense soils the uncertainty was greater and vice versa.

The RF map can be divided into two parts: the northern zone with lower values (less than 5%), and the southern zone with higher average values and peaks of 20–25%. The area around the Gulf of Naples displayed values varying between 10% and 25%. In general, the computed uncertainties were rather large, with values varying between 80% and 100%, except for a) the Gulf of Naples area, b) a central area,

and c) another area located in the southeast, where the uncertainty values ranged between 40% and 60%.

Finally, the soil pH map indicates low variability in absolute terms. Nevertheless, the variability of pH can roughly be split into three main units: those in the north and south characterized by the highest values on average, and the central unit with the lowest values. The uncertainty map shows a certain degree of fragmentation. However, the greatest uncertainties were in the higher areas, whereas the lowest uncertainties occurred in the broad coastal plain surrounding the Gulf of Naples and where soil pH takes on smaller values.

2.3.3 Mapping compound indicators of soil behavior

For the sake of illustrative purposes only, we discuss here the outcomes of mapping the two compound indicators presented in sub-section 2.2.3.1 and 2.2.3.2:

- the stock of SOC (SOCS), which is more relevant to soil quality and can help evaluate the greater or lesser ability of soil to provide ecosystem services (Szatmári et al., 2021);
- the recharge transit time (τ_R), which can be particularly efficient when assessing soil resilience to groundwater pollution and pest management (Mattern and Vanclooster, 2010).

This was simply done to illustrate the importance that the estimation of the variables studied can have when characterizing the environmental quality of an area or designing a suitable recovery plan. It is by no means intended to assess how the uncertainty in the input variables propagates into the prediction of the two calculated compound indicators. This would require the application of stochastic simulation (Heuvelink, 1998), but that lies beyond the scope of the present article. Figure 2-6a shows the distribution in the entire region of Campania of soil organic carbon stock (SOCS) as computed by Eq. (2-7) up to a soil depth of 20cm. The distribution map of topsoil SOC stocks accounts obviously for the spatial variations of SOC in the region (see panel *e* of Figure 2-5) but is also affected by the distributions of the BD and RF variables. Topsoil SOCS values are higher along the Apennine ridge, located in the central NW-SE part of the region, where the elevations are greater (mostly in RLU-2 and the NW-SE band of RLU-4).

Therefore, elevation does exert control on SOCS even under different land uses. The land-use situation in Campania in the year 2018 is shown in Figure 2-6b. Other zones in Campania with the presence of relatively low SOCS values are those of the inland (mainly clayey) hills that characterize larger portions of RLU-1. The volcanic soils that occupy large portions of RLU-3 have relatively low clay contents. In addition, the oven-dry bulk density values of these soils are usually quite low (often even less than 1.0gcm^{-3}). The comments about the typical values of % clay and BD for volcanic soils mainly explain the relatively low values of the computed topsoil SOCS that characterize large portions of RLU-3.

Figure 2-7 shows the spatial patterns of mean recharge transit time for the case study of the shallow groundwater underlying the coastal plain zone on the right side of the Sele River. This map reports the block-specific geometric (τ_{RM}) and shows that most of this study area is affected by relatively high values of τ_{RM} , especially in the northeast part and along the NW-SE band. These zones are both characterized by the presence of arable luvisols and cambisols with relatively high contents of clay-sized particles in the uppermost soil horizons. Instead, the coastal dune facing the Tyrrhenian Sea has a lower τ_{RM} . This zone is mainly characterized by fluvisols whose dynamics of sediment deposition have affected the transit time of water and solutes toward the local groundwater that is very shallow near the sea.

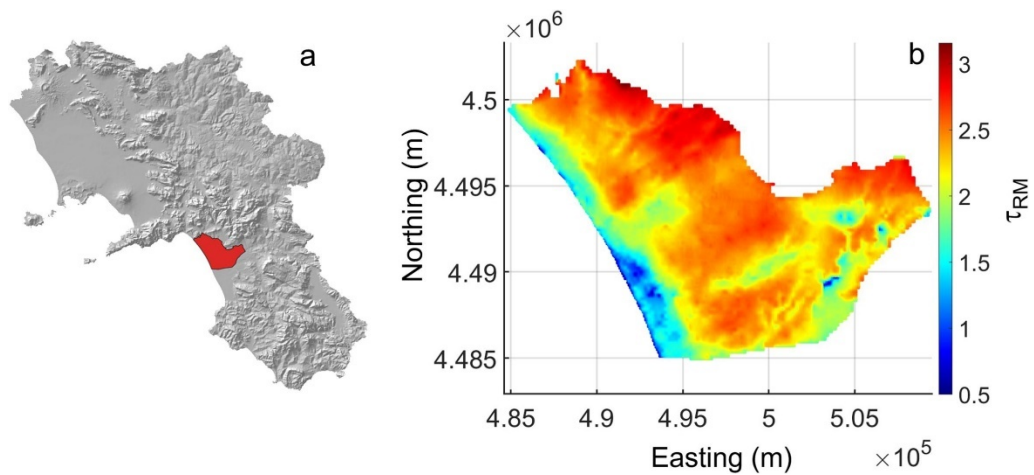


Figure 2-7. a) Geographical position of the Sele River plain (red polygon) in Campania (hillshade), b) 75-m-grid-size map of mean recharge transit time, τ_{RM} .

As mentioned already, these maps have been drawn with the sole aim of illustrating the importance of efficient and reliable estimations of primary soil variables in the characterization of soil functions over a region. We would warn the reader that the maps lack the estimation of the relevant uncertainty, which should be carried out through an analysis of the propagation of uncertainty, namely the effect that the uncertainties in the measurands (in our case, the primary soil properties) exert on the uncertainty of the analytical expression based on them [in our case, Eq. (2-7) and Eq. (2-8)] and used to determine the compound indicators. However, such an assessment would have required the application of stochastic simulation (Heuvelink, 1998), but this issue does not come within the objectives of the present study.

2.4 Concluding remarks

The results presented in this study emphasize the fact that disregarding a change of spatial support has non-negligible effects in determining the uncertainty (variability) and the occurrence of extreme values (minima and maxima) in the datasets. Instead, the central values of the probability distributions do not seem to suffer significant negative effects. Therefore, attention should be paid to adequately assessing the change-of-support problem when the goal of an investigation is to perform risk analysis and determine the likely occurrence of adverse events. These tasks involve the calculation of the probability of whether or not threshold values are exceeded, which is a primary interest in decision-making when dealing, for example, with precision farming or land restoration problems.

No map providing spatial information about soil parameters and functions is free from errors that can arise from different sources, mainly due to measurement errors and interpolation techniques, or resulting from differences in spatial support between the observations and the estimates. To be able to judge whether a given soil map is suitable for a particular use, a prerequisite is to quantify the uncertainty of the estimates and communicate it to professionals, end-users, and stakeholders. This is particularly necessary in the case of environmental mapping, where only an overall measure of accuracy is provided. To calculate uncertainty, a preliminary unambiguous definition of uncertainty is needed since there is no unanimous consensus in the scientific community.

By using a geostatistical approach based on probability distributions, this study showed how uncertainty can not only vary from point to point on a map but also how, especially for some soil variables, it can be particularly sensitive to the change in the size of the area (or volume) over which the observations were measured and the estimates averaged. The approach presented in this study is based on solid statistical and geostatistical theories, allows characterization of the uncertainty in detail, and evaluates how uncertainty depends on both the position and the support of the estimates compared with that of the observations. The proposed approach can be transferred not only to other disciplines in the field of environmental sciences, such as climatology, ecology, and hydrogeology but also to the health sciences which today more than in the past deal with mapping disease incidence. Moreover,

it is helpful to those who should use a soil map, whether practitioners or planners, to derive performance indicators that synthesize the bulk of available information. We also set ourselves the objective to show how the effort to measure numerous soil properties and exploit auxiliary variables (mainly related to the morphology of the territory under study) can be profitably combined within a geostatistical framework to derive compound indicators of soil functions at a regional scale. The maps of the stock of soil organic carbon (SOCS) and recharge transit time (τ_R) were drawn to show how the information content of primary soil properties and auxiliary terrain attributes can be fruitfully related to the functions that the soil itself is able to provision. These soil function maps, however, do not provide indications of the associated uncertainties. Addressing the problem of computing the propagation of uncertainties from the primary soil properties to the soil function indicators requires the use of techniques based on stochastic simulations, which will be the main topic of a subsequent article.

3 Using a transdisciplinary approach to better describe dominant agro-hydrological processes in two basin agro-forest ecosystems.

3.1 Introduction

According to IPCC estimates (IPCC, 2022), the regions of the Mediterranean area characterized by wet and mild winters and hot and dry summers (Mediterranean climate) are particularly vulnerable to climate change.

Most of its subtypes can be classified as semi-arid, and rain crops are generally exposed to water-scarce conditions (Aguilera et al., 2020). Indeed, serious concerns relate to water availability to support human health and activities.

Mediterranean climate areas are expected to experience shorter-than-normal winters and a decrease in summer rainfall, which could result in greater vulnerability to extreme events, i.e., more floods in winter and more droughts, fires, and water shortages in summer (Alessandri et al., 2014). Water is an essential component for providing a series of hydrological ecosystem services (HES), such as drinking water, food, or climate regulation. HES are defined by Brauman et al., 2007 as "all the benefits that ecosystems provide by regulating the hydrological cycle." HES procurement is based on so-called blue and green water flows (Willaarts et al., 2012)

Given the global change, there is particular attention to the long-term partition of blue waters, and green water flows to improve the management of a territory's water resources. "Green water" refers to the amount of rain infiltrated and stored in the root zone of the soil that supports the primary productivity of natural and agricultural systems through evapotranspiration. "Blue water" is the amount of precipitation that exceeds the storage capacity of the earth that flows downstream to feed rivers, lakes, and aquifers. However, few studies still exist that project the likely relative effects of climate change and land use on blue and green water flows with their associated predictive uncertainties (Smith et al., 2021). In regions subject to extreme climatic conditions, these flows need to be better quantified to support sustainable long-term land and water use policies for anthropogenic (drinking water

extraction and irrigation) and natural (forests, wetlands, and in-stream). Improving understanding of water's roles in ecosystem functioning requires an integrated approach between hydrologists and ecologists (Bonacci et al., 2009). A new discipline, ecohydrology, has been proposed to demonstrate the importance of this integrated approach. Ecohydrology adopts an interdisciplinary approach to investigating interlinkages between the structure and function of ecological systems and the partitioning, flux, and storage of freshwater (Guswa et al., 2020). Furthermore, the emerging climatic consequences of global warming, changes in precipitation patterns and vegetation structure have further directed research attention to plant water use strategies and eco-hydrological interactions between plants and ecosystem water soil (Brodribb et al., 2020; Guswa et al., 2020).

The results of ecohydrological research have contributed to better managing and preserving fragile ecosystems (Bonacci et al., 2009;).

The observation and measurement of ecohydrological processes have seen important advances in new ideas, methodologies, and techniques.

Many state-of-the-art observation techniques, such as stable isotopes, wireless sensor networks, cosmic ray probes, and multi-source remote sensing, are continuously being introduced and widely applied. In a 2019 study by Lazo et al. 2019, a combination of techniques, including gravimetric measurements, cosmic ray soil moisture observations, soil moisture measurements, flow recession analyses, water balance-based and tracer-based techniques (e.g., stable isotopes) were effective for providing valuable information on water storage in reservoirs.

Stable isotopes of water are ideal tracers for hydrological analyses because they are intrinsic to water molecules and can be traced throughout the water cycle. Over the past two decades, isotope measurements have been increasingly used to derive water transit times in hydrological systems ranging on scales from catchments, lysimeters, or soil profiles, as recently reviewed by Sprenger et al. (2019b). In the past few decades, tracers have been widely applied in hydrological studies because they provide more detail about some underlying processes that control the chemical and physical behavior of elements and compounds in the natural environment. Naturally occurring tracers are more effective and environmentally accepted than artificially introduced tracers, making them applicable to a wide range of

geochemical problems (Gibson et al., 2005). Tracer methods mainly include isotope, geochemical, and dye tracers. Isotopic tracing techniques are crucial in hydrological studies. They were introduced into catchment hydrology research in the 1960s as supplementary tools to traditional hydrologic methods. These techniques aid in identifying the direction of water flow during rainfall, the paths it takes to reach the stream, and the period of its presence in the catchment area (McDonnell, 2003).

Stable isotope tracers are primarily oxygen-18 (^{18}O) and deuterium (^2H or D). Hydrogen and oxygen isotopes and mixing models are commonly utilized to differentiate stormflow into its pre-event and event components (Inamdar, 2011). However, analyzing the stable isotope compositions ($\delta^{18}\text{O}$ and $\delta^2\text{H}$) of xylem water and their potential sources has been shown to determine the water sources for plants effectively (Zhao et al., 2022).

A valuable tool for untangling water flows and limiting flow paths in complex landscapes is the application of isotope tracers. Stable isotopes in water are conservative tracers and provide valuable information about the water cycle at various spatiotemporal scales (Kendall & McDonnell, 1998). The isotopic composition of water connects the plant's water to its purported water sources, such as groundwater, rainfall, stream water, or soil water (mobile or tightly bound) (Mennekes et al., 2021). In recent years, they have been increasingly applied to understand the distribution of water at the soil-plant-atmosphere interface, in particular, the effects of seasonality and different types of soil and vegetation (Kuhlemann et al., 2021).

The association between observation, use of tracers, and simulation tools will increase the knowledge of forest ecosystem biogeochemistry and thus improve decision support for their sustainable management (Valentin, 2018).

In our study, the general objective was to investigate the effects of land use on soil water dynamics in an environment subject to climatic seasonality. The main research question is: How do the combined information on soil moisture and stable isotopes provide insights into the description of hydrological fluxes locally?

3.2 Materials and Methods

3.2.1 Site description and field campaign

The Alento River Catchment (ARC) is located in the southern Apennines (Province of Salerno, Campania Region, Italy) (Figure 3-1). Its drainage area is approximately a total drainage area of about 409 km², a perimeter of about 141 km, and an average altitude of approximately 400 m above sea level. Part of this basin belongs to the Cilento, Vallo di Diano, and Alburni National Parks. The main barrage is the Piano della Rocca (PDR) earthen dam that has been operating since 1995 and can be viewed as a hinge that not only physically connects the two parts of ARC, namely the Upper ARC (UARC; 101 km² drainage area) and Lower ARC (LARC; 308 km² drainage area) see Figure 3-1. The "Piano della Rocca" is 43.80 m high and has a maximum historical capacity of 28.5 m³. The artificial lake, subject to the regulation of the flow regime, is about 212 hectares at the peak water level and about 45 hectares at the minimum level. The upper Alento basin, together with the study areas of Picassent (Spain) and Thessaly Basin (Greece), has recently been considered as a hydrological observatory of the TERENO network ("Terrestrial environmental observatories") in the Mediterranean region (Nasta et al., 2017).



Figure 3-1 Geographic location of the Upper (UARC, green polygon) and Lower (LARC, red polygon) Alento river catchment in southern Italy.

The territory of the Alento River basin is almost totally mountainous-hilly, and the only flat areas are represented by the coastal strip and the valley floor of the river and its tributaries. The highest peaks are located at the eastern end of the basin and are represented by Monte Sacro (1705 m), Monte Scuro (1610 m), and Monte Falascoso (1494 m). The Alento river basin is set on terrigenous geological formations from the pre (Cretaceous) to synorogenic (Upper Miocene) series, commonly called Cilento flysch, formed by clayey and arenaceous rocks, with medium-low hydraulic permeability (Jones, 1985; De Vita et al., 2018). In the area of the basin, limestones also emerge in the northern end of the basin itself and the alluvial deposits of the valley floor of the Alento River. In the coastal area where the river mouth is located, there are finally sandy beach deposits, which are also permeable due to porosity. Furthermore, the basin is very homogeneous from the hydrogeological point of view; 80% consists of the arenaceous-marly-clayey complex, scarcely permeable; 15%, which mainly includes the Piana Alento and the coastal area, consists of the sandy-silty-gravelly complex, with decidedly higher permeability and 5% consists of a small limestone part located in the northern part of the basin. The water courses that flow on the arenaceous-marly-clayey complex are characterized by a torrential type regime, especially if their catchment area insists on poorly permeable soils named "flyschoids"; in fact, they are often characterized by the absence of outflows in the summer months (De Vita, 2001). In the sandy-silty-gravelly complex, on the other hand, the rivers flow on very permeable soils due to fracturing and karst phenomena; water circulation mainly affects the basal part of the aquifers. The presence of discontinuities and karst ducts induces intense infiltration phenomena that result in a prevalent underground runoff compared to surface runoff.

In UARC, the mean annual temperature is around 15.3 °C, and the mean annual precipitation is 1229.3 mm. In LARC, the mean annual temperature is around 16.4 °C, and the mean annual rainfall is 1067.1 mm. This information was referred to the period from 2016 to 2022. The Alento River catchment is now recognized as a Hydrological Observatory (ARC-HO) that belongs to the TERENO (TERrestrial Environmental Observatories) network. This is a long-term European ecosystem infrastructure network (Romano et al., 2018).

In UARC, two sub-catchments, MFC2 and GOR1, were chosen for experimental research. Two observed locations were set up, which represented varying hydrogeological, pedological, and topographic conditions and land uses (Figure 3-2).

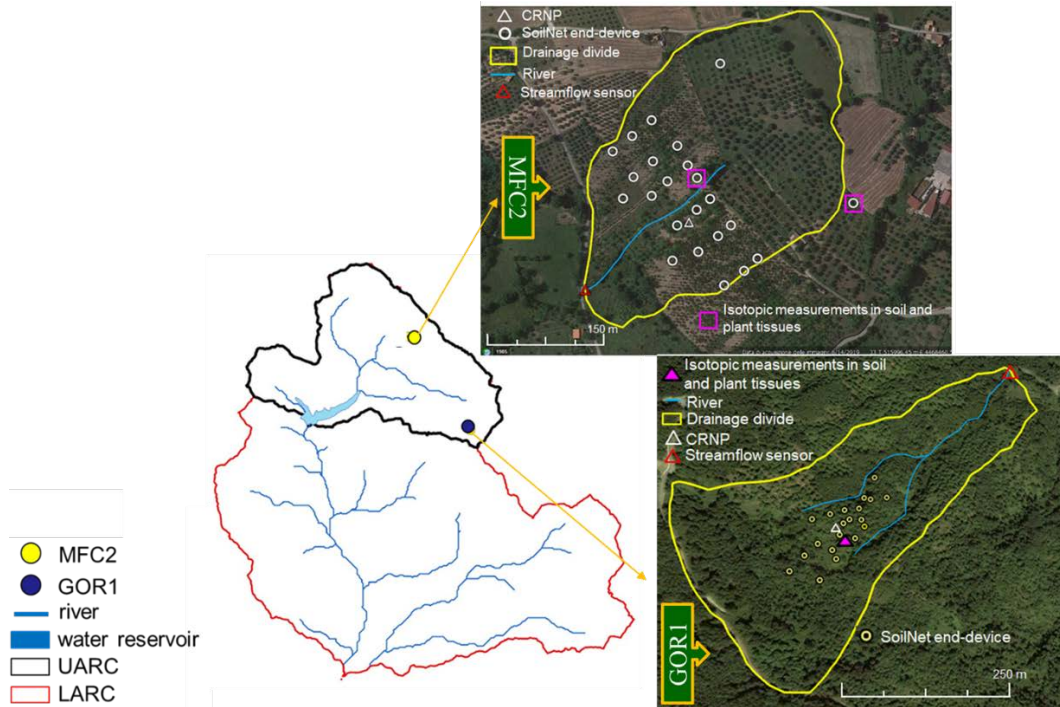


Figure 3-2 Geographical location and 5-m Digital Elevation Model (DEM) of the Upper Alento River Catchment (UARC) in Campania (southern Italy). Also shown are the two experimental sites (MFC2 and GOR1) with the relevant weather stations. The Piano della Rocca earthen dam delimits the artificial water reservoir. The satellite images display the positions of the twenty end-devices of the SoilNet wireless network and cosmic-ray neutron probe at MFC2 and GOR1. The triangle depicts the position of the soil profile subject to isotopic measurements.

MFC2 is close to the village of Monteforte Cilento, on the south-facing hillslope of UARC. It covers an area of around 8 hectares and represents the cropland zone of UARC. Here, you can find a mix of sparse horticultural crops and olive, walnut, and cherry trees. On the other hand, GOR1 is located near the village of Gorga, on the north-facing hillslope of UARC. It has a drainage area of roughly 23 hectares and represents the woodland zone of UARC. This area is characterized by dense chestnut, oak trees, and brushwood made of ferns and brambles.

The MFC2 sub-basin is set on a regolith (matrix of silt and clay and a subordinate fraction of sand and gravel) over a clayey turbiditic bedrock with relatively low permeability. Auger hole and slug infiltration tests were performed in MFC2 to

characterize the quiet permeability regolith zone. An outflow measurement station equipped with an ultrasonic sensor was installed at the outlet of MFC2 to keep track of the flow rate of an ephemeral stream.

The GOR1 sub-basin has a bedrock consisting of turbiditic sandstones with medium permeability and is mantled by a regolith zone characterized by mixtures of sand and silt.

The flow at GOR1 is temporary and drains an area of around 37.9 ha. A water height pressure transducer is placed close to the exit of a lengthy circular culvert (UTM WGS84 33T, 519832 m E, 4462834 m N) to monitor the discharge continually. The trench has recently been modified to measure low flow rates accurately.

The following is a comprehensive list of everything being monitored and the methods used in the experimental sub-basins to provide a complete description of the basin and a full report. In 2016, the MFC2 and GOR1 sub-catchments were equipped as follows:

An automatic weather station is located near MFC2, at 400 m a.s.l., and another is near GOR1, at 711 m a.s.l. A streamflow gauging station is also located at the outlet of each sub-catchment (a water level sensor at GOR1 and an ultrasonic sensor at MFC2).

A wireless sensor network (SoilNet; Forschungszentrum Jülich, Germany), comprising twenty end-devices connected to sensors positioned at 0.15 m and 0.30 m soil depths. At each soil depth, the apparent soil dielectric permittivity (which is used to estimate the volumetric soil-water content, θ , through an in-situ based calibration relation), soil temperature, and soil electrical conductivity are measured by the GS3 capacitance sensors, whereas the soil matric pressure potential, ψ , is determined by the MPS-6 sensor (the GS3 and MPS-6 probes are both manufactured by METER Group, Inc., Pullman, WA, USA).

A stationary cosmic-ray neutron probe (CRS2000/B by Hydroinnova LLC, Albuquerque, USA) is positioned approximately at the center of the SoilNet network. The CRNP is most sensitive to soil moisture in the upper soil horizon, and this sensitivity decreases exponentially to a penetration depth of about 0.3–0.8 m, depending on the soil moisture content. The CRNP is most sensitive to soil moisture

in the upper soil horizon, and this sensitivity decreases exponentially to a penetration depth of about 0.3-0.8 m, depending on the soil moisture content.

Twenty piezometers (consisting of PVC pipes) were also placed in this study area at depths from 6.0 m to 8.0 m below the land surface. In contrast, one piezometer was positioned at a depth of approximately 20 m. The monitoring wells are all equipped with sensors to measure the local depth to the water table. Apart from the classic chemical analyses, the water pumped from some piezometers is also used for stable isotope measurements.

In October 2020, we started fortnightly measurements of stable hydrogen and oxygen isotopes ($\delta^2\text{H}$ and $\delta^{18}\text{O}$) of water from a shallow aquifer, streamflow, and precipitation, but also extracted from soils and plant leaves in a representative soil profile in each experimental site (pink triangles in Figure 3-2).

Soil and vegetation samples were taken over the experimental soil profile (pink triangle in Figure 3-2). Cryogenic vacuum distillation has been used for water extraction. Vegetation (twig) samples were obtained from one oak tree and olive tree in MFC2 and one chestnut tree in GOR1. After cutting the twigs from the trees, we removed all the leaves and other green tissues close to the leaves, as well as the bark.

We sampled the twigs and not the leaves to avoid the effect of fractionation on xylem water (Benettin et al., 2018). Soil samples were taken from three different soil depths (15 cm, 30 cm, and approximately 100 cm) by using an Eijkelkamp manual auger (<https://en.eijkelkamp.com/products/>). Vegetation samples and soil samples for the extraction of xylem water and soil water were properly collected in 12-ml air-tight exetainer glass vials (Labco, Lampeter, U.K.). The extraction of soil and xylem water was carried out by using the cryogenic vacuum distillation (CVD) method (Koeniger et al., 2011) performed at the C.I.R.Ce. Laboratory of the “Luigi Vanvitelli” University of Campania.

3.2.2 Hydroclimatic monitoring

Since April 2016, an automatic weather station has been in operation at both experimental sites. It records rainfall using an aerodynamic rain gauge at 1-minute intervals, air temperature (T), relative humidity (RH), wind speed and direction,

and solar radiation using a four-component net radiometer at 15-minute intervals. The reference evapotranspiration (ET₀) (mm d⁻¹) is computed with the Penman–Monteith equation described by Allen et al. (1998).

3.2.3 Stable water isotopic monitoring

The monitoring of water isotopes commenced on October 19, 2020. Every 15 days, water samples were collected from MFC2 and GOR1 sites, including rainwater, groundwater, outlet, soil, and plant samples.

The water was extracted from soil and twig samples. We installed a Palmex rain collector near the weather stations on both sites. Rainfall water enters a 3 L plastic bottle through a funnel connected to a plastic siphon tube. The groundwater was sampled only at MFC2 in 2 piezometers and one stone-case well. At MFC2, we collected undisturbed soil samples at three depths (15, 30, and 100 cm) near a downy oak and an olive tree. The isotopic campaigns we started in October 2021 at the Olive Tree. In addition to the two plants, where we took the soil, we sampled another plant (a willow) that lay very close to a temporary channel that flows inside the basin and cuts it in half. At GOR1, we sampled the soil at three depths (15, 30, and 100 cm) near a chestnut tree and the tree near the same point.

3.2.3.1 Rain groundwater and surface water sampling for $\delta^2\text{H}$ and $\delta^{18}\text{O}$ analysis

Before sampling, all the information necessary to ensure the traceability of the sample taken was reported in the field register:

- Date and time of sampling;
- Detection of the coordinates of the sampling point;
- Photo of the sampling point;
- Depth of the filtering zone of the well or piezometer;
- Pumping system;
- Weather conditions.

The sampling described above was conducted using the following materials:

- Phreatimeter;
- Submersible pump with adequate head or bailer;
- 30-50 mL plastic bottles with cap and under cap;

- Syringe-to-syringe 0.45 μm filters;
- Labels;
- Indelible and water-resistant markers;
- Auger;
- Vials;
- Tube or paddle to fill the vials;
- Tree pruner;
- Cutter;
- 12-mL air-tight Labco Exetainer[®] vials.

Water sampling

When collecting rainwater samples, we poured water from the Palmex rain collector into the plastic bottle. To ensure the bottle was filled and air bubbles were avoided, we screwed the lid on tightly. These bottles had a capacity of 30-50 ml.

We used either a low-flow submersible pump or a bailer to gather groundwater samples. Before the use, we conditioned the bailer with the water that would be drawn. We then transferred the water sample into the plastic bottles. To prevent air bubbles from forming, we soaked the bottles three times with the water to be sampled and filled them carefully.

Streamflow water was collected from the creek by using a bucket, bailer, or bottle. The water sample was transferred into the plastic bottles. It is essential to rinse the bottles with water three times before filling them thoroughly to avoid the formation of air bubbles.

During sample collection, we refrained from filtering the samples on-site. However, we made sure not to collect suspended material. In cases where it was not avoidable due to turbid or organic-rich water, we filtered the sample in the laboratory using 0.45 μm syringe filters before proceeding with the analysis. The water samples were stored in the fridge before the isotopic analysis.

Soil sampling

We soil samples by using an auger at the depths listed above and divided them into three previously weighed vials. The vials were filled to slightly more than half the

length of the vial, leaving a headspace for the needle used for the extraction. If the sampling occurred in high air temperature conditions, the samples were kept in a field fridge until they were taken to the laboratory.

Plant sampling

To collect plants, we followed these four steps:

- Cut off the branch from the pilot plant;
- Removed the bark from the branch;
- Take from these three components (basal, central, apical);
- Close it in a previously weighed septic-capped Labco Exetainer® vials tube;

If the sampling takes place in conditions of high air temperature, it is advisable to keep the sample in the field fridge until it is taken to the laboratory, where, instead, it can remain in room T.

3.2.4 Extraction of water from the soil and the plant

3.2.4.1 Vacuum Extraction Line

The extraction of soil and branch water was carried out by cryogenic vacuum distillation at the CIRCE laboratory of the Department of Mathematics and Physics Campania University “Luigi Vanvitelli” (Italy). The cryogenic vacuum extraction system is made up of six extraction lines independently connected to a diaphragm vacuum pump (capable of reaching 70 Pa) by following the design proposed by Orłowski et al. (2013). The extraction line body is based on the use of Rilsan® flexible hoses, sphere valves (used for compressed air lines), and needles (Figure 3-3). A vacuum transducer (vacuometer) is used to monitor the vacuum of the line and check for the absence of significant leaks and the effectiveness of the utilized water traps.

In each line, a pair of two Labco Exetainer® vials (12 ml each) served as independent extraction and collection units independently connected by a thin stainless-steel tube (2.00 mm x 1.00 mm (ODxID)).

Before the beginning of the water extraction procedure, the collection vials are evacuated to a baseline vacuum pressure (measured by the vacuometer) to prevent atmospheric water contamination.

The extraction process is based on two distinct conceptual phases happening simultaneously:

- i. water evaporation from the sample in the Extraction Tube (ET) and
- ii. vapor condensation in the collection tube (CT).

The ET glass vials are placed into a thermoblock. Water evaporation is enhanced by heating the glass vials at a constant temperature of 90 °C. Evaporated water is forced to pass through the CT held at c.a. -180°C by Liquid Nitrogen (LN2) bath, partially submerged and dynamically kept under vacuum (i.e., 70 Pa) by keeping sphere valves (6, Figure 3-3) open during the whole extraction procedure. Typical extraction time is 120-180 minutes, depending on the sample typology. The extraction finishes when the entire amount of water is extracted from the soil or twig samples.

The vials are removed from the liquid nitrogen trap, defrosted at room temperature, wrapped tightly with Parafilm®, labeled, and stored in a refrigerator until further analyses.

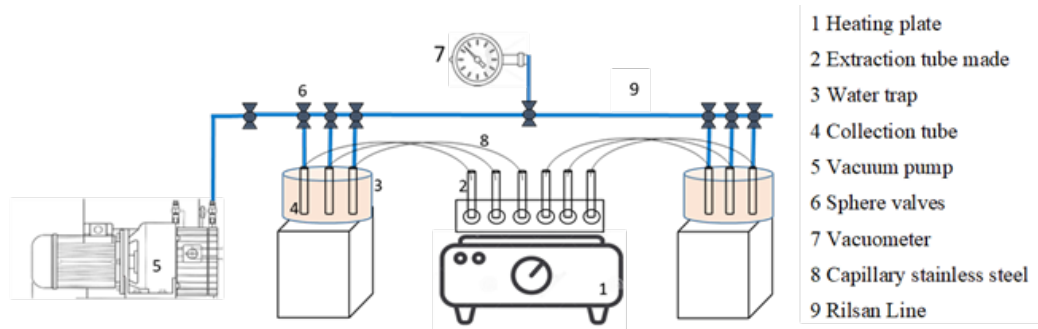


Figure 3-3 Schematic of the CVD realized and tested for soil water extraction

3.2.5 Sample $\delta^{18}\text{O}$ and $\delta^2\text{H}$ measurements

Extracted water samples have been measured by Isotope Ratio Mass Spectrometer (IRMS, Thermo Fisher Delta plus) in continuous flow (Thermo Fisher CONFLO IV) by means of Gas Bench II (GBII) and Flash HT in TC/EA configuration for $\delta^{18}\text{O}$ and $\delta^2\text{H}$, respectively.

For both kind of analyses four different labelled waters have been utilized namely OH26 ($\delta^{18}\text{O}=-11.20(0.01) \text{‰}$; $\delta^2\text{H}=-79.0(0.2) \text{‰}$), OH27 ($-24.89(0.02) \text{‰}$; $\delta^2\text{H}=-190.8(0.2) \text{‰}$), OH28($\delta^{18}\text{O}=-7.95(0.02) \text{‰}$; $\delta^2\text{H}=-49.0(0.3) \text{‰}$) and OH29 ($\delta^{18}\text{O}=-$

1.05(0.01) ‰; $\delta^2\text{H} = 1.8(0.2)$ ‰) belonging to the IAEA WICO 2020 exercise for absolute scale calibration purposes.

At the beginning of each analytical batch, a source optics tuning has been performed by working onto pure CO_2 and H_2 gasses with the aim to maximize *i*) beam transmission over the system and *ii*) attainable precision. Moreover, for the case of H_2 also H_3 Factor determination was performed. Continuous flow analyses were carried out by maintaining the integrated area of the sample and the reference peaks similar.

For each analytical batch QC samples (i.e. water) have been utilized and subjected to the analytical procedure described below for $\delta^{18}\text{O}$ and $\delta^2\text{H}$ to evaluate the overall batch quality.

For $\delta^{18}\text{O}$ analyses, 200 μL of samples (including the reference materials) were put in 20 mL vacutainers using volume calibrated pipettes, samples were flushed with He/CO_2 gas (.3% CO_2) mix @ 60 mL/min for 5 minutes, ensuring a complete environmental air removal. Equilibration between water and CO_2 was attained by letting the sample in static conditions (@25°C) for at least 20 hrs. Water equilibrated CO_2 was sampled and injected in the IRMS system by CONFLO IV (typical GB configuration was modified) in 10 replicate chromatographic pulses and bracketed within five pure CO_2 peaks (3+2) with the second being used as normalization for mass bias correction purposes.

For $\delta^2\text{H}$ samples, they have been analyzed by Flash HT in TC/EA configuration via CONFLO IV by Thermofisher Delta Plus IRMS. At the beginning of each analytical batch (c.a. 100 samples), H_3 factor determination was performed. An automated system allowing for reliable syringe sample introduction was utilized (Thermofisher AS 3000), sampling by a 5 ml syringe from a 2 ml vial containing the samples. Each sample (including the normalization reference samples) underwent to a total of 4 measurements, being the first utilized to avoid memory effects by injecting 2 H_2 gas pulses a series of 3 sample injections and two more H_2 pulses, and the last 3 performed by injecting 3+ 2 H_2 gas pulses (the second utilized for sample raw data normalization) bracketing 1 sample injection peak. Only the final three measurements have been utilized for measurement purposes.

Individually produced delta values in arbitrary ‰ units were acquired and analyzed offline for $\delta^{18}\text{O}$ and $\delta^2\text{H}$ respectively. In details for $\delta^{18}\text{O}$ for each of the ten replicates a statistical analysis was applied to verify the effectiveness of a linear relationship (i.e., linearity) of the produced isotope data vs m/z 44 signal: *i*) if a significant linearity was observed (i.e., significant slope with respect to 0) raw delta value and uncertainty were estimated at the same signal amplitude of the pure CO_2 peak utilized for sample raw data normalization; *ii*) if no linearity was found raw delta values were averaged and uncertainties estimated by standard error. For $\delta^2\text{H}$ instead, three replicate samples were averaged, and the standard error was utilized for uncertainty estimation purposes. Raw data produced for reference samples were used to make a calibration curve by means of an error weight fit procedure. This procedure takes into account for individual sample uncertainties or applies extra uncertainty accounting for sample adherence with the linear model necessary for normalization uncertainty estimation (Marzaioli et al., 2020).

3.2.6 Soil moisture monitoring

3.2.6.1 Calibration of field probes

The laboratory-based thermo-gravimetric method is the most accurate approach for determining the soil water content but is destructive, time-consuming, expensive, tedious, and labor-demanding (Topp and Ferré, 2002). To circumvent this drawback, indirect methods gained popularity by measuring variables, such as soil bulk dielectric properties, which are then empirically related to θ .

So, we carried out a calibration in-field procedure, confronting the volumetric water content (obtained from gravimetric water content in the soil) with the empirical equations.

In the first step, undisturbed soil cores were collected at depths of 15 and 30 cm (steel cylinder of 7.2 cm inner diameter and 7.0 cm height) for thermo-gravimetric measurements over five field campaigns during all year at MFC2 at GOR1 (4 October 2018, 15 November 2018, 29 March 2019, 17 May and 24 October 2019 December 2021).

The gravimetric water content (θ_g) was converted into volumetric water content (θ_v).

We used three empirical calibration equations: 1) factory (METER) calibration, 2) Topp's universal law, and 3) Ferre's equation to calculate θ_v from knowledge of soil permittivity. Then, we compared the gravimetric water content for all 20 sensor positions in both sites with the empirical relations.

3.2.7 Isotope Data Analysis

The relationship between the relative stable hydrogen and oxygen isotope ratios of water systems was identified by Craig (1961) as:

$$\delta^2H = 8 * \delta^{18}O + 10$$

Eq. (3-1)

who characterized this relationship as indicative of "waters which have not undergone excessive evapotranspiration" Rozanski et al. (1994) refined Craig's formula to express the global meteoric water line (GMWL) by replacing the regression coefficients 8 with 8.13 and 10 with 10.8.

We used the local meteoric water line (LMWL) for data visualization in dual isotope plots for two sites.

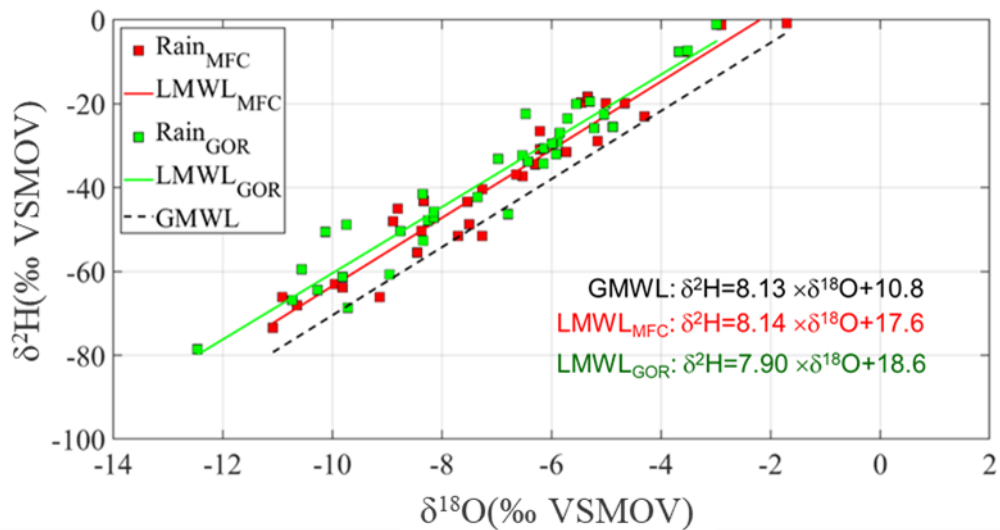


Figure 3-4 Local meteoric water line (LMWL) for two sites versus the global meteoric water line (GMWL). The red dots (MFC2) and green dots (GOR1) indicate the isotopic composition of the rainfall collected from October 2020 to October 2022.

For isotopic composition comparisons, we use line-conditioned excess (lc-excess) as described by Landwehr and Coplen, 2006 and defined as:

$$lc - excess = \frac{\delta^2H - \alpha * \delta^{18}O - b}{S}$$

Eq. (3-2)

where a and b represent the slope and intercept of the LMWL and S represents the standard deviation defined as:

$$S = \sqrt{SD_{\delta^2H}^2 + (\alpha * SD_{\delta^{18}O})^2}$$

Eq. (3-3)

This means that lc-excess is the vertical distance from the LMWL of a sample as measured by δ^2H deviation. Lc-excess of precipitation is 0 ‰ by definition, making it a preferable metric for assessing deviation from the meteoric water line (MWL) (Sprenger et al., 2017). Ecohydrological separation studies commonly employ a combination of dual-isotope plots and lc-excess, as waters can share similar lc-excess values but very different combinations of δ^2H and $\delta^{18}O$.

3.3 Results

3.3.1 Dynamics in hydroclimate and soil moisture

The hydro-climatic conditions during 2020-2022 were similar to the long-term average (2016-2022) and reported in Table 3-1 for two sites. Both sites show precipitation patterns that align with the meteorological regime of Mediterranean environments, with rainfall concentrated between October and March (see Figure 3-5(a)).

The general soil water content (SWC) trends (Figure 3-5(d)) followed the seasonal rainfall patterns at both sites. Soil moisture responded quickly to rainfall even at both sites and exhibited similar trends. Soil moisture at 15 cm depth is higher in wet periods, while at 30 cm depth, SWC is highest in dry months. At GOR1, SWC at 30 cm depth is higher throughout the year. GOR1 had ET₀ higher rates overall and more significant peaks during the dry season. These differences can be attributed to variations in land use and soil characteristics. At the MFC2 site, clayey soils and shallow groundwater might result in capillary rise, decreasing the estimated ET₀ for periods with high groundwater tables. At the GOR1 site, this situation can be neglected. Concerning soil temperature, the highest soil temperature time series is recorded at MFC2, which is located on the south-facing slope (Romano et al., 2018).

Table 3-1 The average precipitation (P), temperature (T), potential evapotranspiration potential (ET₀), and relative humidity (RH) for two experimental sites (at MFC2 and GOR1) over the period of 2016-2022.

	Rain Mm	T °C	ET ₀ Mm	RH -
MFC2	1154.68	14.86	574.69	0.64
GOR1	1259.00	13.23	554.36	0.70

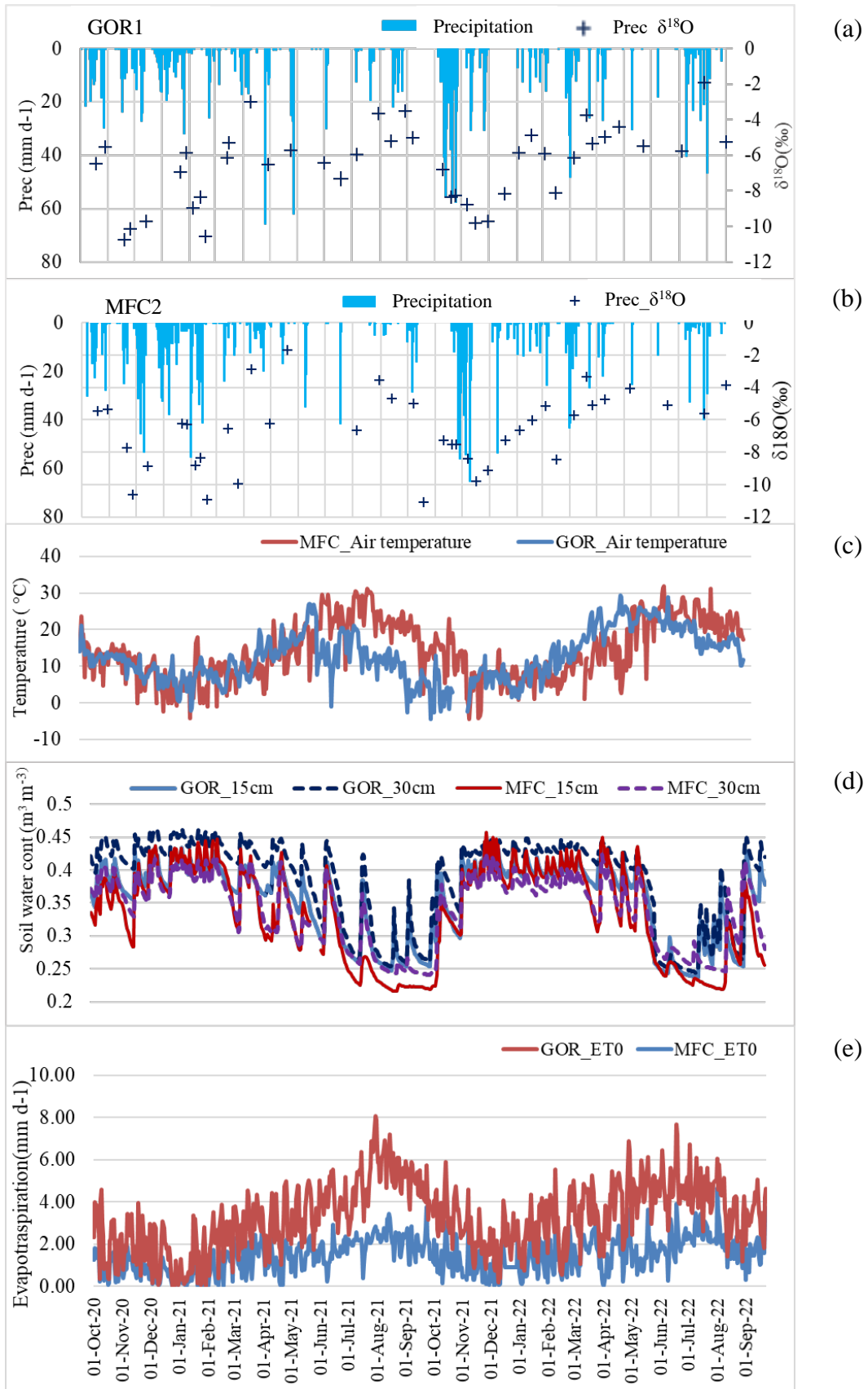


Figure 3-5 Daily values of a) rainfall and $\delta^{18}\text{O}$ in rainfall water at MFC2 (a), b) rainfall and $\delta^{18}\text{O}$ in rainfall water at GOR1 (c), daily air temperature at MFC2 (red line) and GOR1 (blue line) (d) daily volumetric water content measured by using the GS3 sensor at the depths of 15 cm and 30 cm at MFC2 and GOR1, (e) reference potential evapotranspiration(ET_0) at MFC2 and GOR1(interval 15 min) and $\delta^{18}\text{O}$

3.3.2 Dynamics of stable isotopes

3.3.2.1 Measurements of Isotopes in Precipitation, Streamflow, and Groundwater

Precipitation samples plot along the LMWL with no significant deviations, as shown in Figure 3-6. Moreover, the isotope ratios of precipitation showed the expected seasonality, with depletion during winter and enrichment during summer. The mean $\delta^{18}\text{O}$ and $\delta^2\text{H}$ values at MFC2 were -6.56 ($\text{SD}=2.32$) and -38.19 ($\text{SD}=19.26$), respectively. The mean $\delta^{18}\text{O}$ and $\delta^2\text{H}$ values at GOR1 were -6.76 ($\text{SD}=2.33$) and -37.93 ($\text{SD}=18.02$), respectively. Outlet and groundwater samples were tightly clustered on the local meteoric water line (LWML) with no significant seasonal variation (see Figure 3-6), similar to previous ecohydrologic separation studies (Bowling et al., 2017; Brooks et al., 2010; Oshun et al., 2016). The mean $\delta^{18}\text{O}$ and $\delta^2\text{H}$ values at MFC2 for streamflow water were -6.48 ($\text{SD} = 0.51$) and -35.49 ($\sigma = 4.90$), respectively, the mean $\delta^{18}\text{O}$ and $\delta^2\text{H}$ values at GOR1 for outlet water were -7.05 ($\text{SD}= 0.41$) and -33.68 ($\text{SD} = 3.26$), respectively. The mean $\delta^2\text{H}$ and $\delta^{18}\text{O}$ values at MFC2 for groundwater were -6.42 ($\text{SD} = 0.10$) and -34.08 ($\text{SD}= 6.57$), respectively.

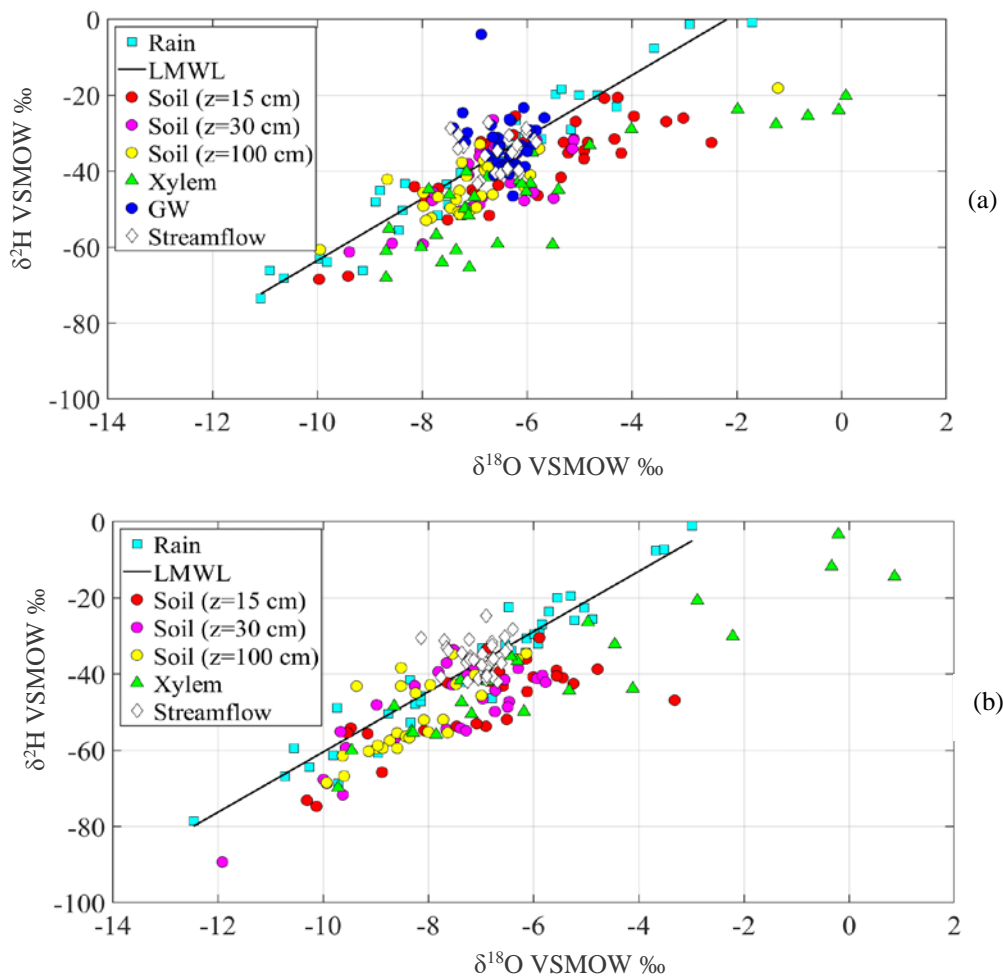


Figure 3-6 Dual-isotope plot for water samples of rain, streamflow, groundwater (GW) soil and plant in two experimental sites, MFC2(a) and GOR1(b)

3.3.2.2 Measurements of isotopes in the soil and xylem water

The $\delta^{18}\text{O}$ and $\delta^2\text{H}$ of soil water isotopic compositions in the soil of oak varied from -9.96‰ to 1.76‰ (MFC2, depths of 15–30 cm), from -9.95‰ to -1.21‰ (MFC2, soil depth of 100 cm), from -68.43‰ to -20.55‰ (MFC2, depths of 15–30 cm), from -60.65‰ to -18.05‰ (MFC2, soil depth of 100 cm), respectively.

The $\delta^{18}\text{O}$ and $\delta^2\text{H}$ of soil water isotopic compositions near the chestnut varied from -11.91‰ to -3.31‰ (GOR1, depths of 15–30 cm), from -9.93‰ to -4.93‰ (GOR1, depth of 100 cm), from -89.31‰ to -30.42‰ (GOR1, depths of 15–30 cm) from -68.47‰ to -34.57‰ (GOR1, depth of 100 cm), respectively.

The $\delta^{18}\text{O}$ and $\delta^2\text{H}$ of xylem water isotopic compositions varied -from -8.69‰ to 2.98‰ , from -68.00‰ to -20.10‰ (Oak at MFC2); from -11.09‰ to -5.51‰ ,

from -60.85 ‰ to -51.77‰ (Olive at MFC2) respectively.; from -8.49 ‰ to -0.44‰, from -62.39 ‰ to -11.46 ‰ (willow at MFC2), respectively. These values are presented in Table 3-2 and Table 3-3.

The analysis showed more stable water isotope variation in upper soil layers (15 and 30 cm depths). However, soil samples collected at 100 cm showed lower respect than those contained at 15 and 30 cm variability in both sites. The isotopic compositions of the deeper soil horizons are depleted and damped in their responses to precipitation inputs and evaporative effects compared to higher horizons. In general, soil water isotopic compositions were more variable in the upper horizons and became less inconsistent with depth at both locations. This phenomenon has also been observed in studies conducted by Song et al. (2009), McCutcheon et al. (2017), and Zhao et al. (2013). All soil layers at MFC2 had negative lc-excess, while at GOR1, all had positive or near-zero lc-excess. Furthermore, the d-excess of soil water at GOR1 increased with soil depth (see Figure 3-7).

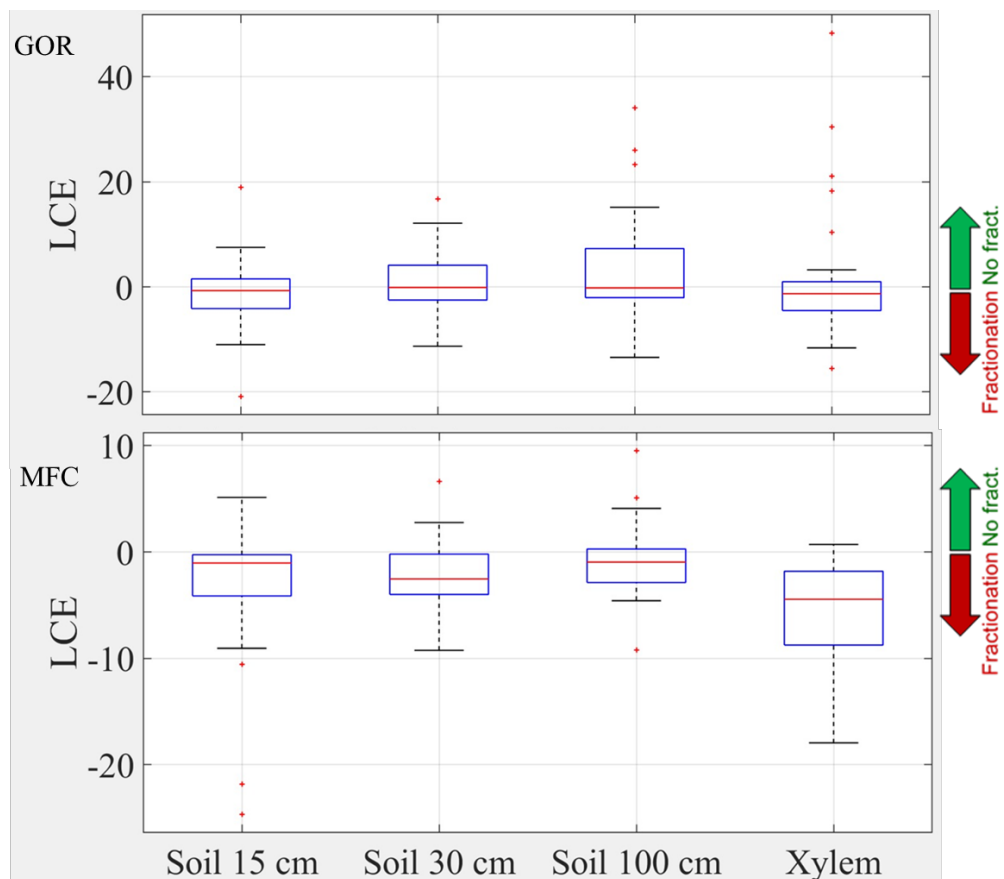


Figure 3-7: Boxplots of soil water and xylem water d-excess. Boxes represent the Lc-excess, while whiskers indicate the minimum and maximum values, excluding the outliers. The horizontal solid line within boxes represents the median.

Moreover, the soil at a depth of 15 cm at MFC2 showed considerable deviations from the LMWL. In the forest site (GOR1), the isotopic water compositions in the soils showed less variation compared to the MFC2 site.

Plant water isotopic evolution varied with species and sampling time. The xylem water isotopic compositions of oak, olive, and willow trees showed variations in their $\delta^{18}\text{O}$ and $\delta^2\text{H}$ values.

The $\delta^{18}\text{O}$ values for Oak trees varied between -8.69‰ and 2.98‰, while the $\delta^2\text{H}$ values ranged between -68.00‰ and -20.10‰. For Olive trees, the $\delta^{18}\text{O}$ values fell between -11.09‰ and -5.51‰, and the $\delta^2\text{H}$ values ranged from -60.85‰ to -51.77‰. Willow trees had $\delta^{18}\text{O}$ values ranging from -8.49‰ to -0.44‰ and $\delta^2\text{H}$ values ranging from -62.39‰ to -11.46‰. Chestnut trees had $\delta^{18}\text{O}$ values ranging from -9.71‰ to 0.87‰, and the $\delta^2\text{H}$ values ranged between -69.76‰ and -3.30‰. The xylem water samples along the LWML exhibit significant deviations for both sites, but the deviations are more pronounced in the samples from MFC2. In fact, at MFC2, some xylem samples fall very far from the LWML and are highly enriched. We noted that the enrichment was from winter to spring, as observed by numerous ecohydrological separation studies (McCutcheon et al., 2017; Oerter & Bowen, 2017). It is probable that having collected a plant sample that was not transpiring and without leaves, water was extracted, which was stagnant xylem and had partially evaporated. MFC2 and GOR1 plants have negative d-excess, with MFC2 being more negative. These results may be influenced by the winter enrichment found in xylem waters.

Similar winter plant water trends have been attributed to the evaporative enrichment of stagnant xylem water that remains after transpiration ceases (Bowling et al., 2017; McCutcheon et al., 2017; Oerter & Bowen, 2017). This phenomenon was not noticed for the olive tree, even though we started isotope monitoring at this point on October 19, 2021. The double isotope diagram shows that the samples of water extracted from the olive tree are positioned together with all the others without showing enrichment.

Table 3-2 Minimum, maximum, mean, median, and standard deviation values of isotopic signatures in the rain, groundwater, streamflow, plants, and soil sampling in each depth segment in MFC2

MFC2 ($\delta^{18}\text{O}$ VSMOW ‰)	Rain		Soil Oak			Soil Olive		
	-	15cm	30cm	100cm	15cm	30cm	100cm	
Samples	39	46	44	44	19	12	23	
Minimum	-11.08	-9.96	-9.39	-9.95	-10.05	-9.73	-8.98	
Maximum	-1.70	1.76	-2.28	-1.21	-0.36	-4.84	-5.53	
Media	-6.56	-5.16	-6.16	-6.81	-5.40	-7.59	-7.18	
Median	-6.30	-5.14	-6.57	-6.93	-5.91	-7.79	-7.22	
Standard deviation	2.32	2.21	1.46	1.28	2.70	1.68	0.94	
MFC2 ($\delta^{18}\text{O}$ VSMOW ‰)	Streamflow	Plant			Groundwater			
	-	Oak	Olive	Willow	P21	P22	P23	
Samples	27	43	18	34	39	9	12	
Minimum	-7.46	-8.69	-11.09	-8.49	-7.42	-6.63	-7.40	
Maximum	-5.82	2.98	-5.51	0.44	-5.92	-5.99	-5.67	
Mean	-6.48	-5.82	-7.39	-5.30	-6.43	-6.36	-6.56	
Mediana	-6.34	-6.56	-7.20	-6.32	-6.35	-6.34	-6.55	
Standard deviation	0.46	2.63	1.24	2.31	0.31	0.19	0.54	
MFC2 ($\delta^2\text{H}$ VSMOW ‰)	Rain		Soil Oak			Soil Olive		
	-	15cm	30cm	100cm	15cm	30cm	100cm	
Samples	34	34	31	31	9	10	12	
Minimum	-73.51	-68.43	-61.22	-60.65	-76.41	-68.79	-61.82	
Maximum	-0.80	-20.55	-26.39	-18.05	-42.75	-38.56	-44.52	
Mean	-38.19	-37.01	-42.05	-43.50	-53.95	-55.60	-52.04	
Median	-37.03	-34.59	-40.95	-45.06	-50.61	-56.12	-51.14	
Standard deviation	19.26	11.70	9.08	8.29	9.93	10.12	5.62	
MFC2 ($\delta^2\text{H}$ VSMOW ‰)	Streamflow	Plant			Groundwater			
	-	Oak	Olive	Willow	P21	P22	P23	
Samples	26	32	8	23	29	9	10	
Minimum	-43.23	-68.00	-60.85	-62.39	-46.49	-40.97	-35.53	
Maximum	-27.03	-20.10	-51.77	-11.46	-3.91	-26.27	-25.89	
Mean	-35.49	-45.90	-57.57	-41.12	-34.73	-36.23	-31.39	
Median	-34.71	-45.76	-58.60	-44.08	-35.83	-37.94	-31.55	
Standard deviation	4.91	13.39	3.03	14.41	7.77	4.87	3.43	

Table 3-3: Minimum, maximum, mean, median, and standard deviation values of isotopic signatures in the rain, groundwater, streamflow, plants, and soil sampling in each depth segment in GOR1

GOR1 ($\delta^{18}\text{O}$ VSMOW ‰)	Rain		Soil Chestnut			Plant	Outlet
	-	15cm	30cm	100cm	Chestnut	-	
Samples	44	40	39	40	32	46	
Minimum	-12,46	-10,31	-11,91	-9,93	-9,71	-8,14	
Maximum	-1,91	-3,31	-4,88	-4,93	0,87	-5,97	
Mean	-6,76	-6,47	-7,30	-8,03	-5,92	-6,99	
Median	-6,14	-6,13	-7,11	-8,16	-6,68	-6,91	
Standard deviation	2,33	1,74	1,54	1,13	2,86	0,40	

GOR1 ($\delta^2\text{H}$ VSMOW ‰)	Rain		Soil Chestnut			Plant	Outlet
	-	15cm	30cm	100cm	Chestnut	-	
Samples	39	31	30	29	24	38	
Minimum	-78,57	-74,70	-89,31	-68,47	-69,76	-83,75	
Maximum	-1,05	-30,42	-33,59	-34,57	-3,30	-24,62	
Mean	-37,93	-46,75	-49,56	-51,54	-40,31	-37,31	
Median	-34,28	-43,12	-46,84	-55,15	-42,82	-36,30	
Standard deviation	18,02	10,85	12,28	9,91	16,97	8,82	

3.3.2.2.1 Seasonal variability

The isotope signal in the groundwater was consistent at both locations throughout the year. The stable isotopes of water (P21, P22, P23) at MFC2 showed limited variation. We sampled several wells, and the isotopic signal was constant in all of them.

During the first sampling period (October 2020 to February 2021), the soil water, plants, and rainfall showed depleted isotope signals, probably due to seasonal variations in precipitation patterns. However, during the spring and summer at MFC2, we observed enriched isotope ratios of deuterium and oxygen in the soil, particularly in the surface soil (15-30 cm). In contrast, the surface soil is depleted in winter and fall, and the deep earth (100 cm) remains consistent all year with low variability (Figure 3-8). At GOR1, we observed similar phenomena but with slight variations in seasonality.

In contrast, olive shows a non-seasonal isotopic signal with slight variation throughout the year.

A winter enrichment of the isotope composition was observed in oak, willow, and chestnut plants during winter, as observed by numerous ecohydrologic separation

studies (McCutcheon et al., 2017; Oerter & Bowen, 2017). Similar winter plant water trends have been attributed to the evaporative enrichment of stagnant xylem. Some xylem samples fall very far from the LWML and are highly enriched, but most are branch samples collected in winter when transpiration was null. It is probable that having collected a plant sample that was not transpiring and without leaves, water was extracted, which was in the selection and had partially evaporated.

This phenomenon was not noticed for the olive tree, even though we started isotope monitoring at this point on October 19, 2021 (Figure 3-9). In fact, in the dual isotope plot, it is observed that the samples of water extracted from the olive tree are positioned together with all the others without showing enrichment.

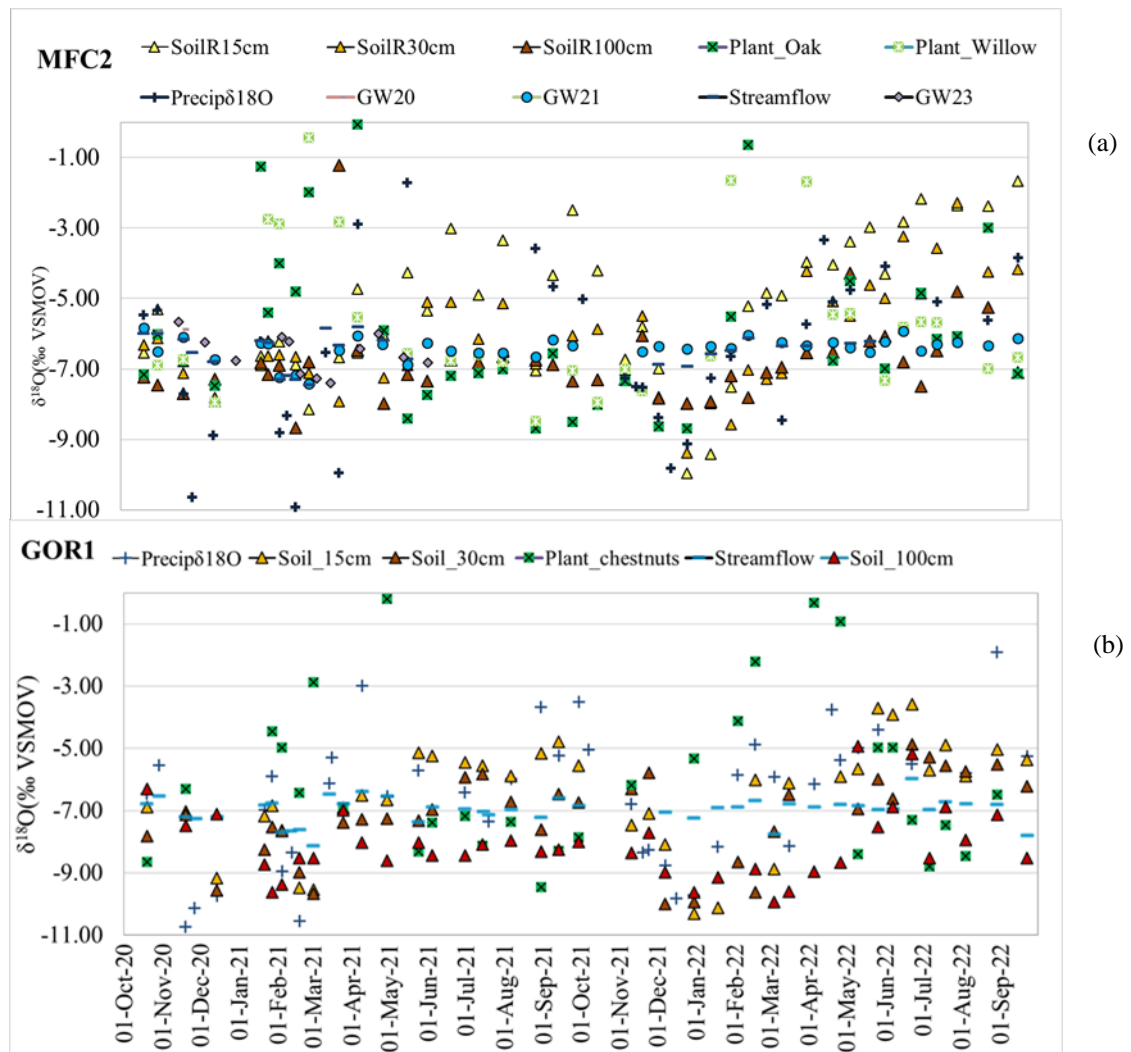


Figure 3-8 Seasonal sample of the isotopic ratio for water samples of rain, streamflow, groundwater (GW) soil and plant in two experimental sites, MFC2(a) and GOR1(b)

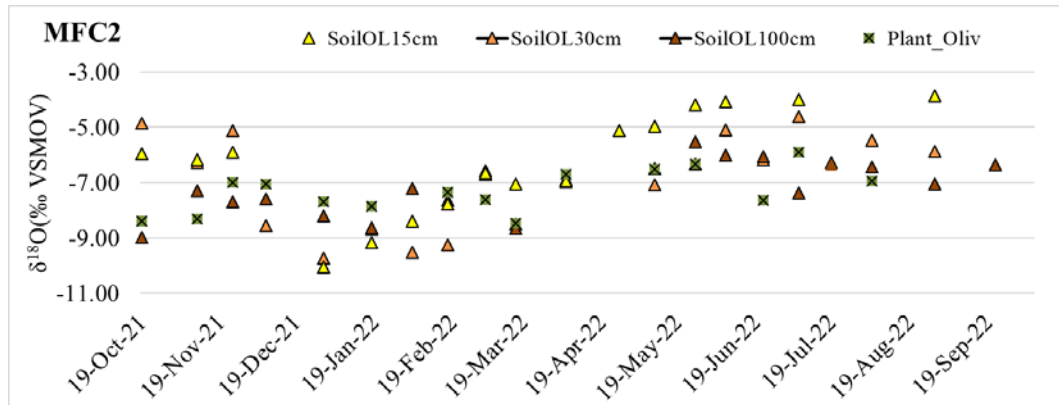


Figure 3-9 Seasonal sample of the isotopic ratio for water samples soil and plant in MFC2 (olive monitoring point)

3.3.2.3 Isotopes and soil moisture

The correlation between soil water content and isotope signal exhibits a seasonal pattern. Between April and September, when the soil's water content is around the wilting point, the soil's isotopic signal is enriched (see Figure 3-10 and Figure 3-11). Conversely, the soil's isotopic signal is depleted from October to March when the water content is at field capacity. The wilting point and field capacity references refer to the work of Nasta et al., 2020. At MFC2, the enrichment of water in the soil in the period between April and September is more marked as the water content decreases; the isotopic signal is enriched, probably due to the high evaporation of the soil. The SWC data shows rapid drainage at 15 cm sensors and high soil temperatures, supporting this interpretation. However, at GOR1, the dominant flux is transpiration. In fact, in Gorga, the enrichment of the isotopic signal is observed in the summer months, but it stops in a range of values without progressive enrichments.

The explanation could be given by the fact that it could be that at MFC2, evaporation is more significant than transpiration, assuming that there is no fractionation in the plant (Barbeta et al., 2020).

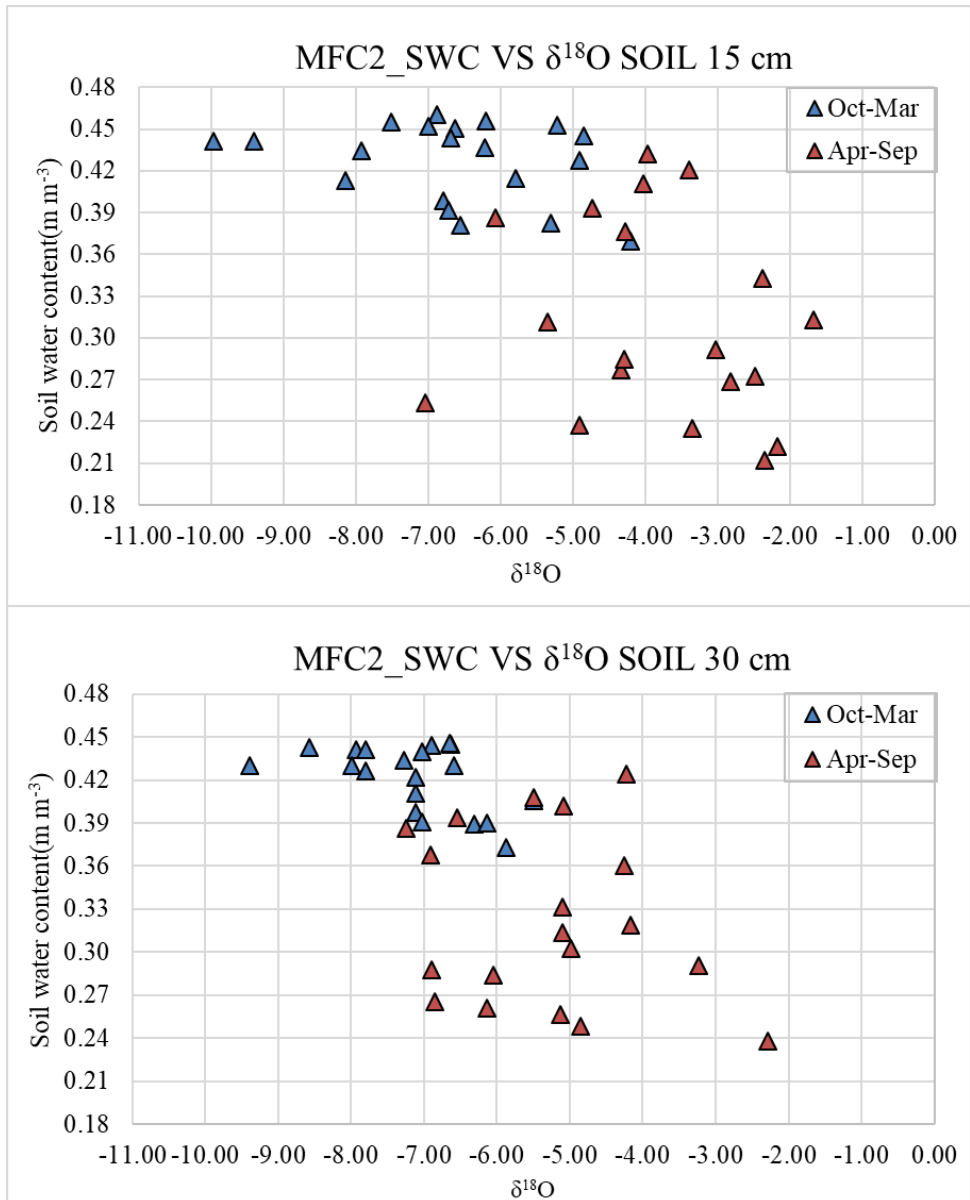


Figure 3-10: The daily soil water content versus the measurement of $\delta^{18}\text{O}$ in soil water. The blue triangles represent the relationship between water content and $\delta^{18}\text{O}$ on sampling days from October to March, while the red ones represent the relationship between water content and $\delta^{18}\text{O}$ on sampling days from April to September. The plot (a) relates to the samples collected at 15 cm depth, while plot (b) relates to those collected at 30 cm depth. The data is related to the MFC2 site.

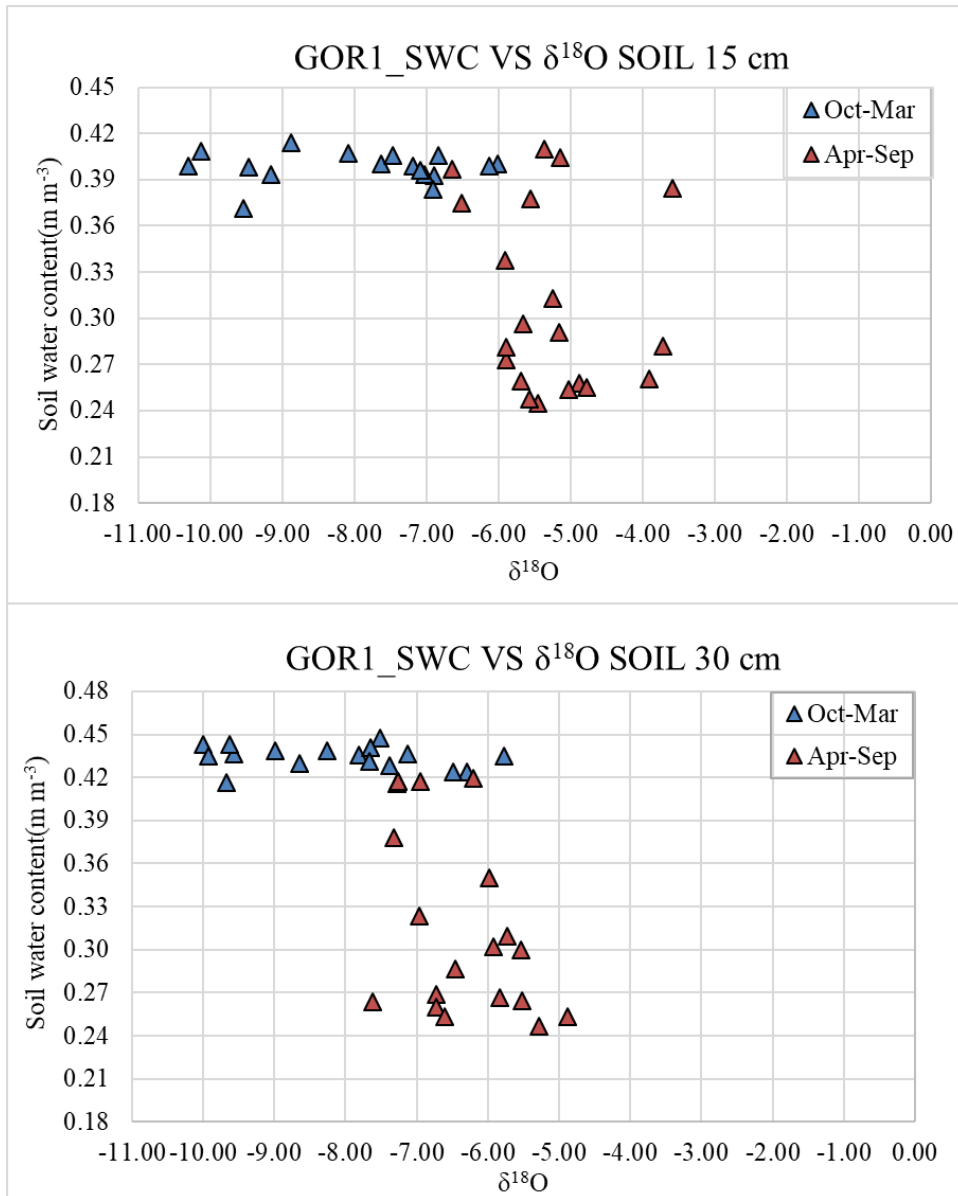


Figure 3-11: The daily soil water content versus the measurement of $\delta^{18}\text{O}$ in soil water. The blue triangles represent the relationship between water content and $\delta^{18}\text{O}$ on sampling days from October to March, while the red ones represent the relationship between water content and $\delta^{18}\text{O}$ on sampling days from April to September. The plot (a) relates to the samples collected at 15 cm depth, while plot (b) relates to those collected at 30 cm depth. The data is related to the GOR1 site.

3.4 Discussion

In this study, we sampled stable water isotopes every two weeks for two years, from October 2020 to October 2022, in two different soil types and land uses in a Mediterranean agroforestry environment. Other studies have focused on monthly samplings during an entire growing period in different land use types in the North German lowlands (Landgraf et al., 2022). Information from this sampling should be interpreted with other variables monitored in the experimental basins used for this study, such as soil physical properties, soil moisture monitoring, and soil hydraulic properties. In the results section, we have seen the different soil moisture dynamics in the two experimental sites regarding the isotopes present in the soil and the information regarding the eco-hydrological separation that can be provided by isotope monitoring. At GOR1, peak moisture recessions at lower water contents are faster than at MFC2. This partly reflects land use influences on ecohydrological distribution (e.g., increased evaporation in MFC2) and soil properties. Forest soils have a lower water retention capacity than MFC2 clayey soils, which have a higher water retention capacity. Several studies by Smith, Tetzlaff, and Kleine have demonstrated the dependence between soil moisture dynamics, soil properties, and land use (Kleine et al. (2020b) and Kleine et al. (2020)). We did not monitor soil moisture at 100 cm, but soil isotope measurements at a depth of 100 cm demonstrated that deep soil layers have less dynamic soil moisture at both MFC2 and GOR1.

In long-term studies, soil water isotope monitoring, together with the other variables monitored in this basin, has a vital potential to show how water distribution changes over the seasons and under non-stationary climatic conditions. In particular, the effects of evaporation on fractionation change as vegetation develops according to new land uses. Land use, whether agricultural or forestry, significantly affects the eco-hydrological distribution of these basins. It was observed that the forest areas (GOR1) had more stable water isotopic signals in the soil and showed less variability than the MFC2 site with clayey soils and crops. This suggests that forests have a more consistent eco-hydrological pattern. Agriculture, with its different soil characteristics and land management practices, has led to variations in soil moisture and isotopic signals. This could result in higher evaporation rates, resulting in an

impact on soil water content. Regarding identifying the dominant processes, we can state that the forest areas typically showed higher transpiration rates, even if it is inferred information and not directly measured, which leads to a more coherent and stable isotopic signal in soil and water.

Agricultural areas may experience higher evaporation rates and soil moisture variability, affecting the eco-hydrological distribution.

Stable isotopes of soil water have provided information through water source tracing by helping to identify sources of water in the soil, whether from rainfall, groundwater, or other sources, understanding how water moves, revealing its signature along the soil profile Sprenger et al. (2017); the assessment of water availability by indicating availability at different depths and how it varies according to land use. In long-term studies, soil water isotope monitoring, together with the other variables monitored in this basin, has a vital potential to show how water distribution changes over the seasons and under non-stationary climatic conditions. In particular, the effects of evaporation on fractionation change as vegetation develops according to new land uses. Land use will also change how rainfall mixes with resident soil water as soil structure changes and root zones expand. Such monitoring would usually not be feasible as part of routine monitoring. However, repeating this after a few years and using the data to calibrate a model may be worth it.

4 Coupling isotope tracing and eco-hydrological modeling to quantify root water uptake transit time²

4.1 Introduction

Understanding how plants uptake soil water originating from individual irrigation events is key to agricultural water sustainability. However, quantifying plant water use, stress, and resilience represents a major scientific challenge for improving the design of appropriate irrigation-based water management strategies (Jackisch et al., 2020). A key factor is the transit time of irrigation water from when it enters through the soil surface to its exit as root water uptake (RWU). This transit time is a key metric to describe the temporal origin of RWU (von Freyberg et al., 2020). Stable isotopes of hydrogen (²H) and oxygen (¹⁸O) represent valuable tools to estimate transit time and source water mixtures in the soil-plant-atmosphere continuum (SPAC) (e.g., Stumpp et al., 2012; Benettin et al., 2015; Penna et al., 2018; Beyer and Penna, 2021), especially in agricultural systems (e.g., Beyer et al., 2018; Barbeta et al., 2020; Penna et al., 2020; Penna et al., 2021; Mennekes et al., 2021; Kahmen et al., 2021; Chen et al., 2022; Aguzzoni et al., 2022).

Recently, the temporal origin of RWU has been determined by tracking water parcels introduced with individual labelled rainfall or irrigation events into the soil profile (Sprenger et al., 2016; Asadollahi et al., 2022). These studies have used virtual tracer injection experiments to assess root water uptake dynamics under different environmental conditions. Nevertheless, interpreting RWU dynamics and understanding the temporal origin of RWU by exploiting process-oriented hydrological models is still needed. Here we built on an isotope labelling approach in a potted olive tree experiment performed by Amin et al. (2021) as the basis of our model approach. We present a proof-of-concept modelling analysis that combines isotope tracing and the water flow in Hydrus-1D to explore the temporal origin of RWU. Our specific objectives are: *i*) to simulate water flow and isotope

² Nasta, P., D. Todini-Zicavo, G. Zuecco, C. Marchina, D. Penna, J.J. McDonnell, A. Amin, C. Allocca, F. Marzaioli, L. Stellato, M. Borga, N. Romano. 2023. Quantifying irrigation uptake in olive trees: a proof of concept approach combining isotope tracing and Hydrus-1D. *Hydrological Sciences Journal* 68:10, 1479-1486 DOI: 10.1080/02626667.2023.2218552

transport in the potted olive tree system by optimizing the soil hydraulic parameters via inverse modeling; *ii*) to simulate the RWU transit times and the contribution of irrigation water to actual transpiration by using a virtual tracer experiment based on an ensemble simulation approach.

4.2 Materials and Methods

4.2.1 Experimental setup, monitoring, and sampling approach

Two 6-year-old olive trees (*Olea europaea*; 0.06 m diameter and 1.9 m height) were placed in a glasshouse at the Dept. of Land, Environment, Agriculture and Forestry of the University of Padova (Italy). The two olive trees (named O1 and O2) were positioned in 70-L draining plastic pots (height of 42.0 cm) containing a soil mixture of 80% sandy loam and 20% pumice repacked at the oven-dry soil bulk density of 1.45 g cm^{-3} with a corresponding soil porosity of $0.45 \text{ cm}^3 \text{ cm}^{-3}$ (Amin et al., 2021). The soil in each pot was covered with plastic film to limit the evaporation losses from the soil surface (Figure 4-1). The experiment lasted seven weeks, from May 16, 2018 to July 6, 2018 for a total of 52 days (corresponding to 1234 hours considering the initial time on May 16 at midnight and the final time on July 6 at 9:00 a.m.).

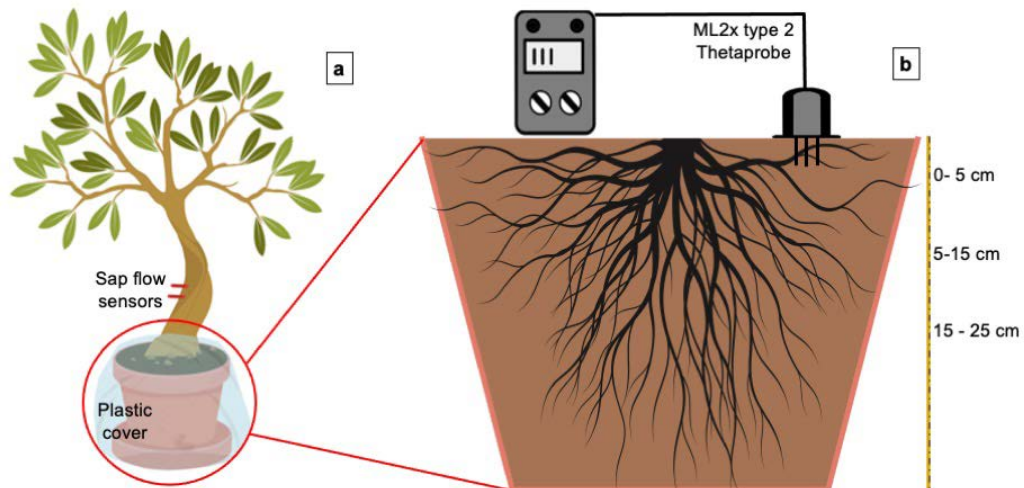


Figure 4-1 a) Sap flow sensors were installed in the trunk of the olive tree (*Olea Europaea*) and placed in a 70 L pot covered by a plastic film; b) cross-section of the soil profile in the pot with the positions of the ThetaProbe shown on the soil surface and the three soil sampling depths (0-5 cm, 5-15 cm, and 15-25 cm) for isotope measurements.

Air temperature, relative air humidity, and global solar radiation were measured at 5-minute intervals by a weather station installed inside the glasshouse, at a 1 metre distance from the two olive trees. Daily values of reference evapotranspiration (ET_0) were calculated using the standard physically-based Penman-Monteith equation (Allen et al., 1998). Crop-specific potential evapotranspiration (ET_c) under standard conditions without water limitations (the pot was frequently irrigated during the experiment) was calculated by multiplying ET_0 by the specific crop coefficient, K_c (i.e., $ET_c = ET_0 \times K_c$). The crop coefficient (K_c ; dimensionless) for the olive tree was assumed to be $K_c = 0.75$ (Rallo et al., 2010). The roots were distributed along the entire soil profile at the end of the experiment; therefore, the maximum root depth (z_r in cm) was assumed to be $z_{r0} = 42$ cm. Potential transpiration, T_p , was supposed to be ET_c since surface evaporation was set to zero. Thermal dissipation sensors were installed in the stems of both trees to record sap flow rates at 5-minute intervals (Granier, 1985). Measurements of near-surface soil water content (0-6 cm soil depth) were taken twice a day (morning and evening) using the ThetaProbe soil moisture sensor (ML2x type 2 ThetaProbe, Delta-T devices, Cambridge, UK). After the experiment, the soil capacitance readings were calibrated and converted into soil water contents through an empirical equation (Amin et al., 2021).

Stable isotopes of hydrogen and oxygen were used for the tracer experiment. The experiment duration was split into a 2-week conditioning period and a labelling period. The former began on May 16, 2018 when the plants were irrigated with 3 L of local tap water ($\delta^2\text{H}$ of $-52.3\text{‰} \pm 1.8\text{‰}$ and a $\delta^{18}\text{O}$ of $-7.97\text{‰} \pm 0.77\text{‰}$) every two days; the latter followed the conditioning period, and the potted trees were irrigated with 2, 3, or 5 L of labelled water ($\delta^2\text{H}$: $-93.3\text{‰} \pm 1.8\text{‰}$, and $\delta^{18}\text{O}$: $-12.75\text{‰} \pm 0.50\text{‰}$) approximately every two days for 5 weeks (Amin et al., 2021). Soil and twig samples for isotopic analyses were taken at the end of each week of the experiment. The twig samples were collected along the entire length of each selected branch, and the bark was removed before storing the samples. Soil cores were collected at three different depths, i.e., 0-5 cm, 5-15 cm, and 15-25 cm. All samples were stored in airtight 12 ml Labco Exetainer[®] glass vials (Labco Ltd., Lampeter, UK). At the end of the experiment (6 July 2018), additional soil and plant

samples were retrieved completely from O1 while the usual sampling was carried out from O2 (considered a replicate) (Amin et al., 2021). Irrigation water samples were collected from the tap water and labelled water for isotopic analysis. All the samples were stored in the refrigerator until the isotopic analysis.

The extraction of soil and xylem water was carried out by using the cryogenic vacuum distillation (CVD) method (Koeniger et al., 2011), performed in two different laboratories, at the Faculty of Science and Technology, Free University of Bozen-Bolzano (Italy), and at the Global Institute for Water Security, University of Saskatchewan (Canada). A detailed description of the two cryogenic vacuum distillation systems used in this work can be found in Amin et al. (2021). Data analysis showed that there was not a clear effect of the cryogenic vacuum distillation system on the isotopic composition of the extracted soil and plant waters (Amin et al., 2021). Therefore, in this study, we only considered $\delta^{18}\text{O}$ data from O1 obtained from the samples extracted at the Global Institute for Water Security, University of Saskatchewan (Canada). The isotopic composition of xylem water was determined by isotope ratio mass spectrometry at InnoTech Alberta (Edmonton, Canada), whereas the isotopic compositions of irrigation and soil water were measured by a Picarro isotope analyzer (cavity ring-down spectroscopy method, model L2130-i, manufactured by Picarro Inc., USA) at the Faculty of Science and Technology, Free University of Bozen-Bolzano (Italy) (Penna et al., 2010). The memory effect of laser-based measurements was minimized following the procedure reported by Penna et al. (2012).

4.2.2 Simulation of isotope transport in the potted olive tree experiment

We used Hydrus-1D for simulating one-dimensional water flow and isotope transport in the potted olive tree system by using the Richards and the advection-dispersion equations, respectively (Šimůnek et al., 2016).

The five van Genuchten parameters (θ_r , θ_s , α , n , and K_s) featuring the water retention and hydraulic conductivity functions were assessed through parameter optimisation (Supplementary material Table S 4-1). Irrigation supply and free drainage represent the upper and lower boundary conditions, respectively, whereas the potential evaporation (E_p) was assumed to be zero (see Section 4.2.1). Plant potential

transpiration, T_p , determines the potential RWU that takes place within the soil profile. The maximum rooting depth was set to 42 cm, and root density was maximum at the soil surface and minimum at the soil profile bottom, based on the visual inspection at the end of the experiment (see Section 4.2.1). T_p was reduced by water stress to actual transpiration (T_a). The simulation period was set to 1,234 hours. Hydraulic equilibrium was assumed as the initial condition by fixing $\psi = -42$ cm and $\psi = 0$ cm at the soil surface and soil profile bottom, respectively.

The observed isotopic composition of irrigation water was set as the concentration flux in the upper boundary condition. In contrast, a zero-concentration gradient (free drainage) was set as the lower boundary condition. The initial isotope composition of -4 ‰ in $\delta^{18}\text{O}$ was set through the soil profile.

4.2.3 Determination of root water uptake source and transit time with the virtual tracer experiment

Another set of model simulations was carried out using the virtual tracer injection experiment to assess the temporal origin of RWU. The number of numerical simulations depended on the total number of irrigation events. There were 26 irrigation events, and therefore Hydrus-1D was run 26 times by assigning the i th $\delta^{18}\text{O}$ value to the i th irrigation event and then setting $\delta^{18}\text{O}=0$ ‰ for all other irrigation events. The initial isotope composition across the soil profile was set to zero. RWU transit time, τ , is defined as the elapsed time between the irrigation inflow on the soil surface at time t_{in} and the RWU outflow of that water at time t_{out} (Sprenger et al., 2016).

We defined the tracer arrival time (t_{out}) as the cumulative root isotope uptake reaching 50% of the mass breakthrough curve (Sprenger et al., 2016). Therefore, τ was calculated as the difference between arrival time (t_{out}) and entry time (t_{in}) for each i -th irrigation event. The relative irrigation contribution to actual transpiration was calculated as the ratio between isotope flux output (through actual RWU) and isotope flux input (through irrigation) (Sprenger et al., 2016).

4.3 Results

4.3.1 Simulation of isotope transport in the potted olive tree experiment

Figure 4-2 shows the soil water response to the irrigation. The successive irrigation events (blue bars in Figure 4-2a) rapidly increased the soil water storage (wet conditions across the soil profile are indicated by the bluish colour in Figure 4-2b), and the high transpiration rates induced a gradual desaturation of the soil profile after the irrigation events. These effects were enhanced near the soil surface (despite evaporation being largely absent), where root distribution was at its maximum.

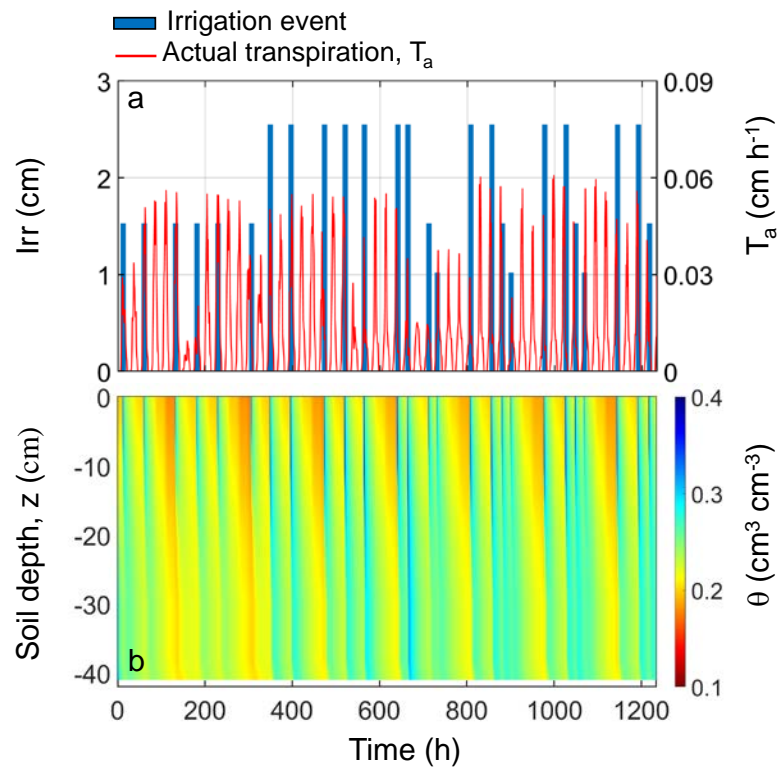


Figure 4-2 Hourly data of a) water irrigation (Irr) events (blue bars), actual transpiration, T_a (red line), and b) soil water content, θ (from red to blue indicated in the colour bar indicating dry to wet conditions) across the soil profile simulated in Hydrus-1D.

Figure 4-3 shows that the soil isotopic composition reflected the water mixtures originating from all irrigation events. The vertical distribution of the $\delta^{18}\text{O}$ composition was quite uniform (bluish colour of soil water in Figure 4-3b) when the irrigation events with local tap water ($\delta^{18}\text{O} = -7.97\text{‰}$, blue bars in Figure 4-3a) were applied during the first (2 week-long) conditioning period. $\delta^{18}\text{O}$ values gradually decreased towards more depleted compositions when the irrigation events

with labelled water ($\delta^{18}\text{O}=-12.75\text{‰}$, yellow bars in Figure 4-3a) were applied during the second (5 week-long) period.

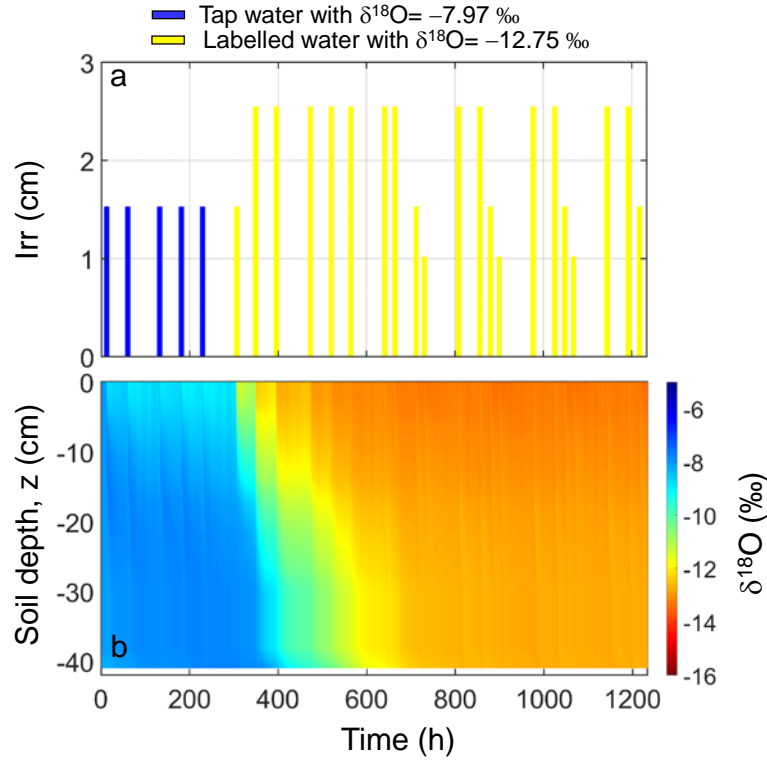


Figure 4-3 Hourly data of a) tap (blue bars with $\delta^{18}\text{O} = -7.97 \text{‰}$) and labelled (yellow bars with $\delta^{18}\text{O} = -12.75 \text{‰}$) b) $\delta^{18}\text{O}$ (from red to blue indicated in the colorbar) across the soil profile simulated in Hydrus-1D.

4.3.2 Determination of root water uptake source and transit time through the virtual tracer experiment

An illustrative example of the steps for assessing the transit time for two 3 L labelled irrigation events is shown in Figure 4-4. The first event with tap water and the 14th event with labelled water are indicated by the black bars in Figure 4-4a-b. Isotope transport across the soil profile (Figure 4-4c-d) depended on the frequency and amounts of irrigation events, actual transpiration, and drainage fluxes following the selected labelled irrigation event (Figure 4-4a-b). Both events were characterised by very similar transit times ($\tau = 119 \text{ h}$ and $\tau = 116 \text{ h}$) even though the transpired water amount in the first case (1st event) almost doubled that in the second case (14th event). The proportion of i -th irrigation isotope and cumulative

root isotope uptake was 38.3 % and 22.6 % for the 1st and 14th irrigation events, respectively.

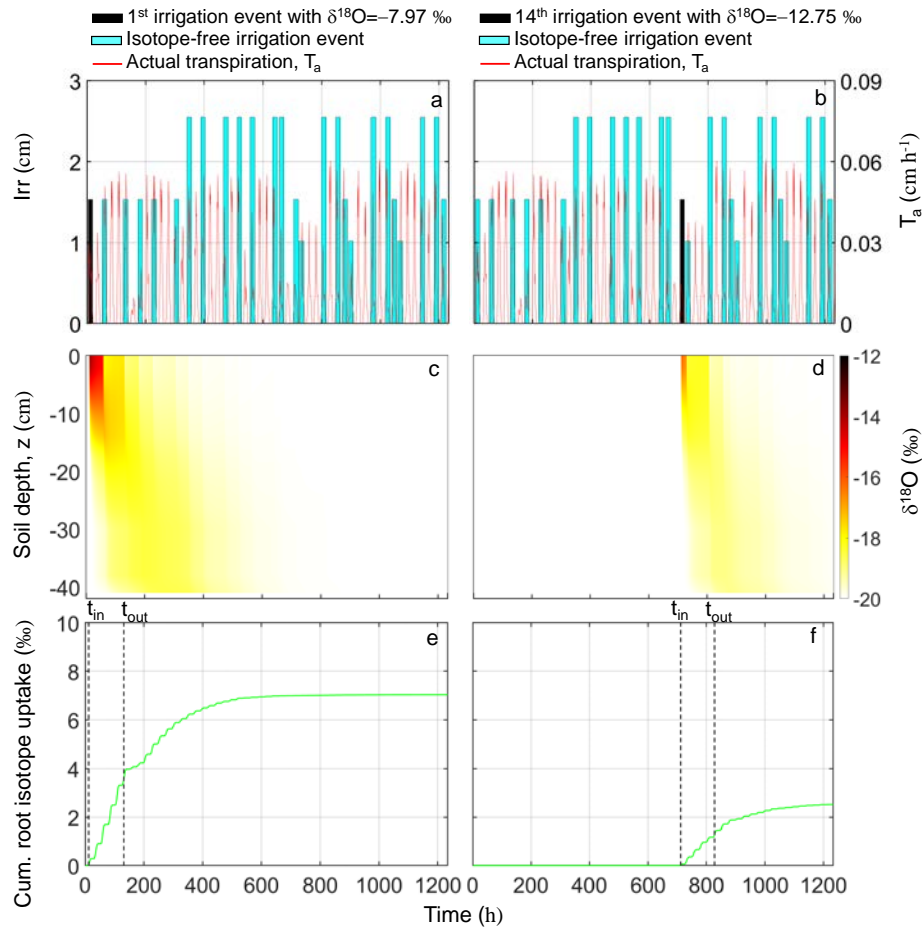


Figure 4-4 Hourly data of a-b tap (1st event) and labelled (14th event) water irrigation (Irr) event (black bar) with known $\delta^{18}\text{O}$ signature, isotope-free irrigation events (cyan bars), actual transpiration, T_a (red line), c-d $\delta^{18}\text{O}$ (from white to black indicated in the colorbar) across the soil profile, e-f cumulative root $\delta^{18}\text{O}$ uptake (green line). Vertical dashed lines indicate entry (t_{in}) and arrival (t_{out}) times.

The descriptive statistics of RWU transit time and proportion of irrigation to actual transpiration are listed in Table 4-1 while all events are reported in Appendix 4-1. The first five irrigation events were characterised by tap water ($\delta^{18}\text{O} = -7.97\text{‰}$) in the conditioning period, while the remaining 21 events based on labelled water ($\delta^{18}\text{O} = -12.75\text{‰}$) were applied in the second five-week-long period. It has to be noted that the last five irrigation events were removed from data analysis because the arrival time occurred beyond the end of the model simulation.

Table 4-1 Mean, standard deviation, coefficient of variation, minimum and maximum amounts of irrigation (Irr), transit time (τ), and irrigation contribution to actual transpiration (T_a/Irr) for the first 21 irrigation events used in this study. The last five events were ignored because their arrival time exceeded the time of the model simulation.

	Irr (cm)	τ (h)	T_a/Irr (%)
Mean	2.02	95.43	25.65
standard deviation	0.59	22.24	7.53
coefficient of variation	29.37	23.30	29.35
min.	1.02	62.00	14.92
max.	2.55	136.00	40.68

The arrival time (t_{out}) and transit time (τ) values depended on water and isotope mass balance. As the labelled irrigation water moved through the soil profile, it carried its isotope concentration load as described by the advection-dispersion equation. Meaning, part of it was absorbed by roots (Figure 4-4e-f), another part was lost by drainage at the base of the soil profile, and the remaining portion was retained in the soil (Figure 4-4c-d). The mean irrigation supply and relative contributions of irrigation to actual transpiration were on average about 2.0 cm and 26%, respectively, allowing for the fact that evaporation was set at zero while the remaining portion of irrigation water was lost by drainage. In other words, the water amount of 0.52 cm was removed by roots under optimal water conditions with a mean transit time of about 95 h. The low coefficient of variation (below 30%) of τ and T_a/Irr indicates the impact of regular irrigation management on water flow and isotope transport in the SPAC.

Figure 4-5 helps interpret RWU dynamics originating from each irrigation event. We note the shape similarity between cumulative root water uptake (Figure 4-5a) and root isotope uptake (Figure 4-5b) patterns up until the arrival time.

These curves represent the first half of RWU, as the arrival time was identified when the cumulative root isotope uptake reached 50% of its final value. Ideally, the root isotope uptake sums would perfectly align with the corresponding root water uptake sums on a linear regression line (Figure 4-5c). Instead, the data pairs scatter around the fitted linear regression line with a coefficient of determination (R^2) equal to 0.67, indicating that 67% of root isotope uptake variability is controlled by

transpiration rates. Short transit times (bluish circles in Figure 4-5c) are related to the steepest cumulative root isotope uptake curves (Figure 4-5b).

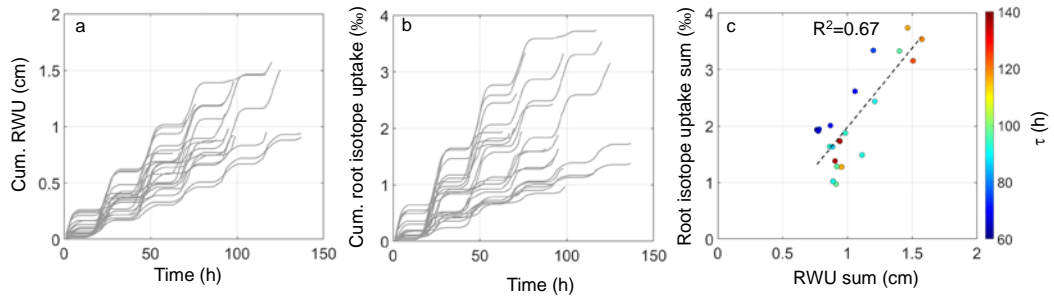


Figure 4-5 a) Cumulative root water uptake (RWU) till arrival time for each irrigation event, b) cumulative root isotope uptake till arrival time for each irrigation event, c) relationship between RWU and root isotope uptake sums with dashed line indicating the fitting linear regression equation with corresponding coefficient of determination (R^2); the circles are colour-coded according to the corresponding RWU transit time (τ).

4.4 Discussion

4.4.1 Quantifying irrigation uptake dynamics

Our proof of concept work was an ensemble simulation approach (the virtual tracer injection experiment) to trace soil water pathways in the SPAC originating from individual irrigation events. Any isotope concentration can be applied in the virtual tracer injection experiment, which enables the calculation of RWU transit time and the calculation of the contribution of irrigation water to plant transpiration. The repeated model simulations indicate that, on average, water travels across the soil for about 95 h (roughly corresponding to 4 days) before being taken up by roots. Moreover, the average irrigation depth is 2.02 cm, and about 26 % of it is absorbed by the roots, according to the isotope mass balance. The results of the water balance show that the amount of water taken up by the roots was 14.1 cm, while the amount supplied by irrigation was 51.6 cm (RWU represents 27.3% of total irrigation). Therefore, the water balance corroborates the isotope mass balance, in which RWU represents 25.6 % of total irrigation.

The temporal origin of RWU from each irrigation event was determined by tracking root isotope uptake, which depended mainly on transpiration rates following the labelled irrigation event and on the isotope mass balance across the soil profile, which in turn was influenced by irrigation timing and amounts (Figure 4-5). The regular irrigation management and transpiration fluxes induced low variability of transit time and irrigation partitioning values (Table 4-1).

In this study, the virtual tracer experiment combined the Richards equation and the advection-dispersion equations to simulate transit time in a potted olive tree experiment. This approach relies on the assumption that the arrival time corresponds to the time when the tracer mass breakthrough reaches 50% (Sprenger et al., 2016). Therefore, the virtual tracer experiment needs to be evaluated against other well-established approaches, such as the particle tracking algorithm or the water age equation. The former describes the advection-dominated flow pathways in the SPAC, while the latter explicitly models water age (e.g., Danesh-Yazdi et al., 2018; Zarlenga and Fiori, 2020). However, such approaches were tested mainly at the catchment and hillslope scales (Wilusz et al., 2020; Zarlenga et al., 2022). The comparison between the virtual tracer experiment and other well-known approaches

can be tested at the plot or tree scale, by exploiting hydro-chemical measurements in isotope-labelled water experiments.

By raising model complexity (i.e., preferential flow in a heterogeneous soil profile, capillary rise from the shallow aquifer) in real-world situations, the temporal origin can reveal interesting aspects of the SPAC response to irrigation management and climate seasonality if well supported by *ad hoc* measurements (Yin et al., 2015). Multi-modal transit time distributions are expected under seasonal climate regimes in field-scale applications.

4.4.2 Model limitations

Measurements of soil water content and $\delta^{18}\text{O}$ at different soil depths were integrated to optimise the soil hydraulic properties in Hydrus-1D via inverse modelling (Groh et al., 2018; Zhou et al., 2022). This is presented in the Supplementary Figure S 4-1). We recognise that model oversimplification might increase the discrepancy between observed and simulated isotopic compositions at different soil depths. The root water uptake is controlled by the root depth, root distribution, and the root-water uptake water stress function (Feddes et al., 1978). In this study, we had the opportunity to visualise root depth and distribution with a destructive approach at the end of the experiment (see Amin et al., 2021), but the Feddes function merits particular attention for determining actual transpiration (Rabbal et al., 2018; de Melo and de Jong van Lier, 2021). Model simulations were validated by using independent observations of sap flow and isotope composition in xylem water (Supplementary Figure S 4-2). In our analysis, we assumed that no fractionation occurred in either evaporation from the soil surface (along the pathway from the soil up to the roots) or transpiration (along the pathway from the roots up to the leaves). This assumption was verified for this specific case study (Amin et al., 2021), but is not generally applicable to other locations and other climate conditions (Martín-Gómez et al., 2017; Poca et al., 2019; de Deurwaerder et al., 2020).

4.5 Concluding remarks

The use of a combined isotope tracing and Hydrus-1D approach was able to quantify the temporal origin of water taken up by roots in a potted olive tree. The water parcels introduced with irrigation events were virtually traced across the soil profile to assess RWU transit time and the proportion of irrigation water to actual transpiration. The statistical distribution of transit times represents a functional indicator that can be used to characterise the reaction of the SPAC to irrigation management and climate seasonality. The results presented in this study pave the way for future field applications in which long-term model simulations will generate site-specific transit time distributions of all water balance components (RWU, evaporation, and drainage) in response to adverse climate disturbances (i.e., drought).

APPENDIX

Appendix 4-1 Entry time (t_{in}), irrigation (Irr) amount and $\delta^{18}\text{O}$, arrival time (t_{out}), transit time (τ), and rainfall contribution to actual transpiration (T_a/Irr) for the 26 irrigation events used in this study. Last five events were ignored in the data analysis.

t_{in} (h)	Irr (cm)	$\delta^{18}\text{O}$ (‰)	t_{out} (h)	τ (h)	T_a/Irr (%)
12	1.53	-8.0	131	119	38.3
60	1.53	-8.0	176	116	40.7
132	1.53	-8.0	256	124	34.2
181	1.53	-8.0	278	97	36.5
229	1.53	-8.0	304	75	36.2
306	1.53	-12.7	398	92	26.7
349	2.55	-12.7	440	91	26.3
396	2.55	-12.7	466	70	28.3
473	2.55	-12.7	535	62	21.0
520	2.55	-12.7	614	94	17.3
564	2.55	-12.7	637	73	20.3
641	2.55	-12.7	777	136	14.9
664	2.55	-12.7	800	136	18.6
712	1.53	-12.7	828	116	22.6
731	1.02	-12.7	829	98	26.1
808	2.55	-12.7	877	69	21.7
856	2.55	-12.7	950	94	20.3
880	1.53	-12.7	977	97	22.9
900	1.02	-12.7	992	92	27.3
977	2.55	-12.7	1043	66	20.6
1026	2.55	-12.7	1113	87	17.7
1048	1.53	-12.7	1117	69	21.2
1068	1.02	-12.7	1118	50	24.7
1144	2.55	-12.7	1187	43	10.5
1192	2.55	-12.7	1212	20	4.0
1217	1.53	-12.7	1232	15	1.1

SUPPLEMENTARY MATERIAL

S4 Quantifying irrigation uptake in olive trees: A proof of concept approach combining isotope tracing and Hydrus-1D

S4.1 Soil water balance and isotope transport in Hydrus-1D

We used Hydrus-1D for simulating one-dimensional water flow in the SPAC (Šimůnek et al., 2016). The water balance in the system was computed using the Richards equation:

$$\frac{\partial \theta}{\partial t} = \frac{\partial}{\partial z} \left[K(\psi) \left(\frac{\partial \psi}{\partial z} + 1 \right) \right] - \xi(z, \psi, T_p)$$

Supplementary material Eq. S (4-1)

where t (h) is time, ψ (cm) is soil matric head, z (cm) is soil depth (positive upward), θ ($\text{cm}^3 \text{ cm}^{-3}$) is volumetric soil water content, K (cm h^{-1}) is the hydraulic conductivity, and ξ (z , ψ , and T_p) (h^{-1}) is a sink term describing the actual plant root water extraction rate, which depends on z , ψ , and potential transpiration (T_p). In this study, time and length units were set in hours (h) and centimetres (cm), respectively. In Hydrus-1D, the numerical integration of Supplementary material Eq. S (4-1) was performed using a finite element scheme for spatial discretization and a finite difference scheme for time discretization. The water retention function, $\theta(\psi)$ is described by van Genuchten's equation (van Genuchten, 1980):

$$\theta(\psi) = \theta_r + \frac{\theta_s - \theta_r}{[1 + |\alpha \psi|^n]^m}$$

Supplementary material Eq. S (4-2)

where α (cm^{-1}), m (-), and n (-) are the water retention function shape parameters, whereas θ_r ($\text{cm}^3 \text{ cm}^{-3}$) and θ_s ($\text{cm}^3 \text{ cm}^{-3}$) are the residual and saturated soil water contents, respectively. The two shape parameters m and n are related as follows: $m=1-1/n$ (van Genuchten, 1980).

The degree of saturation, S_e is defined as:

$$S_e = \frac{\theta - \theta_r}{\theta_s - \theta_r}$$

Supplementary material Eq. S (4-3)

which varies from 0 ($\theta = \theta_r$) to 1 ($\theta = \theta_s$). The unsaturated hydraulic conductivity function, $K(S_e)$, is given by the following equation (van Genuchten, 1980):

$$K(S_e) = K_s S_e^l \left[1 - (1 - S_e^{1/m})^m \right]^2$$

Supplementary material Eq. S (4-4)

where K_s (cm h⁻¹) is the saturated hydraulic conductivity, and l (-) is a tortuosity parameter that is assumed to be $l = -1$ (Schaap *et al.*, 2000).

The actual root water extraction rate, ξ , was modeled using the Feddes-style RWU model (Feddes *et al.*, 1978). T_p was reduced below $\psi = -500$ cm or below $\psi = -800$ cm if the transpiration rate was high or low, respectively. The wilting point of the olive tree was assumed to be -2.5 MPa, which corresponds to $\psi = -25,493$ cm (Brito *et al.*, 2019).

The governing equation for isotope transport during transient water flow in a variably-saturated, rigid, porous medium is:

$$\frac{\partial \theta C}{\partial t} = \frac{\partial}{\partial z} \left(\theta D^w \frac{\partial C}{\partial z} \right) - \frac{\partial (qC)}{\partial z} - \xi C$$

Supplementary material Eq. S (4-5)

where C corresponds to $\delta^{18}\text{O}$ in liquid water assumed as isotope concentration, q is the volumetric flux density (cm h⁻¹), and D^w is the dispersion coefficient (cm² h⁻¹) for the liquid phase.

The dispersion coefficient in the liquid phase, D^w , is given as:

$$D^w = D_L \frac{|q|}{\theta} + D_w T_w$$

Supplementary material Eq. S (4-6)

where D_w is the molecular diffusion coefficient in free water (cm² h⁻¹), T_w is a unitless tortuosity factor in the liquid phase, $|q|$ is the absolute value of the Darcian flux density (cm h⁻¹), and D_L is the longitudinal dispersivity (cm).

The solute transport module in Hydrus-1D was specifically modified to account for isotope transport (Stumpp *et al.*, 2012). This module is only applicable for conditions where fractionation due to evaporation is of minor importance. Evaporation from the soil surface was assumed to be equal to zero, and therefore the fractionation process during evaporation was neglected. Moreover, the previous

study on the same dataset showed no evidence of isotopic fractionation in xylem water induced by olive tree transpiration (Amin et al., 2021).

The longitudinal dispersivity, D_L , was assumed to be 4.2 cm (corresponding to 1/10th of the soil profile depth) (Gelhar et al., 1992; Vanderborght and Vereecken, 2007; Brunetti et al., 2020; Nasta et al., 2021).

S4.2 Parameter optimisation via inverse modelling in Hydrus-1D

Hydrus-1D requires, among other inputs, knowledge of the soil hydraulic properties (soil water retention function, WRF, and hydraulic conductivity function, HCF) that control the water fluxes and consequently isotope transport across the critical zone. Direct measurements of WRF and HCF are commonly based on accurate but time-consuming and labour-demanding soil sampling and laboratory tests, such as the evaporation method (Romano and Santini, 1999), and multi-step outflow techniques (Eching et al., 1994), or in-situ experiments (Romano, 1993). Another viable option is the inverse modelling approach in the form of parameter optimisation to enable the simultaneous estimation of WRF and HCF based on measurements of state variables and water fluxes (Hopmans et al, 2002), recently integrated with isotope data in soil water (Sprenger et al., 2015; Groh et al., 2018). The Marquardt-Levenberg type parameter optimisation algorithm for inverse estimation of the unknown soil hydraulic parameters (θ_r , θ_s , α , n , and K_s) is embedded in Hydrus-1D. Generally speaking, the local-search Marquardt-Levenberg type algorithm is reliable only if the number of parameters to be optimised is low (by decreasing the effect of collinearity on the parametric optimization), initial and boundary conditions are affected by acceptable measurement errors (by relaxing the effect of being ill-posed on the parametric optimisation) and the observed data in the objective function are informative enough to avoid parametric equifinality. To reduce the number of parameters, we assumed $\theta_r = 0$ and $\theta_s = 0.408 \text{ cm}^3 \text{ cm}^{-3}$ as the latter was assumed to be 90% of soil porosity, which in turn is calculated from the oven-dry bulk density.

The remaining three soil hydraulic parameters (α , n , and K_s) were optimised by minimising the residuals between observed and fitted soil water content and $\delta^{18}\text{O}$ at specific depths of the soil profile. To this end, three observation points in Hydrus-

1D were placed at $z = -3$ cm, -10 cm, and -20 cm corresponding to the following soil sampling depths: 0-5 cm, 5-15 cm, and 15-25 cm. Vector \mathbf{p} and the observed and simulated hydrological and isotopic data were included in the objective function, ϕ , as follows:

$$\min_p \phi(p) = \min_p \left\{ \sum_{t=1}^n [\theta_{obs}(t, z) - \theta_{sim}(t, z, p)]^2 + \sum_{t=1}^n [\delta^{18}O_{obs}(t, z) - \delta^{18}O_{sim}(t, z, p)]^2 \right\}$$

Supplementary material Eq. S (4-7)

where $\theta_{obs}(t, z)$ and $\theta_{sim}(t, z, p)$ denote the observed and simulated soil water content data at $z = -3$ cm at time step t , respectively, whereas $\delta^{18}O_{obs}(t, z)$ and $\delta^{18}O_{sim}(t, z, p)$ are the observed and modelled isotope composition values at three soil depths ($z = -3$ cm, $z = -10$ cm, $z = -20$ cm) at time step, t , respectively. The two data sets were weighed by their standard deviations.

Model performance measures are based on the root mean square error (RMSE) and coefficient of determination (R^2) defined as:

$$RMSE = \sqrt{\frac{1}{n} \sum_i^n (O_i - P_i)^2}$$

Supplementary material Eq. S (4-8)

$$R^2 = \frac{\sum_i^n (O_i - P_i)^2}{\sum_i^n (O_i - \bar{O})^2}$$

Supplementary material Eq. S (4-9)

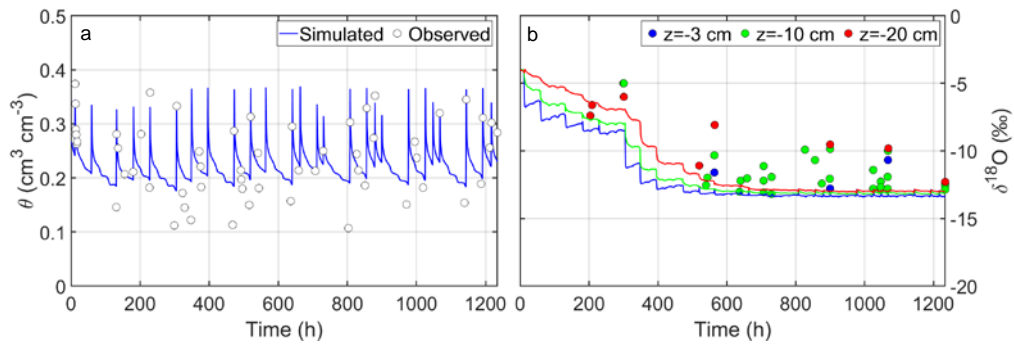
where O , \bar{O} , and P are the observed, mean of observed, and predicted values of either soil water content or stable isotope composition at time step i expressed in hours (n is the total number of time steps). For an optimum prediction, values should be as low as possible for RMSE and as close as possible to 1.

The optimised parameters α and K_s reflect well the hydraulic characteristics of a mixture of sandy loam and pumice, while the water retention shape parameter n is lower than expected and is significantly correlated with K_s (Supplementary material Table S 4-1). Anyway, the calibrated soil hydraulic parameters led to fair model

performance when comparing observed and simulated soil water content (RMSE = $0.0474 \text{ cm}^3 \text{ cm}^{-3}$ and $R^2 = 0.56$) at $z = -3 \text{ cm}$ (Supplementary Figure S 4-1a). The observed soil water content data ranges between 0.107 and $0.388 \text{ cm}^3 \text{ cm}^{-3}$. The simulated soil water content data fairly match the observed data except for values below $0.2 \text{ cm}^3 \text{ cm}^{-3}$, while the isotopic composition simulated in Hydrus-1D reflects the change in irrigation water (from tap water to labelled water). The observed $\delta^{18}\text{O}$ values of soil water range from -5.0 ‰ at $z = -3 \text{ cm}$ to -13.2 ‰ at $z = -10 \text{ cm}$ with high variability probably suggesting a slow mixing of irrigation water in the porous matrix (see coloured circles in Supplementary Figure S 4-1b). We point out possible different velocities in the water percolation induced by the presence of preferential flow pathways in the soil profile, which might influence the observed isotopic composition, especially at the soil depth between -15 and -25 cm (Amin et al., 2021). The simulated $\delta^{18}\text{O}$ composition (RMSE = 1.63 ‰ and $R^2 = 0.73$) values at $z = -3 \text{ cm}$, $z = -10 \text{ cm}$, $z = -20 \text{ cm}$ show a smooth decrease in time and are unable to match some episodic depletion of the corresponding observations (see coloured lines in Supplementary Figure S 4-1b). Beyond expected measurement errors affecting the isotopic composition of soil water, the model setup hardly reflects the real soil heterogeneity, even under pot conditions.

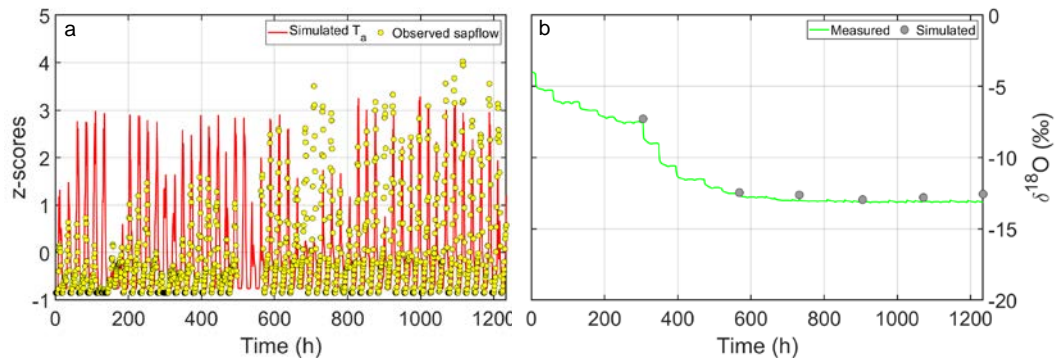
Supplementary material Table S 4-1. Optimised values of the soil hydraulic parameters α , n , and K_s with their 95% confidence limits and correlation matrix.

Parameter	Units	Optimised value	95% confidence limits		Correlation matrix		
			Lower	Upper	α	n	K_s
α	cm^{-1}	0.254	0.127	0.380	1		
n	-	1.31	1.24	1.37	-0.18	1	
K_s	cm h^{-1}	23.61	1.83	45.38	0.01	-0.76	1



Supplementary Figure S 4-1. Hourly data of a) observed (white circles) and simulated (blue line) soil water content values at $z = -3$ cm and b) observed (coloured circles) and simulated (coloured lines) $\delta^{18}\text{O}$ (‰) at $z = -3$, $z = -10$, and $z = -20$ cm.

Observed sap flow data and simulated root water uptake (corresponding to actual transpiration, T_a) are not fully comparable, and therefore, these two variables were converted into their corresponding z -scores. Supplementary Figure S 4-2a shows that, in the early stages, the observed sap flow (yellow circles) underestimated the simulated root water uptake z -scores (red line), whereas for time values greater than 600 hours, a much better agreement occurred between observations and model simulations. The model's performance in terms of z -scores is indicated by $\text{RMSE} = 0.931$ and $R^2 = 0.30$. A final validation step was performed by comparing observed and simulated $\delta^{18}\text{O}$ ($\text{RMSE} = 0.931$ ‰ and $R^2 = 0.99$) values in the xylem water. The observed isotopic composition of the extracted water from olive twigs changes from $\delta^{18}\text{O} = -7.28$ ‰ (± 0.53 ‰) on May 28, 2018, up to $\delta^{18}\text{O} = -12.56$ ‰ (± 0.19 ‰) on July 6, 2018. The few observations (only six observations in Supplementary Figure S 4-2b) matched almost perfectly the corresponding model simulations and reflected the signature of the labelled water of the irrigation events.



Supplementary Figure S 4-2. Hourly data of a) observed sap flow (yellow circles) and simulated actual transpiration, T_a (red line) z-scores, and b) observed (grey circles) and simulated (green line) $\delta^{18}\text{O}$ (‰) in the twig tissues.

The model set up applied to real-world agricultural field conditions should raise complexity based on a large amount of data. In field-scale inverse modelling the soil hydraulic properties of the soil layers vary considerably; therefore, layer-specific observations of pressure head, soil water content, and isotope composition are prerequisites to inversely determining the soil hydraulic parameters of different layers (Schelle et al., 2012). If supported by many integrated observations, the model setup can be enhanced by adding more complex dynamics such as preferential flow, hysteresis in the water retention function, and root water uptake compensation, to mention a few, at the cost of increasing the number of parameters to be optimised in the inverse modelling routine. The degree of model complexity can significantly raise the realm of water flux and isotope transport across the vadose zone. The impact of evaporation and related fractionation and capillary rise from a shallow aquifer is expected in most field situations (Yin et al., 2015). Evaporation fractionation enriches the isotopic composition in shallow soil water, while capillary rise, supplying water and isotopes to the vadose zone with upward flow rates, influences the isotope composition in the deeper soil layers.

5 Conclusion

The issues of the impact of climate and land use changes on water resources are of practical interest for land managers, stakeholders and policy makers at landscape and regional scales.

At these large scales, water management strategies should be adopted based on accurate and detailed input information on most environmental variables. One of the most influential and sustainable approaches is producing maps containing suitable indicators that reflect the complex dynamics of water resources in landscape and regional contexts.

In this thesis, an innovative method to identify dynamic resilience indicators has been successfully developed. These dynamic indicators provide a more complete and dynamic view than traditional static approaches of how an ecosystem responds to perturbations. An example of such an indicator is the "travel time" which is used to assess the vulnerability of shallow groundwater to climate change and human activities.

However, it is crucial to recognize that, despite the effectiveness of such approaches at a regional or territorial scale, there is always a need to verify and validate assessments at a local level. Hydrological challenges can vary greatly even within a region or territory, so it is crucial to understand the specific local conditions and interactions between soil and vegetation.

In this perspective, the thesis was concerned with carrying out specific investigations at two smaller scales: the scale of sub-catchment with different land uses, and at the point scale of a soil-plant system.

Future studies could focus on developing adaptive management strategies that consider the dynamic information provided by indicators. This could help management bodies respond more quickly and effectively to changes in water resources. Furthermore, future scenario modeling could be further developed to predict how impacts on hydrological systems might evolve in response to climate and land use changes and enable more proactive planning.

Involving local communities in data collection and decision-making could be crucial for sustainable water management.

6 References

- Adhikari, K., & Hartemink, A. E. (2016). Linking soils to ecosystem services—A global review. *Geoderma*, 262, 101-111.
- Aguilera, E., Diaz-Gaona, C., Garcia-Laureano, R., Reyes-Palomo, C., Guzmán, G. I., Ortolani, L., ... & Rodriguez-Estevez, V. (2020). Agroecology for adaptation to climate change and resource depletion in the Mediterranean region. A review. *Agricultural Systems*, 181, 102809.
- Aguzzoni, A., Engel, M., Zanutelli, D., Penna, D., Comiti, F., & Tagliavini, M. (2022). Water uptake dynamics in apple trees assessed by an isotope labeling approach. *Agricultural Water Management*, 266, 107572.
- Alessandri, A., De Felice, M., Zeng, N., Mariotti, A., Pan, Y., Cherchi, A., ... & Artale, V. (2014). Robust assessment of the expansion and retreat of Mediterranean climate in the 21st century. *Scientific reports*, 4(1), 1-8.
- Allen, R. G., Pereira, L. S., Raes, D., & Smith, M. (1998). Crop Evapotranspiration-Guidelines for computing crop water requirements-FAO Irrigation and drainage paper 56. Fao, Rome, 300(9), D05109.
- Allen, W. J., Bufford, J. L., Barnes, A. D., Barratt, B. I., Deslippe, J. R., Dickie, I. A., ... & Tylianakis, J. M. (2022). A network perspective for sustainable agroecosystems. *Trends in Plant Science*.
- Amin, A., Zuecco, G., Marchina, C., Engel, M., Penna, D., McDonnell, J. J., & Borga, M. (2021). No evidence of isotopic fractionation in olive trees (*Olea europaea*): a stable isotope tracing experiment. *Hydrological Sciences Journal*, 66(16), 2415-2430.
- Asadollahi, M., Nehemy, M. F., McDonnell, J. J., Rinaldo, A., & Benettin, P. (2022). Toward a closure of catchment mass balance: Insight on the missing link from a vegetated lysimeter. *Water Resources Research*, 58(4), e2021WR030698.
- Attwood, S., Bossio, D., Girvetz, E., Chaplin-kramer, B., Declerck, F., Enfors, E., & Willemsen, L. (2014). Ecosystem Services and Resilience Framework: CGIAR Research Program on Water, Land and Ecosystems (WLE).
- Bai, Y., Ochuodho, T. O., & Yang, J. (2019). Impact of land use and climate change on water-related ecosystem services in Kentucky, USA. *Ecological Indicators*, 102, 51-64.

- Barbeta, A., Burlett, R., Martín-Gómez, P., Fréjaville, B., Devert, N., Wingate, L., ... & Ogée, J. (2022). Evidence for distinct isotopic compositions of sap and tissue water in tree stems: consequences for plant water source identification. *New Phytologist*, 233(3), 1121-1132.
- Barbeta, A., Gimeno, T. E., Clavé, L., Fréjaville, B., Jones, S. P., Delvigne, C., ... & Ogée, J. (2020). An explanation for the isotopic offset between soil and stem water in a temperate tree species. *New Phytologist*, 227(3), 766-779.
- Batsukh, K., Zlotnik, V. A., & Nasta, P. (2022). Analysis of Groundwater Recharge in Mongolian Drylands Using Composite Vadose Zone Modeling. *Frontiers in Water*, 4, 7.
- Benettin, P., Nehemy, M. F., Asadollahi, M., Pratt, D., Bensimon, M., McDonnell, J. J., & Rinaldo, A. (2021). Tracing and closing the water balance in a vegetated lysimeter. *Water Resources Research*, 57(4), e2020WR029049.
- Benettin, P., Volkmann, T. H., von Freyberg, J., Frentress, J., Penna, D., Dawson, T. E., & Kirchner, J. W. (2018). Effects of climatic seasonality on the isotopic composition of evaporating soil waters. *Hydrology and Earth System Sciences*, 22(5), 2881-2890.
- Bennett, E. M., Cramer, W., Begossi, A., Cundill, G., Díaz, S., Egoh, B. N., ... & Woodward, G. (2015). Linking biodiversity, ecosystem services, and human well-being: three challenges for designing research for sustainability. *Current opinion in environmental sustainability*, 14, 76-85.
- Beyer, M., and Penna, D., 2021. On the spatio-temporal under-representation of isotopic data in ecohydrological studies. *Frontiers in Water*, 3, 643013. <https://doi.org/10.3389/frwa.2021.643013>
- Beyer, M., Hamutoko, J. T., Wanke, H., Gaj, M., & Koeniger, P. (2018). Examination of deep root water uptake using anomalies of soil water stable isotopes, depth-controlled isotopic labeling and mixing models. *Journal of Hydrology*, 566, 122-136.
- Bierkens, M. F., Finke, P. A., & De Willigen, P. (2000). Upscaling and downscaling methods for environmental research. *Developments in plant and soil sciences*, 88.

- Bittelli, M., & Flury, M. (2009). Errors in water retention curves determined with pressure plates. *Soil Science Society of America Journal*, 73(5), 1453-1460.
- Bonacci, O., Pipan, T., & Culver, D. C. (2009). A framework for karst ecohydrology. *Environmental Geology*, 56, 891-900.
- Boumaiza, L., Chesnaux, R., Walter, J., & Stumpp, C. (2021). Constraining a flow model with field measurements to assess water transit time through a vadose zone. *Groundwater*, 59(3), 417-427.
- Bowers, W. H., & Williams, D. G. (2022). Isotopic Heterogeneity of Stem Water in Conifers Is Correlated to Xylem Hydraulic Traits and Supports Multiple Residence Times. *Frontiers in Water*, 4, 861590.
- Bowers, W. H., & Williams, D. G. (2022). Isotopic Heterogeneity of Stem Water in Conifers Is Correlated to Xylem
- Bowers, W. H., Mercer, J. J., Pleasants, M. S., & Williams, D. G. (2020). A combination of soil water extraction
- Bowling, D.R., E.S. Schulze, and S.J. Hall (2017), Revisiting streamside trees that do not use stream water: can the two water worlds hypothesis and snowpack isotopic effects explain a missing water source? *Ecohydrology*, 10(1), 1771.
- Brauman, K. A., Daily, G. C., Duarte, T. K. E., & Mooney, H. A. (2007). The nature and value of ecosystem services: an overview highlighting hydrologic services. *Annu. Rev. Environ. Resour.*, 32, 67-98.
- Brinkmann, N., Seeger, S., Weiler, M., Buchmann, N., Eugster, W., & Kahmen, A. (2018). Employing stable isotopes to determine the residence times of soil water and the temporal origin of water taken up by *Fagus sylvatica* and *Picea abies* in a temperate forest. *New Phytologist*, 219(4), 1300-1313.
- Brito, C., Dinis, L. T., Moutinho-Pereira, J., & Correia, C. M. (2019). Drought stress effects and olive tree acclimation under a changing climate. *Plants*, 8(7), 232.
- Brodribb, T. J., Powers, J., Cochard, H., & Choat, B. (2020). Hanging by a thread? Forests and drought. *Science*, 368(6488), 261-266.
- Brooks, J.R., H.R. Barnard, R. Coulombe, and J.J. McDonnell (2010), Ecohydrologic separation of water between trees and streams in a Mediterranean climate. *Nature Geoscience* 3 (2), 100-104.

- Brunetti, G., Šimůnek, J., Glöckler, D., & Stumpp, C. (2020). Handling model complexity with parsimony: Numerical analysis of the nitrogen turnover in a controlled aquifer model setup. *Journal of Hydrology*, 584, 124681.
- Burrough, P.A., R.A. McDonnell, 1988. *Principles of Geographical Information Systems*. Oxford: University Press.
- Buttafuoco, G., Quarto, R., Quarto, F., Conforti, M., Venezia, A., Vitti, C., & Castrignanò, A. (2021). Taking into account change of support when merging heterogeneous spatial data for field partition. *Precision Agriculture*, 22, 586-607.
- Carroll, S. S., & Cressie, N. (1996). A Comparison of Geostatistical Methodologies Used to Estimate Snow Water Equivalent 1. *JAWRA Journal of the American Water Resources Association*, 32(2), 267-278.
- Castrignanò, A., Buttafuoco, G., Quarto, R., Parisi, D., Rossel, R. V., Terribile, F., ... & Venezia, A. (2018). A geostatistical sensor data fusion approach for delineating homogeneous management zones in Precision Agriculture. *Catena*, 167, 293-304.
- Castrignanò, A., Costantini, E. A., Barbetti, R., & Sollitto, D. (2009). Accounting for extensive topographic and pedologic secondary information to improve soil mapping. *Catena*, 77(1), 28-38.
- Castrignanò, A., G. Buttafuoco, 2020. Data Processing. In: *Agricultural Internet of Things and Decision Support for Precision Smart Farming* (A. Castrignanò, G. Buttafuoco, R. Khosla, A.M. Mouazen, D. Moshou, O. Naud, eds.), Chapter 3, pp. 139-182, Academic Press, London, United Kingdom, ISBN: 978-0-12-818373-1.
- CBD (Convention on Biological Diversity). 1992. *Convention on Biological Diversity*. United Nations
- Chen, G., Guo, J., Song, Z., Feng, H., Chen, S., & Li, M. (2022). Soil water transport and plant water use patterns in subsidence fracture zone due to coal mining using isotopic labeling. *Environmental Earth Sciences*, 81(11), 310.
- Chiles, J. P., & Delfiner, P. (2012). *Geostatistics: modeling spatial uncertainty* (Vol. 713). John Wiley & Sons.

- Clarke Topp, G., & Ferré, P. A. (2002). 3.1 Water Content. *Methods of soil analysis: part 4 physical methods*, 5, 417-545.
- Conway, G. R. (1987). The properties of agroecosystems. *Agricultural systems*, 24(2), 95-117.
- Costantini, E.A.C., C. Dazzi (eds.) 2013. The soils of Italy. World Soils Book Series, Springer, Dordrecht, The Netherlands, ISBN: 978-94-007-5641-0.
- Costanza, R., R. d'Arge, R. de Groot, S. Farber, M. Grasso, B. Hannon, K. Limburg, S. Naeem, R.V. O'Neill, J. Paruelo, et al., 1997. The value of the world's ecosystem services and natural capital. *Nature* 387, 253-260.
- Craig, H. (1961). Isotopic variations in meteoric waters. *Science*, 133(3465), 1702-1703.
- Cressie, N.A.C. 1993. *Statistics for spatial data*, revised edition. John Wiley & Sons, New York, USA, 920 pp., 900 pages, ISBN: 9780471002550.
- Crossman, N.D., B. Burkhard, S. Nedkov, L. Willemen, K. Petz, I. Palomo, E.G. Drakou, B. Martín-Lopez, T. McPhearson, K. Boyanova, 2013. A blueprint for mapping and modelling ecosystem services. *Ecosyst. Serv.* 4, 4-14.
- Cusano D, V. Allocca, S. Coda, D. Lepore, M. Vassallo, P. De Vita, 2022. The survey of Italian springs by the National Hydrographic Service, a forgotten database - Structuring and analysis of a dataset of Campania springs (southern Italy). *Italian J. Groundwater* 11, 31-41.
- Daily, G. C., Matson, P. A., & Vitousek, P. M. (1997). Ecosystem services supplied by soil. *Nature's services: societal dependence on natural ecosystems*, 113-132.
- Danesh-Yazdi, M., Klaus, J., Condon, L.E., and Maxwell, R.M., 2018. Bridging the gap between numerical solutions of travel time distributions and analytical storage selection functions. *Hydrological Processes*, 32, 1063 – 1076.
- De Deurwaerder, H., Visser, M. D., Detto, M., Boeckx, P., Meunier, F., Kuehnhammer, K., ... & Verbeeck, H. (2020). Causes and consequences of pronounced variation in the isotope composition of plant xylem water.
- de Melo, M. L. A., & van Lier, Q. D. J. (2021). Revisiting the Feddes reduction function for modeling root water uptake and crop transpiration. *Journal of Hydrology*, 603, 126952.

- De Vita, P. 2001. Acque superficiali, in L'ambiente geologico della Campania, a cura di A. Vallario, CUEN, Napoli, 207-221.
- De Vita, P., V. Allocca, F. Celico, S. Fabbrocino, C. Mattia, G. Monacelli, I. Musilli, V. Piscopo, A.R. Scalise, G. Summa, G. Tranfaglia, P. Celico, 2018. Hydrogeology of continental southern Italy. *J. Maps* 14, 230-241.
- Dey, P., & Mishra, A. (2017). Separating the impacts of climate change and human activities on streamflow: A review of methodologies and critical assumptions. *Journal of Hydrology*, 548, 278-290.
- Di Gennaro, A., Aronne, G., De Mascellis, R., Vingiani, S., Sarnataro, M., Abalsamo, P., Cona, F., Vitelli, L., Arpaia, G., 2002. I sistemi di terre della Campania (Land systems of Campania, scale 1:250.000). 64 pp., S.EL.CA., Florence, Italy (in Italian).
- Diacono, M., A. Castrignanò, C. Vitti, A.M. Stellacci, L. Marino, C. Coccozza, D. De Benedetto, A. Troccoli, P. Rubino, D. Ventrella, 2014. An approach for assessing the effects of site-specific fertilization on crop growth and yield of durum wheat in organic agriculture. *Precis. Agric.* 15, 479-498.
- Dominati, E., Patterson, M., & Mackay, A. (2010). A framework for classifying and quantifying the natural capital and ecosystem services of soils. *Ecological economics*, 69(9), 1858-1868.
- Dong XB., Yang W, Ulgiati S, Yan M, Zhang X. (2010) The impact of human activities on natural capital and ecosystem services of natural pastures in North Xinjiang China. *Ecol Model* 2010;225:28–39.
- Doran, J.W., T.B. Parkin, 1994. Defining and assessing soil quality. In: *Defining Soil Quality for a Sustainable Environment* (J.W. Doran, D.C. Coleman, D.F. Bezdicek, B.A. Stewart, eds.), SSSA Special Publications, vol. 35, pp. 3-21.
- Eching, S.O., Hopmans, J.W., and Wendroth, O. 1994. Unsaturated hydraulic conductivity from transient multistep outflow and soil water pressure data. *Soil Science Society of America Journal*, 58, 687-695.
- Ellis, E. C. (2011). Anthropogenic transformation of the terrestrial biosphere. *Philosophical Transactions of the Royal Society A: Mathematical, Physical and Engineering Sciences*, 369(1938), 1010-1035.

- Ellison, D., Morris, C. E., Locatelli, B., Sheil, D., Cohen, J., Murdiyarso, D., ... & Sullivan, C. A. (2017). Trees, forests and water: Cool insights for a hot world. *Global environmental change*, 43, 51-61.
- European Environment Agency. (2019). *The European environment—State and outlook 2020: Knowledge for transition to a sustainable Europe*. Luxembourg.
- FAO, 2020. Standard operating procedure for soil calcium carbonate equivalent: Volumetric calcimeter method. Food and Agriculture Organization of the United Nations, Rome, Italy.
- Fidélis T, Cardoso AS, Riazi F, Miranda AC, Abrantes J, Teles F, Roebeling PC (2021) Policy narratives of circular economy in the EU – assessing the embeddedness of water and land in national action plans. *J Clean Prod* 288:125685.
- Fischer, B., Frentress, J., Manzoni, S., Cousins, S. A., Hugelius, G., Greger, M., ... & Lyon, S. W. (2019). Mojito, anyone? An exploration of low-tech plant water extraction methods for isotopic analysis using locally-sourced materials. *Frontiers in Earth Science*, 7, 150.
- Gelfand, A. E., Zhu, L., & Carlin, B. P. (2001). On the change of support problem for spatio-temporal data. *Biostatistics*, 2(1), 31-45.
- Gelhar, L. W., Welty, C., & Rehfeldt, K. R. (1992). A critical review of data on field-scale dispersion in aquifers. *Water resources research*, 28(7), 1955-1974.
- Goovaerts, P. (1997). *Geostatistics for natural resources evaluation*. Applied Geostatistics.
- Goovaerts, P. 2008. Kriging and Semivariogram Deconvolution in the Presence of Irregular Geographical Units. *Math. Geology* 40(1), 101-128.
- Gotway Crawford, C.A., L.J. Young, 2005. Change of support: An interdisciplinary challenge. In: *Geostatistics for Environmental Applications* (P. Renard, H. Demougeot-Renard, R. Froidevaux, eds.), pp. 1-13, Springer-Verlag Berlin Heidelberg, ISBN-10: 3-540-26533-3.
- Granier, A., 1985. Une nouvelle methode pour la mesure du flux de seve brute dans le tronc des arbres. *Annales des Sciences Forestières*, 42 (2), 193–200, doi: 10.1051/forest:19850204

- Groh, J., Stumpp, C., Lücke, A., Pütz, T., Vanderborght, J., & Vereecken, H. (2018). Inverse estimation of soil hydraulic and transport parameters of layered soils from water stable isotope and lysimeter data. *Vadose Zone Journal*, 17(1), 1-19.
- Guarino, A., A. Lima, D. Cicchella, S. Albanese, 2022. Radon flux estimates, from both gamma radiation and geochemical data, to determine sources, migration pathways, and related health risk: The Campania region (Italy) case study. *Chemosphere* 287, 132233.
- Guswa, A. J., Tetzlaff, D., Selker, J. S., Carlyle-Moses, D. E., Boyer, E. W., Bruen, M., ... & Levia, D. F. (2020). Advancing ecohydrology in the 21st century: A convergence of opportunities. *Ecohydrology*, 13(4), e2208.
- Haines-Young R, Potschin M (2018) CICES V5. 1. Guidance on the application of the revised structure. Fabis Consulting, p. 53.
- Harding, B. E., & Deutsch, C. V. (2019). Change of Support and the Volume Variance Relation. *Geostatistics Lessons*.
- Heuvelink, G.B.M. 1998. Error propagation in environmental modelling with GIS. Taylor & Francis Ltd, London, 127 pp., ISBN 0-7484-0743.
- Heuvelink, G.B.M. 2014. Uncertainty quantification of *GlobalSoilMap* products. In: *GlobalSoilMap. Basis of the Global Spatial Soil Information System* (D. Arrouays, N.J. McKenzie, J.W. Hempel, A. Richer de Forges, A.B. McBratney, eds.), Proceedings of the First *GlobalSoilMap* Conference, Orleans, France, 7th –9th October 2013, Taylor & Francis, Balkema, The Netherlands.
- Hewitt, A., Dominati, E., Webb, T., & Cuthill, T. (2015). Soil natural capital quantification by the stock adequacy method. *Geoderma*, 241, 107-114.
- Hopmans, J. W., Šimůnek, J., Romano, N., & Durner, W. (2002). 3.6. 2. Inverse Methods. *Methods of soil analysis: Part 4 Physical methods*, 5, 963-1008.
- Hopmans, J.W., D.R. Nielsen, K.L. Bristow, 2002. How useful are small-scale soil hydraulic property measurements for large-scale vadose zone modeling. In: *Heat and Mass Transfer in the Natural Environment, The Philip Volume* (D. Smiles, P.A.C. Raats, A. Warrick, eds.), AGU, Geophysical Monograph Series No. 129, 247-258.

- Hrachowitz, M., P. Benettin, B.M. van Breukelen, O. Fovet, N.J.K. Howden, L. Ruiz, Y. van der Velde, A.J. Wade, 2016. Transit times - The link between hydrology and water quality at the catchment scale. *WIREs Water* 3, 629-657.
- Inamdar, S., Singh, S., Dutta, S., Levia, D., Mitchell, M., Scott, D., ... & McHale, P. (2011). Fluorescence characteristics and sources of dissolved organic matter for stream water during storm events in a forested mid-Atlantic watershed. *Journal of Geophysical Research: Biogeosciences*, 116(G3).
- IPBES, 2019, Global assessment report on biodiversity and ecosystem services, Intergovernmental Science-Policy Platform on Biodiversity and Ecosystem Services, Bonn, Germany (<https://www.ipbes.net/global-assessment-report/biodiversity-ecosystem-services>) accessed 6 August 2019
- IPCC, 2019: Climate change and land: an IPCC special report on climate change, desertification, land degradation, sustainable land management, food security, and greenhouse gas fluxes in terrestrial ecosystems, Geneva.
- IPCC, 2022: Climate Change 2022: Impacts, Adaptation, and Vulnerability. Contribution of Working Group II to the Sixth Assessment Report of the Intergovernmental Panel on Climate Change [H.-O. Pörtner, D.C. Roberts, M. Tignor, E.S. Poloczanska, K. Mintenbeck, A. Alegría, M. Craig, S. Langsdorf, S. Lösschke, V. Möller, A. Okem, B. Rama (eds.)]. Cambridge University Press. In Press.
- Jackisch, C., Knoblauch, S., Blume, T., Zehe, E., & Hassler, S. K. (2020). Estimates of tree root water uptake from soil moisture profile dynamics. *Biogeosciences*, 17(22), 5787-5808.
- Jax, K. (2010). *Ecosystem functioning*. Cambridge University Press.
- Jia, G., Shevliakova, E., Artaxo, P., De Noblet-Ducoudré, N., Houghton, R., House, J., ... & Verchot, L. (2019). Land–climate interactions. *Climate change and land: an IPCC special report on climate change, desertification, land degradation, sustainable land management, food security, and greenhouse gas fluxes in terrestrial ecosystems*. Preprint at <https://www.ipcc.ch/srcl/chapter>.
- Jones, C. W. (1985). *Effects of Brine on the Soil Lining of an Evaporation Pond*. ASTM International.

- Journel, A.G., C.J. Huijbregts, 1978. *Mining Geostatistics*. Academic Press, London, 600 p.
- Kahmen, A., Buser, T., Hoch, G., Grun, G., & Dietrich, L. (2021). Dynamic 2H irrigation pulse labelling reveals rapid infiltration and mixing of precipitation in the soil and species-specific water uptake depths of trees in a temperate forest. *Ecohydrology*, 14(6), e2322.
- Kaptijn, E. (2018). Learning from ancient water management: Archeology's role in modern-day climate change adaptations. *Wiley Interdisciplinary Reviews: Water*, 5(1), e1256.
- Kendall, C., & McDonnell, J. J. (Eds.). (2012). *Isotope tracers in catchment hydrology*. Elsevier.
- Kleine, L., Tetzlaff, D., Smith, A., Wang, H., & Soulsby, C. (2020). Using water stable isotopes to understand evaporation, moisture stress, and re-wetting in catchment forest and grassland soils of the summer drought of 2018. *Hydrology and Earth System Sciences*, 24(7), 3737–3752. <https://doi.org/10.5194/hess-24-3737-2020>
- Koeniger, P., Marshall, J.D., Link, T., Mulch, A., 2011. An inexpensive, fast, and reliable method for vacuum extraction of soil and plant water for stable isotope analyses by mass spectrometry. *Rapid Commun. MassSpectrom.* 25, 3041–3048. <https://doi:10.1002/rcm.5198>.
- Kuhlemann, L. M., Tetzlaff, D., Smith, A., Kleinschmit, B., & Soulsby, C. (2021). Using soil water isotopes to infer the influence of contrasting urban green space on ecohydrological partitioning. *Hydrology and Earth System Sciences*, 25(2), 927-943.
- Kühnhammer, K., Kübert, A., Brüggemann, N., Deseano Diaz, P., van Dusschoten, D., Javaux, M., Merz, S., Vereecken, H., Dubbert, M., & Rothfuss, Y. (2020). Investigating the root plasticity response of *Centaurea jacea* to soil water availability changes from isotopic analysis. *New Phytologist*, 226(1), 98–110. <https://doi.org/10.5194/hess-24-4413-2020>
- Kumar, P., M. Verma, M.D. Wood, D. Negandhi, 2010. *UNEP guidance manual for the valuation of regulating services*. ISBN: 978-92-807-3131-6.

- Lajaunie, C., H. Wackernagel, 2000. Geostatistical approaches to change of support problems – Theoretical Framework. IMPACT Technical Report N-30/01/G, ENSMP-ARMINES, Centre de Géostatistique, Fontainebleau, France.
- Lal, R. 2015. Restoring soil quality to mitigate soil degradation. *Sustainability* 7, 5875-5895.
- Landgraf, J., Tetzlaff, D., Wu, S., Freymüller, J., & Soulsby, C. (2022). Using stable water isotopes to understand ecohydrological partitioning under contrasting land uses in a drought-sensitive rural, lowland catchment. *Hydrological Processes*, 36(12), e14779.
- Landwehr, J. M., & Coplen, T. B. (2004). The oxygen and hydrogen isotope ratios in waters from the largest river systems of the United States. *Isotope Hydrology and Integrated Water Resources Management*, 402.
- Landwehr, J. M., and T. B. Coplen (2006), Line-conditioned excess: A new method for characterizing stable hydrogen and oxygen isotoperatios in hydrologic systems, in International Conference on Isotopes in Environmental Studies, pp. 132–135, IAEA, Vienna
- Lazo, P. X., Mosquera, G. M., McDonnell, J. J., & Crespo, P. (2019). The role of vegetation, soils, and precipitation on water storage and hydrological services in Andean Páramo catchments. *Journal of Hydrology*, 572, 805-819.
- Luo, Y., Lü, Y., Fu, B., Harris, P., Wu, L., & Comber, A. (2019). When multi-functional landscape meets Critical Zone science: advancing multi-disciplinary research for sustainable human well-being. *National Science Review*, 6(2), 349-358.
- Malone, B.P., A.B. McBratney, B. Minasny, 2013. Spatial Scaling for Digital Soil Mapping. *Soil Sci. Soc. Am. J.* 77, 890-902.
- Martín-Gómez, P., Serrano, L., & Ferrio, J. P. (2017). Short-term dynamics of evaporative enrichment of xylem water in woody stems: implications for ecohydrology. *Tree physiology*, 37(4), 511-522.
- Marx, C., Tetzlaff, D., Hinkelmann, R., & Soulsby, C. (2022). Seasonal variations in soil–plant interactions in contrasting urban green spaces: Insights from water stable isotopes. *Journal of Hydrology*, 612, 127998.

- Mattern, S., M. Vancloster. 2010. Estimating travel time of recharge water through a deep vadose zone using a transfer function model. *Environ. Fluid Mech.* 10, 121-135.
- McBratney, A., Field, D. J., & Koch, A. (2014). The dimensions of soil security. *Geoderma*, 213, 203-213.
- McBratney, A.B. 1998. Some considerations on methods for spatially aggregating and disaggregating soil information. *Nutr. Cycl. Agroecosys.* 50, 51-62.
- McCutcheon R., J. McNamara, M. Kohn, and S. Evans (2017). An evaluation of the ecohydrological separation hypothesis in a semiarid catchment. *Hydrological Processes*, DOI: 10.1002/hyp.11052
- McDonnell, J. J. (2003). Where does water go when it rains. Moving beyond the variable.
- MEA Millennium Ecosystem Assessment Island Press, Washington, DC (2005)
- Mennekes, D., Rinderer, M., Seeger, S., & Orlowski, N. (2021). Ecohydrological travel times derived from in situ stable water isotope measurements in trees during a semi-controlled pot experiment. *Hydrology and Earth System Sciences*, 25(8), 4513-4530.
- Millar, C., Pratt, D., Schneider, D. J., & McDonnell, J. J. (2018). A comparison of extraction systems for plant water stable isotope analysis. *Rapid Communications in Mass Spectrometry*, 32(13), 1031-1044.
- Moradkhani, H., Sorooshian, S., Gupta, H. V., & Houser, P. R. (2005). Dual state-parameter estimation of hydrological models using ensemble Kalman filter. *Advances in water resources*, 28(2), 135-147.
- Nasta, P., Allocca, C., Deidda, R., & Romano, N. (2020). Assessing the impact of seasonal-rainfall anomalies on catchment-scale water balance components. *Hydrology and Earth System Sciences*, 24(6), 3211-3227.
- Nasta, P., B. Szabó, N. Romano, 2021b. Evaluation of pedotransfer functions for predicting soil hydraulic properties: A voyage from regional to field scales across Europe. *J. Hydrology: Regional Studies* 37, 100903, 1-20.
- Nasta, P., Bonanomi, G., Šimůnek, J., & Romano, N. (2021). Assessing the nitrate vulnerability of shallow aquifers under Mediterranean climate conditions. *Agricultural Water Management*, 258, 107208

- Nasta, P., Palladino, M., Sica, B., Pizzolante, A., Trifuoggi, M., Toscanesi, M., ... & Romano, N. (2020). Evaluating pedotransfer functions for predicting soil bulk density using hierarchical mapping information in Campania, Italy. *Geoderma Regional*, 21, e00267.
- Nasta, P., Palladino, M., Ursino, N., Saracino, A., Sommella, A., & Romano, N. (2017). Assessing long-term impact of land-use change on hydrological ecosystem functions in a Mediterranean upland agro-forestry catchment. *Science of the Total Environment*, 605, 1070-1082.
- Oerter E.J. and G. Bowen (2017), In situ monitoring of H and O stable isotopes in soil water reveals ecohydrologic dynamics in managed soil systems. *Ecohydrology*. e1841. <https://doi.org/10.1002/eco.1841>
- Orlowski, N., Breuer, L., & McDonnell, J. (2016, December). Worldwide Interlaboratory Comparison of Cryogenic Water Extraction Systems for Soil Water Stable Isotope Analysis. In AGU Fall Meeting Abstracts (Vol. 2016, pp. H31E-1440).
- Orlowski, N., Frede, H. G., Brüggemann, N., & Breuer, L. (2013). Validation and application of a cryogenic vacuum extraction system for soil and plant water extraction for isotope analysis. *Journal of Sensors and Sensor Systems*, 2(2), 179-193.
- Orlowski, N., Frede, H. G., Brüggemann, N., & Breuer, L. (2013). Validation and application of a cryogenic vacuum extraction system for soil and plant water extraction for isotope analysis. *Journal of Sensors and Sensor Systems*, 2(2), 179-193.
- Orlowski, N., Pratt, D. L., & McDonnell, J. J. (2016). Intercomparison of soil pore water extraction methods for stable isotope analysis. *Hydrological Processes*, 30(19), 3434-3449.
- Orlowski, N., Winkler, A., McDonnell, J. J., & Breuer, L. (2018). A simple greenhouse experiment to explore the effect of cryogenic water extraction for tracing plant source water. *Ecohydrology*, 11(5), e1967.
- Oshun, J., W. E. Dietrich, T. E. Dawson, and I. Fung (2016), Dynamic, structured heterogeneity of water isotopes inside hillslopes, *Water Resources Research*, 52, 164–189. doi:10.1002/2015WR017485.

- Palladino, M., N. Romano, E. Pasolli, P. Nasta, 2022. Developing pedotransfer functions for predicting soil bulk density in Campania. *Geoderma* 412, 115726, 1-13.
- Parris, K. (2010). Sustainable management of water resources in agriculture. OECD Publishing, ISBN: 978-92-64-08357-8.
- Penna, D., Geris, J., Hopp, L., and Scandellari, F., 2020. Water sources for root water uptake: Using stable isotopes of hydrogen and oxygen as a research tool in agricultural and agroforestry systems. *Agriculture, Ecosystems & Environment*, 291, 106790. <https://doi.org/10.1016/j.agee.2019.106790>.
- Penna, D., Hopp, L., Scandellari, F., Allen, S. T., Benettin, P., Beyer, M., ... & Kirchner, J. W. (2018). Ideas and perspectives: Tracing terrestrial ecosystem water fluxes using hydrogen and oxygen stable isotopes—challenges and opportunities from an interdisciplinary perspective. *Biogeosciences*, 15(21), 6399-6415.
- Penna, D., Stenni, B., Šanda, M., Wrede, S., Bogaard, T. A., Gobbi, A., ... & Chárová, Z. (2010). On the reproducibility and repeatability of laser absorption spectroscopy measurements for $\delta^2\text{H}$ and $\delta^{18}\text{O}$ isotopic analysis. *Hydrology and Earth System Sciences*, 14(8), 1551-1566.
- Penna, D., Stenni, B., Šanda, M., Wrede, S., Bogaard, T. A., Michelini, M. A. R. Z. I. A., ... & Wassenaar, L. I. (2012). Evaluation of between-sample memory effects in the analysis of $\delta^2\text{H}$ and $\delta^{18}\text{O}$ of water samples measured by laser spectrometers. *Hydrology and Earth System Sciences*, 16(10), 3925-3933.
- Penna, D., Zanotelli, D., Scandellari, F., Aguzzoni, A., Engel, M., Tagliavini, M., & Comiti, F. (2021). Water uptake of apple trees in the Alps: Where does irrigation water go? *Ecohydrology*, 14(6), e2306.
- Poca, M., Coomans, O., Urcelay, C., Zeballos, S. R., Bodé, S., & Boeckx, P. (2019). Isotope fractionation during root water uptake by *Acacia caven* is enhanced by arbuscular mycorrhizas. *Plant and Soil*, 441, 485-497.
- Ponge, J. F. (2015). The soil as an ecosystem. *Biology and fertility of soils*, 51(6), 645-648.

- Popleau, C., C. Vos, A. Don. 2017. Soil organic carbon stocks are systematically overestimated by the misuse of the parameters bulk density and rock fragment content. *Soil* 3, 61-66.
- Právǎlie, R. (2018). Major perturbations in the Earth's forest ecosystems. Possible implications for global warming. *Earth-Science Reviews*, 185, 544-571.
- Quintero, M., Sachet, E., Wyckhuys, K. A., Cordingley, J. E., Kizito, F., Cruz García, G. S., ... & Chirinda, N. (2015). Ecosystem action: CIAT's ecosystem services strategic initiative. *CIAT Publication*.
- Rabbel, I., Bogena, H.R., Neuwirth, B., and Diekkrüger, B., 2018. Using Sap Flow Data to Parameterize the Feddes Water Stress Model for Norway Spruce. *Water*, 10, 279, doi:10.3390/w10030279
- Rabot, E., Guiresse, M., Pittatore, Y., Angelini, M., Keller, C., & Lagacherie, P. (2022). Development and spatialization of a soil potential multifunctionality index for agriculture (Agri-SPMI) at the regional scale. Case study in the Occitanie region (France). *Soil Security*, 6, 100034.
- Rallo, G., Agnese, C., Blanda, F., Minacapilli, M., & Provenzano, G. (2010). Agro-Hydrological models to schedule irrigation of Mediterranean tree crops. *Italian journal of agrometeorology*, 1, 11-21.
- Regione Campania, 2009. Agricultural land use map of Campania (CUAS, Carta dell'Utilizzazione Agricola del Suolo). PSR 2007-2013. Retrieved from <https://sit2.regione.campania.it/content/carta-utilizzazione-agricola-dei-suoli>.
- Remondi, F., M. Botter, P. Burlando, S. Fatichi, 2019. Variability of transit time distributions with climate and topography: A modelling approach. *J. Hydrol.* 569, 37-50.
- Rivoirard, J. 2001. Which models for collocated cokriging? *J. Math. Geol.* 33, 117-131
- Robinson, D. A., Emmett, B. A., Reynolds, B., Rowe, E. C., Spurgeon, D., Keith, A. M., ... & Harrison, R. (2012). Soil natural capital and ecosystem service delivery in a world of global soil change. *Soils and food security*, 35, 41.
- Romano N, Hopmans JW, Dane JH. 2002. Water retention and storage: Suction table. In "Methods of Soil Analysis, Part 4, Physical Methods" (J.H. Dane and G.C. Topp, eds.), pp. 692-698, SSSA Book Series N.5, Madison, WI, USA.

- Romano, N., 1993. Use of an inverse method and geostatistics to estimate soil hydraulic conductivity for spatial variability analysis. *Geoderma*, 60, 169-186.
- Romano, N., and Santini, A., 1999. Determining soil hydraulic functions from evaporation experiments by a parameter estimation approach: Experimental verifications and numerical studies. *Water Resources Research*, 35, 3343-3359.
- Romano, N., M. Palladino, 2002. Prediction of soil water retention using soil physical data and terrain attributes. *J. Hydrol.* 265, 56-75.
- Romano, N., Nasta, P., Bogena, H., De Vita, P., Stellato, L., & Vereecken, H. (2018). Monitoring hydrological processes for land and water resources management in a Mediterranean ecosystem: The Alento River Catchment Observatory. *Vadose zone journal*, 17(1), 1-12.
- Rozanski, K., Araguás-Araguás, L., & Gonfiantini, R. (1993). Isotopic patterns in modern global precipitation. *Climate change in continental isotopic records*, 78, 1-36.
- Russel, J.C., E.B. Engle, 1928. The organic matter content and color of soils in the central grassland states. In: *Proceedings and Papers of the First International Congress of Soil Science* (R.B. Deemer, ed.), June 13-22, 1927, Washington, DC, USA.
- S. Inamdar, in *The Use of Geochemical Mixing Models to Derive Runoff Sources and Hydrologic Flow Paths*, ed. by D. F. Levia (Springer, Dordrecht/Heidelberg/London/New York, 2011), pp. 163–181.
- Schaap, M.G., and Leij, F.J., 2000. Improved prediction of unsaturated hydraulic conductivity with the Mualem-van Genuchten model. *Soil Science Society of America Journal*, 64:843-851.
- Schelle, H., Iden, S.C., Fank, J. and Durner, W., 2012. Inverse estimation of soil hydraulic and root distribution parameters from lysimeter data. *Vadose Zone Journal*, 11(4), doi:10.2136/vzj2011.0169.
- Schirpke, U., Kohler, M., Leitinger, G., Fontana, V., Tasser, E., & Tappeiner, U. (2017). Future impacts of changing land-use and climate on ecosystem services of mountain grassland and their resilience. *Ecosystem Services*, 26, 79-94.
- Sciences, 24(8), 4045-4060.

- Šimůnek, J., Van Genuchten, M. T., & Šejna, M. (2016). Recent developments and applications of the HYDRUS computer software packages. *Vadose Zone Journal*, 15(7).
- Smith, A., Tetzlaff, D., Kleine, L., Maneta, M., & Soulsby, C. (2021). Quantifying the effects of land use and model scale on water partitioning and water ages using tracer-aided ecohydrological models. *Hydrology and Earth System Sciences*, 25(4), 2239-2259.
- Smith, D. F., Moore, M. T., Anderson, R. L., & Carey, A. E. (2021). Hydrological Separation of Event and Pre-event
- Song, X., S. Wang, G. Xiao, Z. Wang, X. Liu, and P. Wang (2009), A study of soil water movement combining soil water potential with stable isotopes at two sites of shallow groundwater areas in the North China Plain, *Hydrological Processes*, 23, 1376–1388. doi:10.1002/hyp.7267, 2009.
- Sprenger, M., Seeger, S., Blume, T., and Weiler, M., 2016. Travel times in the vadose zone: Variability in space and time. *Water Resources Research*, 52, 5727–5754, doi:10.1002/2015WR018077.
- Sprenger, M., Stumpp, C., Weiler, M., Aeschbach, W., Allen, S. T., Benettin, P., ... & Werner, C. (2019). The demographics of water: A review of water ages in the critical zone. *Reviews of Geophysics*, 57(3), 800-834.
- Sprenger, M., Tetzlaff, D., & Soulsby, C. ,2017. Soil water stable isotopes reveal evaporation dynamics at the soil–plant–atmosphere interface of the critical zone. *Hydrology and Earth System Sciences*, 21(7), 3839–3858. <https://doi.org/10.5194/hess-21-3839-2017>
- Sprenger, M., Volkmann, T.H.M., Blume, T., and Weiler, M., 2015. Estimating flow and transport parameters in the unsaturated zone with pore water stable isotopes. *Hydrology and Earth System Sciences*, 19, 2617–2635.
- SSSA, 2008. Glossary of soil science terms. Soil Science Society of America Inc., Madison, WI, USA, ISBN 978-0-89118-851-3.
- Staff, C. A. R. D. (2016). SWAT literature database for peer-reviewed journal articles. Center for Agricultural and Rural Development, Ames, IA. https://www.card.iastate.edu/swat_articles/(accessed 1 Aug. 2015).

- Stumpp, C., Stichler, W., Kandolf, M., & Šimůnek, J. (2012). Effects of land cover and fertilization method on water flow and solute transport in five lysimeters: A long-term study using stable water isotopes. *Vadose Zone Journal*, 11(1).
- Stumpp, C., Stichler, W., Kandolf, M., Šimůnek, J., 2012. Effects of land cover and fertilization method on water flow and solute transport in five lysimeters: A long-term study using stable water isotopes. *Vadose Zone Journal*, 11(1), doi:10.2136/vzj2011.0075.
- Szatmári, G., L. Pásztor, G.B.M. Heuvelink, 2021. Estimating soil organic carbon stock change at multiple scales using machine learning and multivariate geostatistics. *Geoderma* 403, 115356, 1-12.
- Tardio, G., Mickovski, S. B., Stokes, A., & Devkota, S. (2017). Bamboo structures as a resilient erosion control measure. *Proceedings of the Institution of Civil Engineers-Forensic Engineering*, 170(2), 72-83.
- Terribile F., A. Basile, R. De Mascellis, M. Iamarino, P. Magliulo, S. Pepe, 2007. Landslide processes and Andosols: The case study of the Campania region, Italy. In: *Soils of Volcanic Regions in Europe* (Ó. Arnalds, H. Óskarsson, F. Bartoli, P. Buurman, G. Stoops, E. García-Rodej, eds.) pp. 545-563, Springer-Verlag Berlin Heidelberg, ISBN: 978-3-540-48711-1.
- Tsuruta, K., Yamamoto, H., Katsuyama, M., Kosugi, Y., Okumura, M., and Matsuo, N. (2019). Effects of cryogenic vacuum distillation on the stable isotope ratios of soil water, *Hydrol. Res. Lett.*, 13,1–6, doi:10.3178/hr.13.1,2019.
- Tufano, R., V. Allocca, S. Coda, D. Cusano, F. Fusco, F. Nicodemo, A. Pizzolante, P. De Vita, 2020. Groundwater vulnerability of principal aquifers of the Campania region (southern Italy). *J. Maps* 16, 565-576.
- UN Environment, 2019, Global environment outlook — Geo-6: healthy planet, healthy people., Cambridge University Press, Cambridge, UK.
- Valentin, C., Munch, J. C., & Berthelin, J. (Eds.). (2018). *Soils as a Key Component of the Critical Zone 1: Functions and Services*. John Wiley & Sons.
- Van De Velde, J. H. and Bowen, G. J.: Effects of chemical pretreatments on the hydrogen isotope composition of 2 : 1 clay minerals, *Rapid Commun. Mass Sp.*, 27, 1143–1148 <https://doi.org/10.1002/rcm.6554>, 2013.

- Van Genuchten, M. T. (1980). A closed-form equation for predicting the hydraulic conductivity of unsaturated soils. *Soil science society of America journal*, 44(5), 892-898.
- Van Meerveld, H. J., Jones, J. P., Ghimire, C. P., Zwartendijk, B. W., Lahitiana, J., Ravelona, M., & Mulligan, M. (2021). Forest regeneration can positively contribute to local hydrological ecosystem services: Implications for forest landscape restoration. *Journal of Applied Ecology*, 58(4), 755-765.
- Vanderborght, J., and Vereecken, H., 2007. Review of dispersivities for transport modelling in soils. *Vadose Zone Journal*, 6:29–52. doi:10.2136/vzj2006.0096
- Vereecken, H., Schnepf, A., Hopmans, J. W., Javaux, M., Or, D., Roose, T., ... & Young, I. M. (2016). Modeling soil processes: Review, key challenges, and new perspectives. *Vadose zone journal*, 15(5).
- Vogel, H. J., Eberhardt, E., Franko, U., Lang, B., Ließ, M., Weller, U., ... & Wollschläger, U. (2019). Quantitative evaluation of soil functions: Potential and state. *Frontiers in Environmental Science*, 164.
- von Freyberg, J., Allen, S. T., Grossiord, C., & Dawson, T. E. (2020). Plant and root-zone water isotopes are difficult to measure, explain, and predict: Some practical recommendations for determining plant water sources. *Methods in Ecology and Evolution*, 11(11), 1352-1367.
- Wackernagel, H. 2003. *Multivariate geostatistics: An introduction with applications*, 3rd edition. Springer-Verlag, Berlin.
- Wadoux, A.M.J.-C., G.B.M. Heuvelink, R.M. Lark, P. Lagacherie, J. Bouma, V.L. Mulder, Z. Libohova, L. Yang, A.B. McBratney, 2021. Ten challenges for the future of pedometrics. *Geoderma* 401, 115155, 1-11.
- WCED, S. W. S. (1987). World commission on environment and development. *Our common future*, 17(1), 1-91.
- Weynants, M., H. Vereecken, M. Javaux, 2009. Revisiting Vereecken pedotransfer functions: Introducing a closed-form hydraulic model. *Vadose Zone J.* 8, 86-95.
- Willaarts, B. A., Volk, M., & Aguilera, P. A. (2012). Assessing the ecosystem services supplied by freshwater flows in Mediterranean agroecosystems. *Agricultural Water Management*, 105, 21-31.

- Wilusz, D. C., Harman, C. J., Ball, W. P., Maxwell, R. M., & Buda, A. R. (2020). Using particle tracking to understand flow paths, age distributions, and the paradoxical origins of the inverse storage effect in an experimental catchment. *Water Resources Research*, 56(4), e2019WR025140.
- Wunder, S., & Thorsen, B. J. (2014). Quantifying water externalities from forests. *The Provision of Forest Ecosystem Services*, 1, 21-25.
- Yin, L., et al., 2015. Interaction between groundwater and trees in an arid site: Potential impacts of climate variation and groundwater abstraction on trees. *Journal of Hydrology*, 528: 435–448.
- Zampieri, M. 2021. Reconciling the ecological and engineering definitions of resilience. *Ecosphere* 12, 3375, 1-8.
- Zarlenga, A., and Fiori, A., 2020. Physically based modelling of water age at the hillslope scale: The boussinesq age equations. *Hydrological Processes*, 34(12), 2694–2706. <https://doi.org/10.1002/hyp.13755>.
- Zarlenga, A., Fiori, A., and Cvetkovic, V., 2022. On the interplay between hillslope and drainage network flow dynamics in the catchment travel time distribution. *Hydrological Processes*, 36(3), e14530. <https://doi.org/10.1002/hyp.14530>
- Zedda, L., & Rambold, G. (2015). The diversity of lichenised fungi: Ecosystem functions and ecosystem services. *Recent advances in Lichenology*, 121-145.
- Zhao, P., X. Tang, P. Zhao, C. Wang, and J. Tang (2013), Identifying the water source for subsurface flow with deuterium and oxygen-18 isotopes of soil water collected from tension lysimeters and cores. *Journal of Hydrology*, 503, 1–10. [10.1016/j.jhydrol.2013.08.033](https://doi.org/10.1016/j.jhydrol.2013.08.033)
- Zhao, Y., Dai, J., Tang, Y., & Wang, L. (2022). Illuminating isotopic offset between bulk soil water and xylem water under different soil water conditions. *Agricultural and Forest Meteorology*, 325, 109150.
- Zhou, T., Šimůnek, J., Braud, I., Nasta, P., Brunetti, G., & Liu, Y. (2022). The impact of evaporation fractionation on the inverse estimation of soil hydraulic and isotope transport parameters. *Journal of Hydrology*, 612, 128100.
- Zwetsloot, M. J., van Leeuwen, J., Hemerik, L., Martens, H., Simo Josa, I., Van de Broek, M., ... & Creamer, R. E. (2021). Soil multifunctionality: Synergies and

trade-offs across European climatic zones and land uses. *European Journal of Soil Science*, 72(4), 1640-1654.